OPISA
Optoelectronics Packaging Interfaces for Sub-Micron Alignment

Asif T. Malik

School of Computing and Mathematical Sciences
University of Greenwich
London, UK

A thesis submitted in partial fulfilment of the requirements of the University of Greenwich for the Degree of Doctor of Philosophy

November 2014

DECLARATION

I certify that this work has not been accepted in substance for any degree, and is not concurrently being submitted for any degree other than that of Doctor of Philosophy (PhD) being studied at the University of Greenwich. I also declare that this work is the result of my own investigations except where otherwise identified by references and that I have not plagiarised the work of others.

Student: Asif Malik

_____

First Supervisor: Professor Chris Bailey

_____

Second Supervisor: Dr Stoyan Stoyanov

_____

_____

Dedications

For my dad

Ghulum-Mustafa Malik

For my mum

Amna Nasreen Malik

Who made all this possible

Acknowledgments

First and fore most I would like to thank Professor Chris Bailey for accepting me on this project. I greatly and sincerely appreciate his guidance and help throughout this project as my first supervisor. As I am also indebted for his valuable comments and suggestions throughout this work.

I would also like to thank Dr Michael Hughes who was my second supervisor but due to family commitments had to leave the University of Greenwich. Kindly, Dr Stoyan Stoyanov became my second supervisor for the remainder of the project and who has given me support for this work. I would like to thank Dr Georgi Djambazov who provided technical help regarding PHYSICA. I also appreciate the input from David Gwyer, Yek Bing, Dr Steve Ridout and other fellow colleagues.

I would like to acknowledge the financial support from the Engineering and Physical Sciences Research Council (EPSRC) through PRIME Faraday as an Industrial Case Award, and also to Oclaro for their financial support of this project. I would like to thank the engineering team at Oclaro who provided information and guidance for the project, this includes Drs Jon Hall and Colin Edge, Jim Fraser, Paul Firth and others who would at various times joined our meetings.

Last but not least to my wife Sobia, who has been a constant source of inspiration, praise, patience and encouragement with my work. To Usman and Mustafa whose time I took for writing this thesis. For Maryam (15th May 2014) and Aiysha (4th June 2015) who timed their arrival when all this was finished.

For just being there, Tayyaba, Zahida and Wasiq, Arif and Asgree, Atif and Yasmine, Abid and Nazia, Shahida; and their little “lambs”, their “grown sheep”, and the cats and budgies!

Abstract

For optoelectronic devices submicron precision is required to optimally couple the laser source with the optical fibre. Laser welding is used because of its inherent attributes of accuracy, strength, cleanliness and minimised heat affected zone and structural changes. Due to the rapid solidification of the welded parts post welding residual stresses occur which can lead to a post weld shift between the aligned components and can significantly reduce the light coupling efficiency. Submicron misalignment induced due to the welding process can result in significant power loss. This is a serious and common issue in the manufacture of optoelectronic components and affects production rates.

The aim of this work is the development of a methodology that can estimate the residual stresses in the weld piece and to optimise the process by locating the optimal site for micro laser welding. The aim establishes the research question which was addressed by nine objectives. The first eight objectives are elements that comprise the Optoelectronic Packaging Interfaces for Sub-Micron Alignment (OPISA) project. The final objective is the dissemination of this work.

Finite element models were developed and used with design of experiments (DoE) statistical technique. This was used to investigate how the key process parameters influence the resultant stress in the optical fibre and to develop a predictive surrogate model. The surrogate model was used with Monte Carlo simulations to determine the fibre stress variation when uncertainty and variation of the design variables are accounted for. The Monte Carlo simulations predicted fibre stress response values which were used to understand how the uncertainties of the input design variables propagate into uncertainty and variation of fibre stress. The surrogate model was used in a sensitivity and risk analysis. The capability analysis of the welding process was also investigated.

The original finding of this work is the development of a methodology that fulfils the aim. The work successfully demonstrated that the current industry weld spot locations

generate 180MPa of post weld stress in the optical fibre. Using the OPISA methodology the optimal weld locations generate 57.6MPa of post weld stress in the optical fibre.

Contents

Figures

Tables

Nomenclature

	Finite Element Analysis
A	Cross section of weld
β	Point source
dA	Area on the plane section
dM	Resultant moment
Δt	Time interval
Δz	Width of element
β	Point source
FE	Finite element
lx	x Direction cosine to the boundary surface
ly	y Direction cosine to the boundary surface
lz	z Direction cosine to the boundary surface
lx	Cosine of the x direction
ly	Cosine of the y direction
lz	Cosine of the z direction
L_f	Liquid fraction
P_t	Plate thickness
φ	Temperature distributions
x	Coordinate
y	Coordinate
z	Coordinate
σ	Stress
σ_{vm}	von Mises stress
T_E	Temperature in the "east" element
T_W	Temperature in the "west" element
	Laser
CGR	Course grained region

FGR	Fine grained region
HAZ	Heat affected zone
Nd:YAG	Neodymium-doped yttrium aluminium garnet
CWNd:YAG	Continuous-Wave Operation Neodymium-doped yttrium aluminium garnet.
PTR	Partially transformed region
Q	Rate of heat
q_t	The fraction of laser energy transmitted through the top surface
Q'	Rate of heat per unit length
q	Thermal energy generation
R	Distance to the heat source
r	Radial distance
r_b	Beam radius
r_p	Heat distribution parameter
ρ_s	Fraction of laser energy reflected from the top surface of the bottom material
r_p	Heat distribution parameter
Ti 6Al	Titanium alloy Grade 5

Statistical

A^2	Anderson-Darling test statistic
Adj SS	Adjusted sum of squares
Adj MS	Adjusted mean squares
c_i	Polynomial coefficients
c_{ij}	Polynomial coefficients
Coef	Coefficient
DoE	Design of Experiment
e_i	Residual
G	Cumulative probability of a point
i	Order of the value
l_i	Factor level
LSL	Lower specification limit

R^2	Coefficient of multiple determination
R-Sq	Coefficient of multiple determination
R-Sq(pred)	Predicted R^2
R-Sq(adj)	Adjusted R^2
Seq SS	Sequential sum of squares
SE Coef	Standard error of the coefficient
USL	Upper specification limit
$\hat{y}$	The fitted response
y_i	Observed value
$\hat{y}_i$	Predicted value

Thermodynamics

ε	Material emissivity
f	Heat distribution factor
T_∞	Room temperature
T_∞	Room temperature
I_o	Intensity of the incident radiation
T_0	Initial temperature
μ	Absorption coefficient
C	Heat capacity
CO2	Carbon dioxide
C_p	Specific heat
D	Thermal diffusion
e_r	Electrical resistivity
h	Surface heat loss coefficient
h_c	Heat transfer coefficient
H_{in}	Heat input on the surface (Wm^{-2})
j	Numbers of design points (runs)
K	thermal conductivity $Wm^{-1}K^{-1}$
k	Empirical factor
m_d	Material diffusivity
N	Number of residuals

P	Laser power
p	Number of predictors
s	Stefan-Boltzmann constant
t	Time
T	Temperature
T_L	Liquidus temperature
T_S	Solidus temperature
v	Velocity
α	Thermal diffusivity
α	Significance level
η	Absorption coefficient
η	Laser absorptivity
λ	Wavelength
ρ	Density
$I(z)$	Intensity of the radiation at a depth z
ω	Lagrange multiplier

Chapter 1

Introduction

This introductory chapter lays the background to the work. The funding of the project and the interest of Oclaro in this project are discussed. This gives the motivation of the project. The aim and objectives needed to fulfil the project are identified. The chapter ends with a discussion on the layout of the thesis and the contribution of the work that is presented here.

1.1 Project Partners

The Engineering and Physical Sciences Research Council (EPSRC) through the PRIME Faraday Partnership financially supported the Optoelectronic Packaging Interfaces for Sub-Micron Alignment (OPISA) project as a PhD Industrial Case Award. Bookham Technology plc is the industrial partner and was the first company to develop optical devices that could be integrated into a silicon chip. Bookham Technology and Avanex merged in 2009 to become the largest producer of optoelectronic devices and subsystems for fibre optic networks. The merged company is now known as Oclaro.

Oclaro uses micro laser welding in optoelectronic packaging. After the welding, residual stresses occur and the post weld shift reduces the efficiency of the package. The company is interested in conserving production resources and increasing production rates of optoelectronic packages by its manufacturing division. To fulfil this Oclaro's interest as a project partner is to use the development of the OPISA methodology to reduce post weld shift.

The OPISA methodology will identify regions of the fibre capsule that will generate the least post welding stress for the laser settings used at Oclaro. This will be achieved by developing a surrogate model and optimising using a response surface methodology.

1.2 Motivation

Optoelectronic packages provide a platform for integrating photonic, optoelectronic and electronic devices for the transmission of optical signals in telecommunication and computing networks. The main issue is that of manufacturing, as the cost of packaging can exceed that of the components themselves (GIA 2010).

To meet the increase in volume of optoelectronic components, one of the main aims of optoelectronic packaging is cost reduction and high volume manufacturing. A prime reason for this is the increased demand in optical components due to the migration from the long haul networks to metro networks and applications that need to access these networks. Uses of optoelectronic packages can be found in any optical networking components that are dependent upon optical carrier signals. Additional pressure for demand has come from wavelength-division multiplexing (WDM) technology (Stearns and Trask, 2004). Manufacturers have missed opportunities as orders are not met since devices cannot be assembled fast enough (OITDA 2012).

Manufacturing of optoelectronic packages is usually undertaken manually or semi-manually and consists of an assembly line with researchers sitting at workstations. Within the manufacturing process the alignment of the laser source with the optical fibre is the most critical and time consuming aspect.

Depending on the application of the optoelectronic package the requirements can vary. However, for all applications it is the alignment of the optical fibre with the laser source that is of importance. For efficient optical link performances alignment is critical, as alignment within a few microns for multi-mode optoelectronic devices and within a micron to sub-micron for single-mode devices are required (Vernooy 2004). Post welding misalignments occur, also known as post weld shift (PWS). These can be transverse, longitudinal or angular, and cause optical power losses due movement of the optical fibre. Of these misalignments lateral alignments tend to produce greater loss of efficiency as compared to longitudinal alignments (Ishikawa 2002).

The reduction of the post welding shift in optoelectronic components is the motivation of the project and has given rise to the research question – to create a methodology that

will identify weld locations that cause the least post welding stress in the optoelectronic package.

1.2.1 Alignment Techniques

The methods used for alignment during manufacture consist of three approaches:

- The active alignment approach is used when the laser's active region or the mode is not known (Ishikawa 2002). Using raster-scanning with respect to the optical source at the input end, the fibre is actively monitored at the output end with the laser on. Once the input end is aligned to give a maximum output the fibre is then welded into place using laser welding. This technique produces submicron alignment accuracy and can take minutes to perform.
- Passive alignment takes seconds to perform and achieves micron level alignment. For this technique the active region of the laser needs to be known. The active region is aligned using a vision-assisted machine. The alignment of the active region occurs at a marker on a silicon sub-mount to which the laser is soldered. The fibre is aligned with the marker by placing it in a v-groove.
- Self-alignment can achieve an accuracy of about two micrometres. If soldering is used, the process takes seconds to achieve and can be done by a batch process (Tan 2005). Otherwise, self-alignment involves using ball lenses between ridges with matching indentations or alignment holes, for waveguides or fibres. A lens placed in a v-groove on a silicon submount and is at the outlet facet of a semiconductor laser. The silicon submount is seated on a thermo-electric cooler and is integrated into the transmitter optical sub-assembly.

1.2.2 Technologies for Optoelectronic Packaging

A number of technologies are used in optoelectronic packaging for optical interconnects at the component and module levels. These include using wire bonding, laser welding, soldering, die attachment, epoxy and hermetic / non-hermetic sealing. The technology that is relevant for this project, specifically Nd:YAG (neodymium-doped yttrium aluminium garnet) laser welding, which is used to secure the alignment of the optical fibre with the laser interface, and will be briefly discussed here and reviewed in detail in a later chapter.

Submicron alignment accuracy between the optical source and the laser source is achieved using active alignment. Nd:YAG laser welding is used to secure the fibre capsule to the butterfly package. For some, non-Oclaro butterfly packages the alignment occurs inside the package using a Kovar cladded fibre, the Kovar protects the fibre, figure 1.1. A Kovar weld clip and the Kovar cladded fibre are welded together. As an alternatively to fixing the components in place, solder or epoxy can be used (Liu 2000).

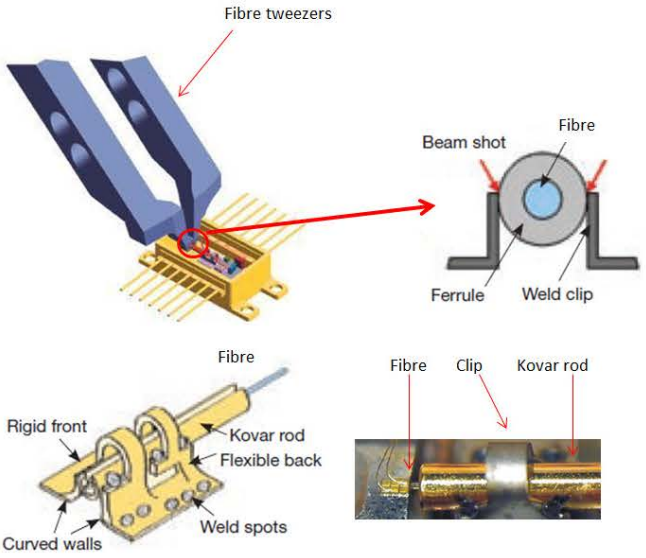

Figure 1.1. Laser welding of the weld clip to the fibre ferrule. (Adapted from Newport n.d, Miyachi Unitek n.d and Assembly Magazine n.d)

The technique described above is not used by Oclaro. For the Oclaro butterfly package, the fibre is aligned with the laser source using active alignment. The optical fibre is held in place inside a steel ferrule using epoxy. Once the fibre has been aligned, the steel ferrule and steel sleeve are welded together using a Nd:YAG laser source. Figure 1.2 shows the Oclaro package which contains a laser chip that has been designed for use in wavelength division multiplexed 2.5 Gbs^{-1} long distance optical fibre trunk systems. The butterfly package is hermetically sealed and the complete package is priced at US $300 as of December 2013. The package is designed to give a stable unattended performance for a rated 25 year lifetime.

For military applications, optoelectronic devices used for telecommunications are required to function for a long life of operation in potentially humid, corrosive and

mechanically turbulent environments. Because of this, long term reliability is a requirement. Hence, optoelectronic devices require secure fixing of the aligned components and hermetic sealing of the housings (Fadhali et al., 2007). Specifically for these reason Oclaro use micro laser welding (Edge 2006).

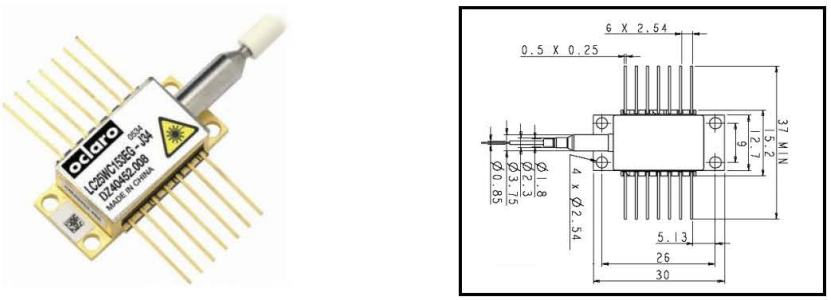

The package contains a laser chip which has been designed for use in Wavelength Division Multiplexed. The dimensions are in millimetres.

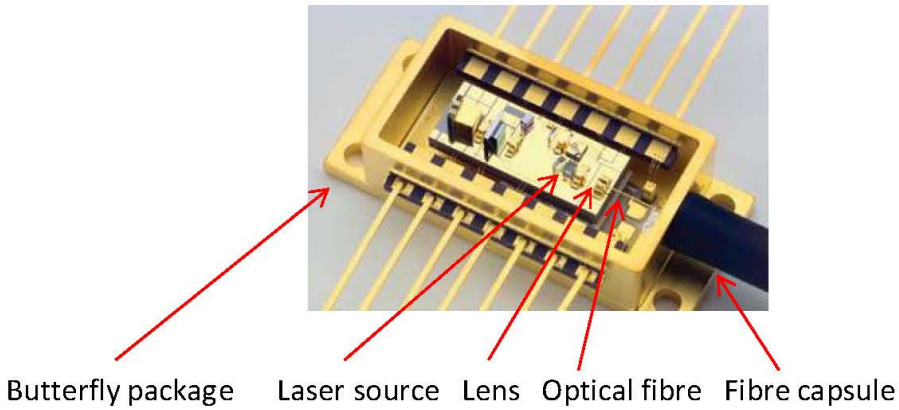

Figure 1.2. The Oclaro fibre capsule and the butterfly package. (Oclaro n.d).

As just discussed above, one of the main issues within manufacturing of optoelectronic devices is the alignment of the optical fibre with the laser source. It has been estimated that 60% to 80% of the cost of optoelectronic modules are due to the coupling and packaging processes (Nawi et al., 2012). For the Oclaro package once the alignment of the optical fibre and laser source has occurred a steel sleeve is welded to the steel ferrule of the fibre capsule. The welding process uses micro laser welding which causes thermal stresses. Micrometre misalignment between the optical fibre and the laser source can occur as the weld spot cools and residual stresses evolve. It is this that has given the motivation for this project to develop a methodology that can predict an

optimal welding location where minimal residual stresses occur and so minimise fibre misalignment.

1.3 Aim and Objectives of the OPISA Project

The aim of the OPISA project (Malik et al., 2007) was to develop a generic methodology that can be used to minimise the misalignment between the optical fibre and the laser source during the micro laser welding process of the steel ferrule and sleeve. This aim was realised by nine objectives associated with this work, listed below:

1. Review of the physical processes that occur during and after laser welding – Chapter Two.
2. A review of the analytical and numerical models of laser welding – Chapter Two.
3. Surrogate modelling technologies used to develop the OPISA methodology – Chapter Three.
4. The development of a thermomechanical model that captures the welding of the sleeve and ferrule – Chapter Four.
5. Understanding the evolutions of the temperature fields, the von Mises stress and displacements of the optical fibre – Chapter Four.
6. The development of a simplified axisymmetric high fidelity model that will be used with design of experiments – Chapter Five.
7. Developing a surrogate model – Chapter Six.
8. Analysis of the uncertainties of the process – Chapter Seven:
9. Dissemination of this work to our industrial partner.

1.3.1 Objectives 1 and 2 - Reviews

The first two objectives consist of reviews and are covered in chapter two. The chapter starts with a discussion of how a laser weld forms and the physics of the process, this is the first objective. The second objective discusses three reviews. The first review looks at the early analytical models used for laser welding and the current understanding. The second review is a discussion of numerical modelling techniques. The third review is of the post weld shift. Objectives one and two form the basis of chapter two. The discussion from this chapter gives the background for chapters four and five.

1.3.2 Objective 3 - Other Modelling Technologies

Chapter three covers the third objective of reviewing the surrogate modelling technologies used in the OPISA project. Specifically the technologies that were selected would allow the development of a surrogate model. These technologies formed the content of chapters six and seven. This chapter also has a review of the use of design of experiments and response surface methodology in welding research.

1.3.3 Objectives 4 and 5 - The Thermomechanical Analysis

Chapter four fulfils the fourth and fifth objectives. The development of a thermomechanical model and an understanding of the evolutions of the temperature fields, the von Mises stress and the displacements of the optical fibre comprise chapter four. The thermomechanical model is developed using finite element analysis. This model was a one third symmetric model and it captured the geometry of the Oclaro fibre capsule.

1.3.4 Objective 6 - Simplified Axisymmetric Model

The sixth objective is covered in chapter five. The model from chapter four is simplified and developed as axisymmetric. The simplification was at the level of the geometry. This model was used for the design of experiments in order to create the surrogate model in chapter six.

1.3.5 Objective 7 - Developing a Surrogate Model

The high fidelity model developed in chapter five is used with the design of experiments to create a surrogate model. This is objective seven and is to be found in chapter six.

To determine the key process variables, design of experiments (DoE) using finite element analysis (FEA) is used to determine the magnitude of the post welding stresses in the optical fibre. Five process variables that are thought to contribute to the generation of post weld stresses in the optical fibre have been identified and were investigated. The process variables are:

- The inter-weld distance between the two micro weld spots
- The air gap between the sleeve and ferrule

- The angle at which the laser fires
- The diameter of the weld spot
- The penetration of the weld spot.

Design of experiments combined with finite element analysis is used to evaluate the post welding stresses in the fibre optic for different combinations of values for the above design variables. Using a least squares method a surrogate model is constructed in the form of an explicit polynomial approximation. This model is a function of the five process variables and can be used to perform a sensitivity analysis and evaluate the impact and significance of the process variables on the fibre stress, which is implemented in chapter seven.

1.3.6 Objective 8 - Uncertainty analysis

Objective eight, which forms chapter seven, is about uncertainty analysis and includes the investigation of risk analysis, process capability and process improvement. The surrogate model which is a linear with interactions polynomial function is used to perform risk analysis, process capability and process improvement. The influence of the manufacturing tolerances on the process variables are assessed using a Monte Carlo simulation. An initial design is assessed for this process to identify the important process parameters and to evaluate the capability of the welding process. Finally, the steepest descent algorithm within response surface methodology is improved using a novel application of the Monte Carlo method.

1.3.7 Objective 9 – Dissemination of the Work

This work is part of an industrial case award PhD. The work that resulted from this project was disseminated to the industrial partner.

1.4 Contribution

This work has resulted in the publication of two papers published in peer reviewed conference journals.

1. Malik Asif, Hughes Michael and Bailey Christopher (2006) Optoelectronic packaging interfaces for submicron alignment (OPISA) and the dynamics of laser spot weld formation. In: Proceedings of the 1st Electronics System Integration Technology Conference, 2006. IEEE, pp. 387-391. ISBN 1-4244-0552-1

2. Malik Asif, Stoyanov Stoyan, Bailey Christopher and Firth Paul (2009) Design for Reliability Methodology for Micro Laser Welding of Pigtail Fibres. In: 10th. Int. Conf. on Thermal, Mechanical and Multiphysics Simulation and Experiments in Micro-Electronics and Micro-Systems, EuroSimE, 2009. IEEE, pp. 232-238. ISBN 978-1-4244-4159-4

Chapter 2

Laser Welding Review

This chapter covers the first and second objective. The chapter starts with a discussion of the physical process of laser welding, which is the first objective. There are a number of physical processes to consider, see figure 2.1, which can make modelling a challenge. The physical processes are dependent upon the properties of the laser and the material upon which the electromagnetic radiation impinges. The laser properties include the power, radiation time, and angle of incidence, just to name a few. The material parameters include absorption of the radiation, thermal conductivity, specific heat capacity and density, to name just a few. Both the laser properties and the material parameters are important in the heating of the material by the electromagnetic radiation of the laser. This causes various effects in the material such as heating, melting and vaporisation, see figure 2.1. These contribute to the process of laser welding.

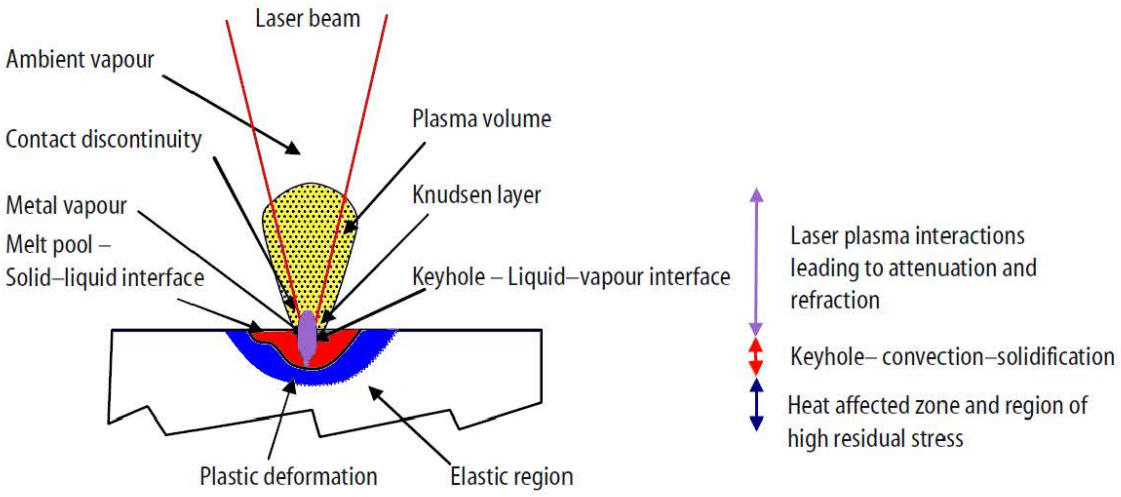

Figure 2.1. Physical interactions that occur during laser welding.

The chapter develops a discussion on residual stresses which can cause local yielding and plastic deformation on both a microscopic and macroscopic level. Knowledge of the internal stress state needs to be cognised to gain an understanding of how such stresses affect component performance. Both the magnitude and the distribution of the residual stress can be can be studied using modelling techniques.

Since the early development of numerical methods one of the important topics of research has been the application of computational techniques for the simulation of the welding process. The interest of this work is in residual stresses, and hence a review covered in this chapter will focus on the state of art of modelling welding residual stresses. The chapter continues with a review of analytical and numerical modelling of laser welding which is the second objective.

The chapter starts with an understanding of the laser welding process and the physical processes involved, the chapter ends with a review of the post weld shift. The post weld shift in essence gives the background to the research question of this work.

2.1 Laser Material Interactions

A process known as Fresnel absorption causes the laser energy to be absorbed a few nanometres into the surface of a metal. The Beer-Lambert law (Steen 1991) governs the absorption of laser radiation in a material, and is given by equation 2.1:

$$I(z) = I_o e^{-\mu z} \qquad \textbf{2.1}$$

Where the intensity of the radiation at a depth z is given by $I(z)$ and the I_o is the intensity of the incident radiation. The absorption coefficient is μ and depends on the metal.

Photons of the laser beam interact with the electrons of the material, whether they are free or bound. The inverse Bremsstrahlung effect describes the process of photons being absorbed by electrons. The Bremsstrahlung effect is the emission of photons from excited electrons. Radiation, reflected and transmitted, will be either re-radiated in all directions or can be kept by the lattice phonons (the bonding energy within a solid or

liquid structure), due to the vibrations of the electron. In the latter case the energy would be said to be absorbed as it no longer radiates. The structure will vibrate because of the phonons and the vibrations are transmitted throughout the structure by diffusion due to the linking of the molecules. The vibrations are detected as heat and can be described by Fourier's laws of heat conduction. If the vibrations are intense enough due to sufficient energy being absorbed the molecular bonding can break and the material shows melting. As the heating progresses the bonding loosens further due to the stronger molecular vibrations and the material vaporises.

2.2 Laser Heating of Metals

Figure 2.2 shows the different effects of heating of metals that can occur due to a laser. At a low power of about 1000 Wcm^{-2}, surface heating occurs, see figure 2.2(a). There are no changes in the material as heat is conducted away from the surface into the body of the material. The laser power determines if laser welding can occur. If the power is high enough laser welding can occur in either conduction mode or keyhole mode.

In conduction mode the laser process does not to break the surface of the weld pool. In this mode the laser energy passes into the depth of the material by conduction, figure 2.2(b). Marangoni-type forces resulting from the variation in surface tension with temperature cause strong stirring forces in the weld pool. This mode of welding where the laser beam is absorbed at the work piece surface forms a shallow and wide weld.

With keyhole mode, figure 2.2(c), also referred to as deep penetration welding, this corresponds to a process that creates a "keyhole" in the weld pool. Typically these welds have a deep narrow profile and they produce little distortion due to the small heat affected zone (Schubert et al., 1998). The laser power has to be sufficiently high for this to occur, and it also depends on the wavelength of the laser.

Additional parameters that affect the welding include the absorption coefficient, heat conduction of the material and the surface of the work piece. The level of power needed for the keyhole mode causes some of the surface material to vaporise (Duley, 1999).

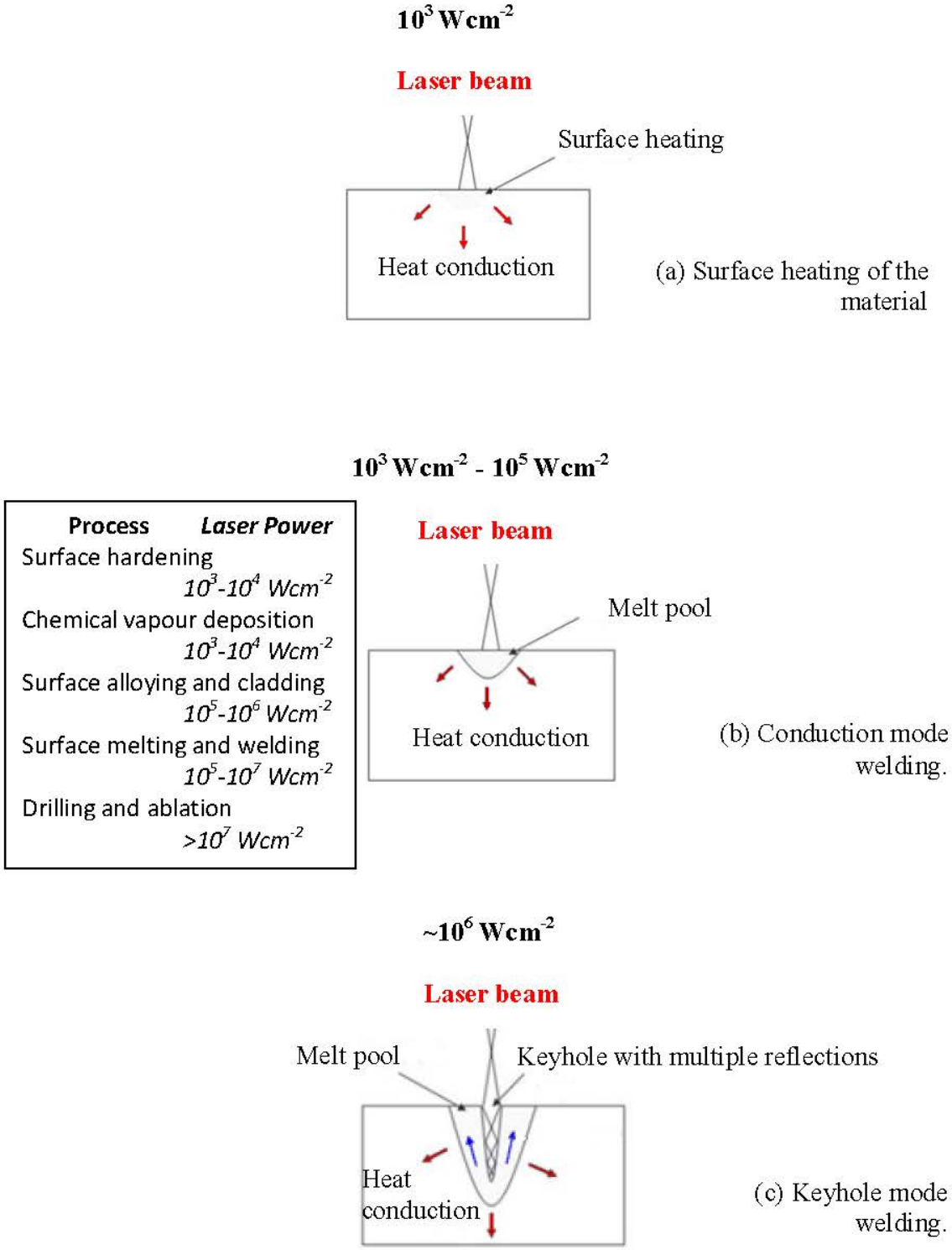

Figure 2.2. Different modes of laser welding. (Adapted from Kar and Langlais, 1995).

In the weld pool a small depression is formed due to the evaporation induced recoil pressure, this later develops into a keyhole by the upward movement of the molten material, figure 2.2c.

Inside the keyhole the laser under goes multiple reflections and is efficiently absorbed by the walls of the keyhole. The keyhole plays an important role in the transferring and distributing of the laser energy into the material. The vaporised material acts against the surface tension to keep the keyhole open. With keyhole mode welding narrow, deep penetration welds are possible. The peak power of a pulsed laser determines the depth of the weld in keyhole mode.

2.3 Conduction and Keyhole Welding

With conduction mode welding steady state conditions are reached in approximately 2.5 ms as heat is absorbed through the top surface (Bransch et al., 1994). The material conducts heat away at a steady rate as heat is input through the surface. The convection in the weld pool and the surface temperature determines the depth of the weld pool (Bransch et al., 1994). As the temperature decreases with the surface tension, molten metal starts to flow outward.

To form a keyhole, vaporisation of the material occurs with the use of a high energy laser. At the surface of the material the energy is absorbed by Fresnel absorption (absorption during reflection from a surface). The keyhole allows the energy of the laser to be absorbed as multiple reflections of the laser occur within the keyhole.

Chiang and Albright (1993) found that only a fraction of the energy from the laser is absorbed, which is sufficient to cause the material to melt. The rest of the energy is conducted into the material, or is lost by radiation or convection in the melt pool. The depth of the weld is determined by the amount of heat lost due to these factors. This will produce a deep and narrow melt pool as the laser penetrates the material due to the keyhole.

The keyhole is stabilised and is kept open for further penetration due to the vapour pressure in the keyhole, whilst the surface tension tends to close it at the surface. Owing to the continuous evaporation of the material by the laser, the keyhole is filled with vapour of the material. The temperature will determine the degree of energy absorption, as well as the degree of ionisation. At a low temperature the absorption coefficient is proportional to the degree of ionisation. The degree of ionisation increases with the temperature, and completes as the temperature increases. The temperature increases, the absorption coefficient decreases due to the lower electron and ion densities. This absorption occurs due to inverse Bremsstrahlung, leading to plasma re-radiation. Hence, higher laser intensities give deeper penetration; lower laser energies give shallow penetration (Chiang and Albright 1993).

2.4 Welding the Oclaro Fibre Capsule

The Oclaro fibre capsule consists of an outer 304L stainless steel ferrule. The ferrule is inserted into a 304L stainless steel sleeve. The ferrule and sleeve have a sliding fit, as there is an air gap between the two ranging from zero to 20 μm. The sleeve is welded to the ferrule using laser micro-welding.

As illustrated in figure 2.3 (a), initially as the laser fires, most of the incident light is reflected back. The laser is fired at an angle to prevent back reflection. The weld sleeve absorbs the incident focused laser light, which rapidly heats up the surface and initiates the welding process. The surface starts to heat up, and heat is conducted into the bulk. A melt pool starts to form. The surface of the weld sleeve heats up faster than it can conduct the heat away and the steel melts as the laser is pulsed at a high frequency. The surface of the steel sleeve is buffed to ensure the surface shine is removed and is matt. This is done prior to welding to reduce the reflectivity of the steel. During the laser pulse the reflectivity drops from 90% to about 50%, see figure 2.3 (b), as the steel begins to melt. A laser power density of about 10^9 Wm^{-2} is required for welding stainless steel; this value is based on our modelling work (Malik et al., 2006). Heat is conducted into the metal, melting the deeper layers as surface absorption accelerates; there is some heat loss due to conduction.

In figure 2.3(c), most of the incident light is absorbed, with the laser approaching peak intensity. The column of vaporised material extends into the weld. This improves energy absorption. The application of the laser pulse generates significant vapour pressure of the vaporised metallic atoms.

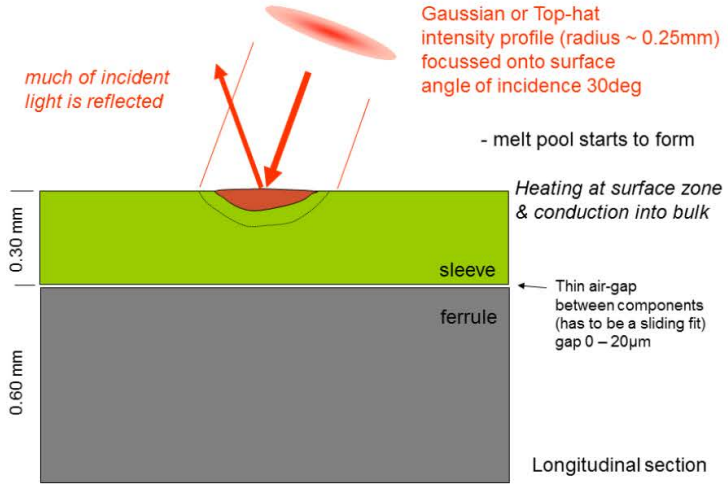

(a)

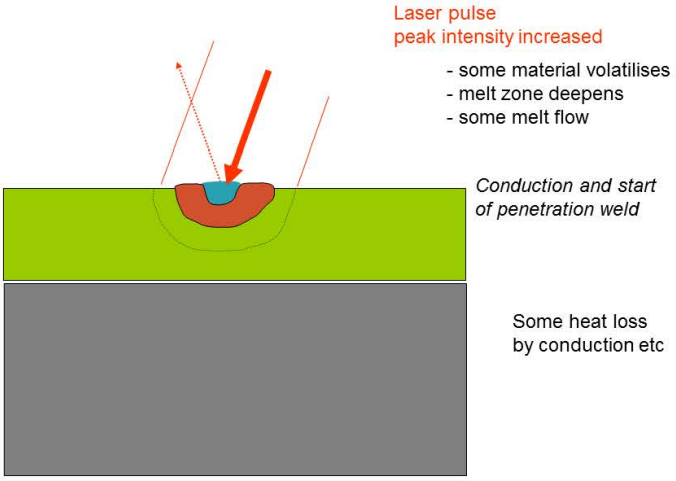

(b)

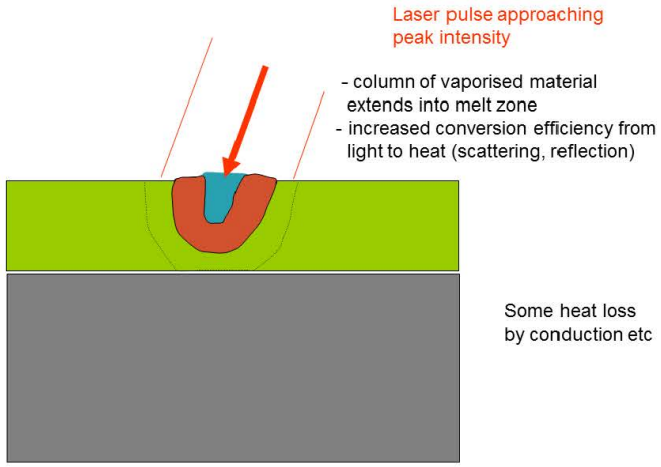

(c)

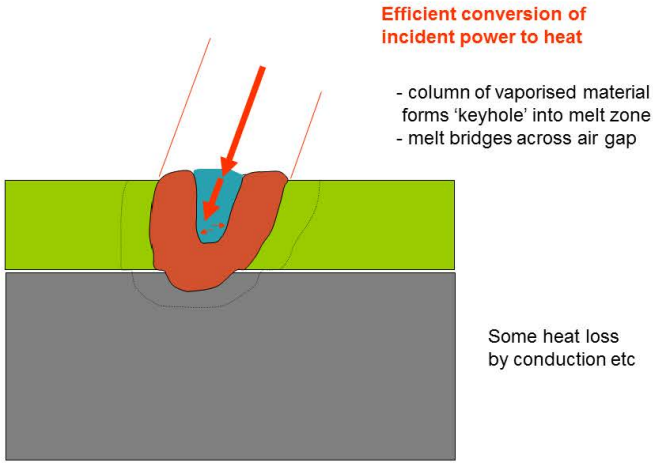

(d)

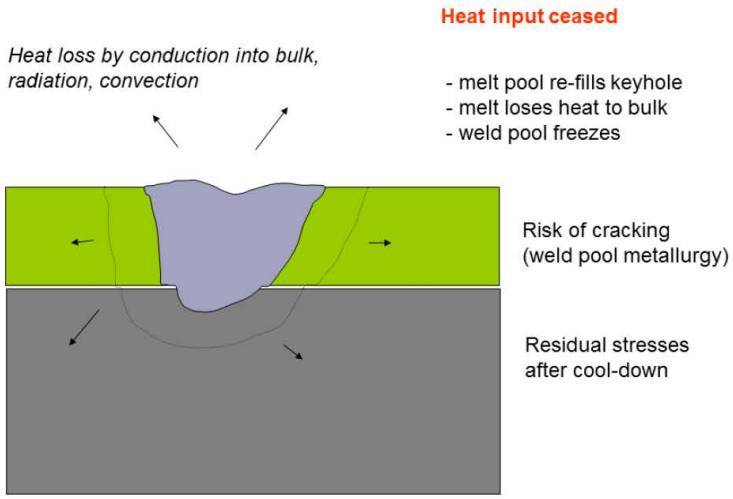

(e)

Figure. 2.3. (a) – (e) The physical process of laser welding, see text above for explanation.

As the metal vaporises a keyhole is created, see figure 2.3(d). The vapour pressure within the keyhole holds back the surrounding liquid metal. The keyhole enhances the absorptivity of the laser beam. The vapour in the keyhole ionizes and absorbs more of the laser radiation, radiating energy to the molten metal along the sides of the keyhole and becomes incandescent. The laser stops firing see figure 2.3 (e), heat loss occurs due to conduction and radiation.

Most welds have an elongated shape, with a heat affected zone (HAZ) that tapers downwards, as illustrated in figure 2.3(e). The aspect ratio of the weld zone is dependent on the spot size, pulse width, and thermal conductivity of the metal. Deeper penetration is achieved by using long pulse widths which are required to effectively transfer energy into the keyhole.

As a laser pulse impinges on metal, because of the localized nature of the HAZ, this allows the joining of metals to take place with minimal thermally induced distortions. The metals are simply made to melt and quickly re-solidify.
When the laser power is low, the dominate mode of heat transfer is conduction, this results in (Bag and De, 2010):-

- A low depth to width ratio.
- A low Pe´clet number (ratio of convected to conducted heat).
- Failure to form a keyhole.

The cooling rate in either instances of low or high laser power depends on:-

- The power of the laser.
- The weld dimensions
- The laser on time.
- The absorptivity of the material to be welded.
    - The absorptivity depends on a number of material and process variables, which leads to difficulties in predicting the joint parameters

The cooling rate of the weld metal also determines the mechanical properties of a weld and hence knowledge of the temperature field of the melt pool is needed for the understanding and modelling of the welding process.

2.5 Thermal Stresses

The weld area heats up rapidly during the welding process. This causes expansion of the weld material which is restrained by the surrounding colder area. The thermal expansion that occurs produces thermal stresses. The thermal stresses are elastic and with cooling the stresses disappear. Due to the high temperature gradient during laser welding the thermal stresses also cause plastic deformations which result in residual stresses after cooling. Residual stresses are internal forces, in equilibrium only with themselves over the whole domain of the body, without external forces (Radaj, 1992).

Since the temperatures are highest in the region near the weld spot, this region expands more than regions further away. During the heating, the stresses in the region near the weld are compressive and plastic because the thermal expansion in this region is restrained by surrounding metal with lower temperature and higher yield stress.

When the welding has been completed and the work piece starts to cool, it deforms in the opposite direction. If the material is completely elastic during the entire period of the heating and cooling phase, the work piece will return to its initial shape with no residual distortions. However, for metals like steel, plastic deformations occur (Connon, 1991).

As a result of the compressive plastic strains produced in the region near the weld spot, the work piece continues to deform after passing its initial shape, which results in a negative final distortion when the work piece cools down to its ambient temperature. The residual stresses are associated with these deformations. Residual stresses exist in a body when there are no external loads or body forces. Hence, residual stresses are also referred to as internal or locked-in stresses (Radaj, 1992, Gatovskii & Karkhin, 1980).

The stresses remaining after all the loads have been removed are the residual stresses, which are equal to or smaller than the yield stress existing after the weld has completely cooled. Residual stresses and welding distortion are two parts of the same problem, namely the thermally induced plasticity. The prediction and control of residual stresses and distortions are crucial in controlling the post weld shift of the fibre capsule.

Stresses due to welding usually occur in two directions, transverse and longitudinal to the weld. Longitudinal residual stresses arise due to a number of reasons. The most common is the longitudinal contraction of the weld as it cools. Transverse residual stresses are generated by the transverse contraction of the weld during the cooling phase. It can also be generated indirectly due to the longitudinal contraction (Connon 1991).

Deformations in and out of plane, as illustrated in figure 2.4, can also occur due to a number of reasons, but are related to the shrinkage of the weld metal during cooling –

- In-plane deformations
    - Transverse shrinkage
    - Longitudinal shrinkage
    - Rotational deformation

- Out-of-plane deformations
    - Angular distortion
    - Longitudinal deformation
    - Torsional deformation
    - Buckling deformation

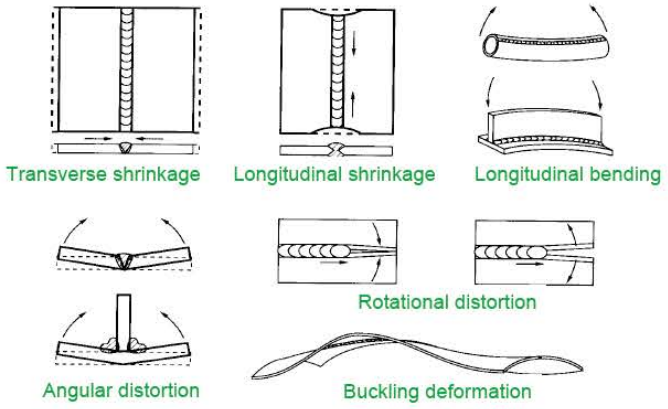

Figure 2.4. (a) Typical distortions that can occur during welding. (Adapted from Connon, 1991)

The stress level in the solidification area is proportionately low, but the stress level in the immediate area increases and can be as high as the yield limit of the base material, which can cause unwanted fractures.

During cooling the material will retrieve its strength, normally at an elevated level due to plastic hardening, which in turn gives rise to the residual stresses. The deformations due to welding are driven by thermal expansion (temporarily) and the residual stresses (permanently). Stress and deformation are largely opposed. A high degree of geometrical restraint in welding results in high stresses and small deformations while an unrestrained weld produces lower stresses but larger deformations.

Residual stresses can be defined as either macro or micro stresses and are ordered according to levels (Withers and Bhadeshia, 2000). Macro residual stresses are also referred to as first order residual stresses. They extend over macroscopic areas and are averaged stresses over several crystal grains. Micro residual stresses can be second or third order stresses. Second order residual stresses act between crystals or crystal sub regions. Third order residual stresses act on the atomic level. It is mainly the first order stresses that are of interest for engineering purposes and thus also in this thesis.

Figure 2.5, shows the changes in temperature and stresses during welding. It is assumed the stresses are uniform in the direction of the plate thickness, as plane stresses are shown. In figure 2.5 (a), the molten weld pool region is shown at *0*, and the weld is indicated by the hatched area. Section *A-A* is in front of the weld bead and shows no residual stresses.

Section *B-B* bisects the melt pool region, section *C-C* which has been welded and is at a close distance from the weld pool. Section *B-B* shows the greatest temperature gradient as it is in the weld pool, figure 2.5 (b).

As a result of welding, residual stresses occur and are shown in figure 2.5 (c). Since the molten metal cannot support any loads, the thermal stress are close to zero in the molten metal. The previously welded metal, where it is cooling, due to the lower temperature and the restrained contraction the stresses are larger. Section *D-D* sees the highest

magnitude of compressive stresses in the weld metal and tensile stresses in the surrounding metal, figure 2.5 (d).

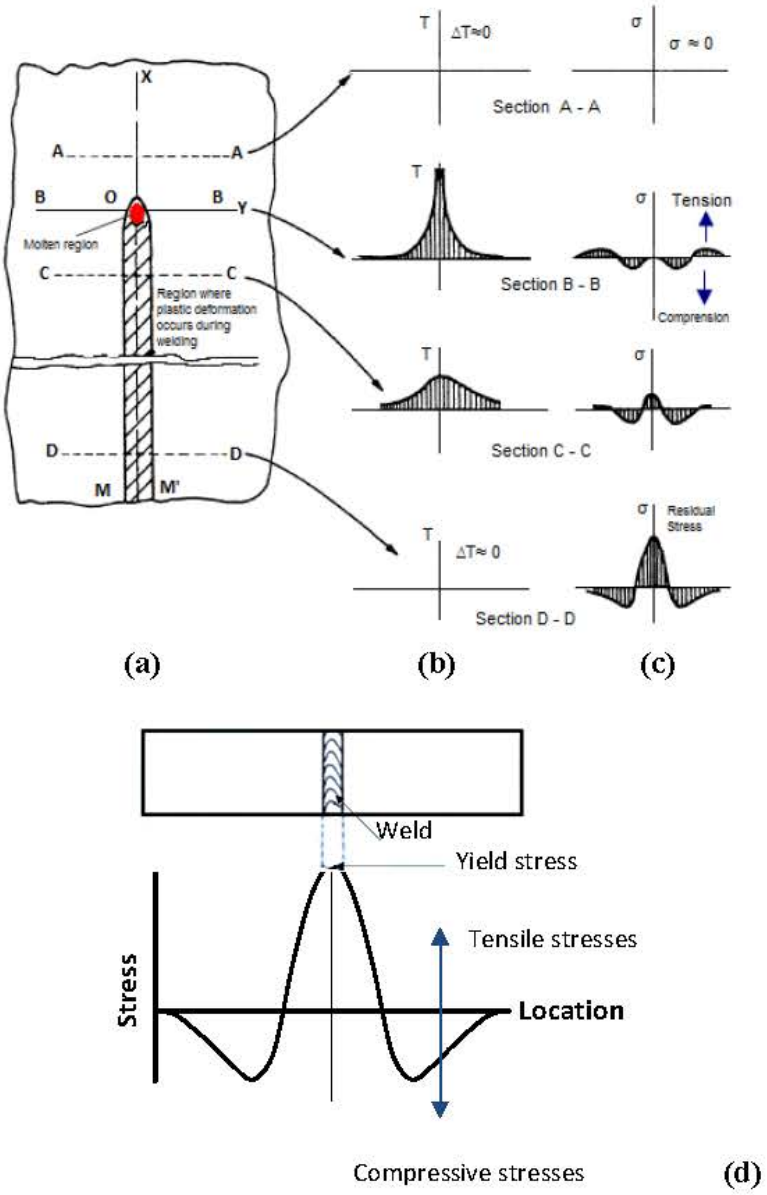

Figure 2.5. (a) Continuous pass butt weld. (b) The associated temperature and (c) stress changes. (Adapted from Feng, 2005). (d) Distribution of stresses in a butt weld. (Adapted from Gourd, 1991).

In the middle of the weld the residual tensile stresses present are very close to the yield point of the parent material (Gourd 1991). The thermal stress as shown at the *D-D* cross section is a typical residual stress distribution. The resultant force and resultant moment

produced by the residual stresses must disappear since residual stresses exist without external forces:

$$\int \sigma \cdot dA = 0 \qquad \textbf{2.2}$$

Where dA is the area on any plane section

$$\int dM = 0 \qquad \textbf{2.3}$$

Where dM is the resultant moment (ASM Handbook 1983).

2.5.1 Modelling Residual Stress

Welding involves a number of complex phenomena that includes heat flow, fluid dynamics, microstructures, deformations, electromagnetism, plasma physics, droplet dynamics just to name a few. A model that takes into account all the physical, chemical and metallurgical effects and their couplings would be very large and complex. In welding, these phenomena are strongly coupled but are not equally relevant or important for all models of the welding process. Hence, welding simulation models tend to be simplified without invalidating the research focus. Generally the simplifications that are used separate the welding process into a number of interrelated coupled fields (Soul and Hamdy 2012). The couplings and their interactions are shown in figure 2.6. The arrows in figure 2.6 indicate the direction and the strength of the couplings. These couplings have been discussed in detail by a number of authors (Soul and Hamdy 2012, Deaconu, 2007, Radaj 1992).

There are strong interactions between two of the main coupled fields in the numerical analysis of residual stresses and distortions in welding. These fields are the heat flow and the mechanical coupling, (Deaconu, 2007), see figure 2.6. The field of microstructure is incorporated into the analysis indirectly in the material description.

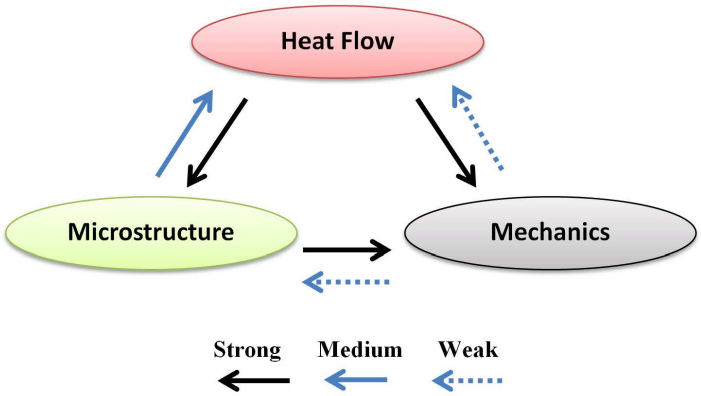

Figure 2.6. Coupling of fields in the numerical analysis of welding (adapted from Deaconu, 2007).

Heat generation due to deformation tends to be ignored because of the weak coupling from mechanics to heat flow. Because of this weak coupling, finite element computer codes generally couple sequentially thermal and mechanical analysis.

Knowledge of the thermal properties and the heat transfer mechanism are needed to calculate the transient temperature field, whereas thermal history and mechanical properties in each location govern the stress field. For such a coupled field problem to provide an exact solutions is not be possible (Koric and Thomas 2008), and numerical methods will provide an approximate solutions.

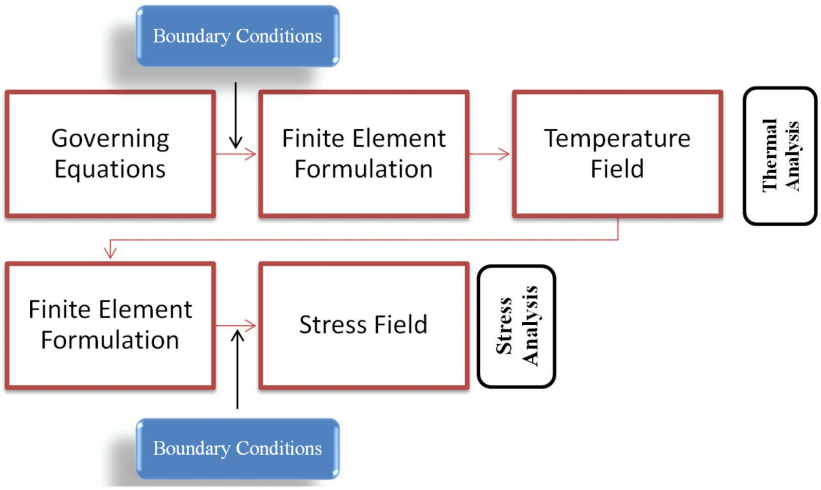

Figure 2.7. Workflow for the coupled field analysis of temperature and stress.

The workflow diagram shown in figure 2.7, illustrates the coupled field analysis for temperature and stress. The boundary conditions for the thermal analysis include the temperature and heat transfer coefficient. The finite element formulation for the thermal analysis will include the capacitance matrix, conductance matrix, and the heat load vector. While the finite element formulation for the stress analysis includes the stress-strain matrix, shape-function matrix and the mass matrix. The boundary conditions for the stress analysis include the constraints in the x, y and z direction.

To estimate the residual stresses in a welding simulation a transient heat transfer analysis is performed. Loading the temperature field which was previously determined a static mechanical analysis is performed. Each time step in the thermal analysis will correspond to a step of the mechanical analysis. The deformation is derived from the thermal dilatation. As the temperatures in the weld region are much higher than in the adjacent regions this gives restrained thermal expansion and causes plastic strains to develop. At the final step when temperatures attain their initial values the residual stress field is obtained as result of all the intermediary analysis steps.

2.6 Characterisation of the Weld

During laser welding there are three different regions that are produced, the fusion zone (FZ), the partially melted zone (PMZ), and the heat affected zone (HAZ), figure 2.8. These regions have been categorized based on the temperatures that occur in the welding process.

During welding, the interaction of the heat source with the base material leads to a series of complex physical processes (De et al., 2003). The material in the fusion zone is completely melted during welding with temperatures surpassing the liquidus temperature and as it cools solidification occurs. It has been determined that the convective heat flow affects the FZ geometry and the temperature distribution in the HAZ (De et al., 2003).

The PMZ is within the fusion boundary where it experiences peak welding temperatures that lie between the solidus and liquidus temperatures of the material (Zhang et al.,

2003) and gives an incomplete melt. This zone tends to be very narrow, and because it has incomplete melting this zone is considered to be part of the heat affected zone.

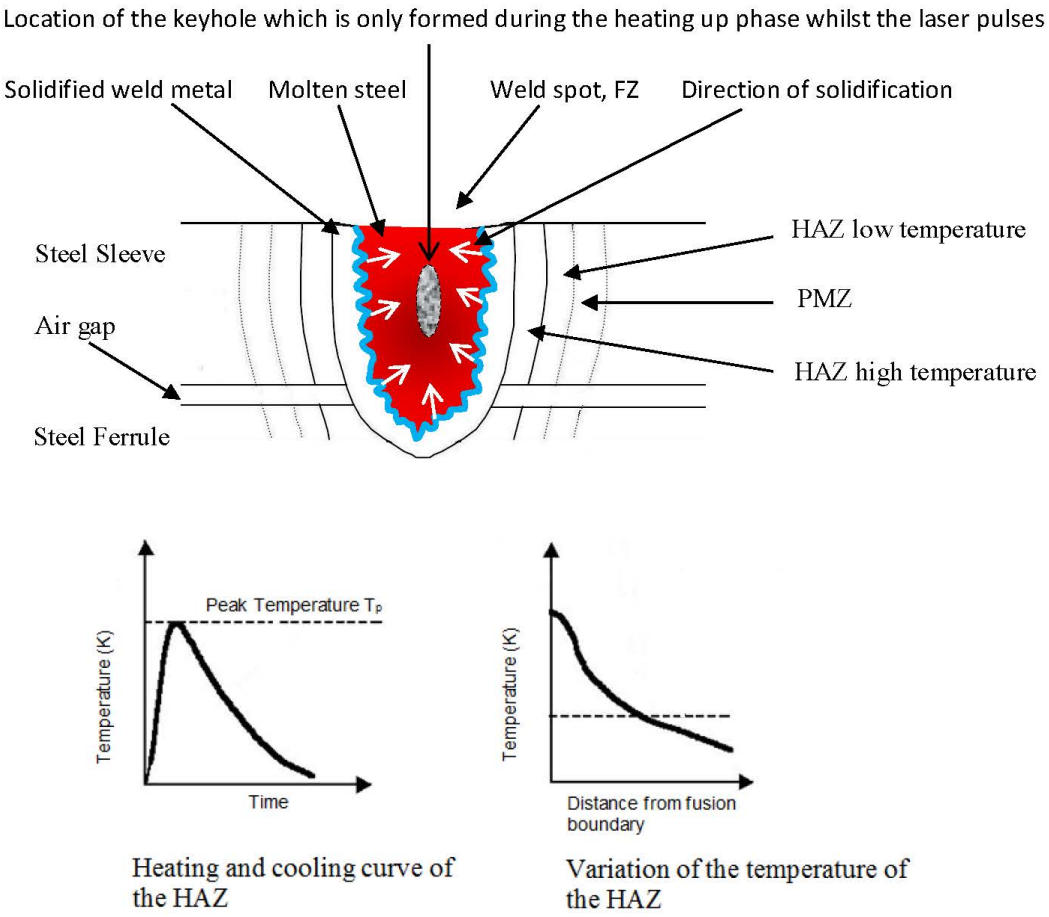

Figure 2.8. Solidification of the weld metal and the formation of the heat affected zones which are not show to scale (adapted from Connon, 1991 and Jin et al., 2012).

The HAZ is the outermost area of the three zones and is divided into a low temperature and a high temperature region. The HAZ is characterized by its softness and in laser-welded joints is narrow. This softened region is defined as the area where hardness values fall below 90% those of the base metal.

2.7 Laser Heat Distribution

The heat from a focused laser spot incident on a metal surface is conducted away from the heated area into the body of the metal. The material diffusivity, k, of the metal is determined by the thermal distribution–

$$k = \frac{K}{\rho C} \qquad \textbf{2.4}$$

Where –

K = thermal conductivity $Wm^{-1}K^{-1}$

C = heat capacity $Jm^{-1}{}^{\circ}C^{-1}$

ρ = density kgm^{-3}

So, for a constant heat source applied for time *t*, the thermal diffusion distance is given by:

$$D = \sqrt{m_d t} \qquad \textbf{2.5}$$

Where –

D = thermal diffusion

t = time

m_d = material diffusivity

The penetration depth of the weld can be estimated using the thermal diffusion distance (Lankalapalliy et al., 1996), which provides a measure of the heat distribution in the metal. To determine a certain depth of penetration, the thermal diffusion *D* can be used to determine the pulse width of the beam. Hence, smaller the value of *k* for a metal, the smaller the heat zone it has and hence there is more efficient use of the laser energy for heating.

Spot size selection is also influenced by the material diffusivity, *k*. The diameter of the weld pool should be smaller than the penetration depth of the laser pulse in order to form a good weld. Fibre optic beam delivery of the laser spot whose size is fixed by the core of the fibre and hence the pulse width will directly control the depth of penetration in most lasers.

Metals with a lower material diffusivity, *k*, and a lower reflectivity are good candidates for laser welding. With metals of high reflectivity the laser energy has to be high for sufficient energy to be absorbed by the metal to melt it. Once molten, absorption is increased and leads to vaporization of the metal leading to a violent reaction creating air pockets and poor welds. Hence, there are limits to the amount of energy which can be

used as this affects the quality of the weld. Alloys such as stainless steels, which is good at absorbing laser radiation, is a good candidate for laser welding, whereas pure metals such as gold and copper which have high reflectivity are poor candidates for laser welding.

2.8 Laser Energy Absorption Efficiency

During welding, only a fraction of the energy is transferred from the heat source to the work piece. The amount of energy transferred directly affects the shape and size of the weld pool and the temperature distribution in the HAZ (Zhang et al., 2003).

The absorption efficiency is equivalent to the absorptivity of the work piece material during conduction mode laser welding. The absorptivity is related to the substrate resistivity and the wavelength of the laser radiation by the following equation (Bramson, 1968):

$$\eta(T) = 0.365\left(\frac{e_r}{\lambda}\right)^{1/2} - 0.0667\left(\frac{e_r}{\lambda}\right) + 0.006\left(\frac{e_r}{\lambda}\right)^{3/2} \qquad \textbf{2.6}$$

Where η is the laser absorptivity at temperature T and wavelength λ, and e_r is the electrical resistivity. For 304L stainless steel the average electrical resistivity is 80 μΩcm (Davis, 1998). Substituting the value of 1.064 μm, the wavelength of a Nd:YAG laser, into equation 2.6 gives a value of 0.27 for the absorption coefficient.

Equation 2.6 indicates that the absorption of the laser energy becomes more efficient as the laser wavelength decreases. There are several other factors such as the nature of the surface, the joint geometry, the concentration of volatile alloying elements in the base material that also affect the absorption efficiency of laser beam energy (Bramson, 1968). However, Fuerschbach (1996) found the absorption efficiency to be almost independent of the composition and physical properties of the substrate material in the keyhole mode.

2.9 Laser Gaussian Heat Source

It is important to know how the heat energy is distributed over the surface of the weld, since the distribution of heat input has a direct influence on the weld pool geometry. For

laser spot welding, the following Gaussian distribution has been widely used to account for the heat flux at the weld top surface (Zhang et al., 2003):

$$H_{in} = \frac{fP\eta}{\pi r_b^2} e\left(-\frac{2r^2}{r_b^2}\right) \qquad \textbf{2.7}$$

H_{in} = Heat input on the surface (Wm^{-2})

f = Heat distribution factor, which in laser welding is taken as 3.0 (Chan et al, 1986)

P = Laser power

r_b = Beam radius

$r = \sqrt{(x^2 + y^2)}$ is the radial distance of any point from beam centre on the surface of the material, where x and y are the Cartesian coordinates of that point

η = absorption coefficient, is calculated using equation 2.8:

$$\eta = q_t(1 - \rho_s) \qquad \textbf{2.8}$$

Where –

q_t = The fraction of laser energy transmitted through the top surface

ρ_s = The fraction of laser energy reflected from the top surface of the lower material

The reported values of the absorption coefficient vary, and range between 0.21 – 0.62 (Fuerschbach and Norris, 2002).

2.10 General Heat Equation

One of the objectives with heat transfer analysis in welding applications is to determine the temperature fields in the work piece resulting from conditions imposed on its boundaries. The temperature distribution represents how temperature varies within different locations in the work piece.

The temperature fields of a work piece can vary from ambient to in excess of the evaporation temperature of the metal. Within this range phase changes, micro structural transformations and thermal strains take place, all of which determine residual stresses and distortion. When the temperature distribution is known, the conduction heat flux

calculated at any point in the material or at the surface may be computed from Fourier's law (Incropera and DeWitt, 1996).

The general form of the heat diffusion equation in Cartesian coordinates –

$$\frac{\partial}{\partial x}\left(k\frac{\partial T}{\partial x}\right)+\frac{\partial}{\partial y}\left(k\frac{\partial T}{\partial y}\right)+\frac{\partial}{\partial z}\left(k\frac{\partial T}{\partial z}\right)+\dot{q}=\rho c_p\frac{\partial T}{\partial t} \qquad 2.9$$

This equation, (2.9), is known as the heat equation and provides the basic tool for heat conduction analysis. This equation states that at any point in the medium the net rate of energy transfer by conduction into a unit volume plus the volumetric rate of thermal energy generation must equal the rate of change of thermal energy stored within the volume. The direction coordinates are given by x, y and z, the temperature is T, time is t, C_p is the specific heat, ρ is the density and q is the thermal energy generation.

2.11 Analytical Modelling

There has been extensive work done on laser welding modelling. The majority of these models are based on the theory of heat flow due to a moving heat source which was given by Rosenthal in 1946 (Carslaw and Jaeger, 1997).

All the basic analytical solutions are based on the solutions for the heat conduction equation (Fourier's law). Most models which are based on analytical solutions have been described by Carslaw and Jaeger (1997). These two researchers have suggested a general three dimensional heat transfer equation.

$$\alpha\left(\frac{\partial^2 T(x,y,z,t)}{\partial x^2}+\frac{\partial^2 T(x,y,z,t)}{\partial y^2}+\frac{\partial^2 T(x,y,z,t)}{\partial z^2}\right)=\frac{\partial T(x,y,z,t)}{\partial t} \qquad \mathbf{2.10}$$

Where, T is the temperature, t is the time, α is the thermal diffusivity, and, x, y, and z are the coordinates.

One of the earliest analytical solutions for welding (Carslaw and Jaeger 1997), used a point source which was incident on an infinite material and was moving relative to it. The geometry for simulating heating by conduction and surface melt is shown in figure 2.9.

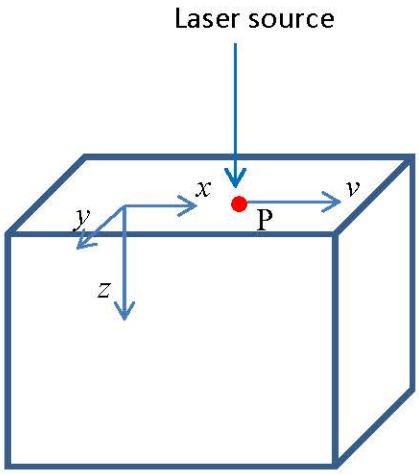

Boundary conditions are:

$$\frac{\partial T}{\partial x} = 0 \ as \ x \ \to \infty;$$

$$\frac{\partial T}{\partial y} = 0 \ as \ y \ \to \infty;$$

$$\frac{\partial T}{\partial z} = 0$$

Figure 2.9. The model geometry that uses a moving point source of heat to simulate laser welding, with the given boundary conditions.

The three dimensional heat transfer equation, equation 2.10, can be re-written for a point source moving at a constant velocity in the x-direction, equation 2.11.

$$\alpha\left(\frac{\partial^2 T(\beta,y,z,t)}{\partial \beta^2} + \frac{\partial^2 T(\beta,y,z,t)}{\partial y^2} + \frac{\partial^2 T(\beta,y,z,t)}{\partial z^2}\right) = v\frac{\partial T(\beta,y,z,t)}{\partial \beta} + \frac{\partial T(\beta,y,z,t)}{\partial t} \qquad \textbf{2.11}$$

The distance from a point to the point source, β, is given by equation 2.12. Where velocity is given by v,

$$\beta = x - vt \qquad \textbf{2.12}$$

For a quasistationary heat flow, this can be defined by:

$$\frac{\partial T(\beta,y,z,t)}{\partial t} = 0 \qquad \textbf{2.13}$$

By substituting equation 2.14 into equation 2.12 and then simplifying:

$$T = T_0 + e^{-\beta v \lambda} \varphi(\beta, y, z) \qquad \textbf{2.14}$$

The initial temperature is T_0, and to calculate the temperature distributions φ is the function which needs to be determined.

$$\left(\frac{\partial^2 \varphi(\beta, y, z)}{\partial \beta^2} + \frac{\partial^2 \varphi(\beta, y, z)}{\partial y^2} + \frac{\partial^2 \varphi(\beta, y, z)}{\partial z^2}\right) - \left(\frac{v}{2\alpha}\right)^2 \varphi(\beta, y, z) = 0 \qquad 2.15$$

By using appropriate boundary conditions these equation can be solved to give the temperature profiles for an infinite and semi-infinite solid using a moving heat point source. The solution of the heat transfer equation for three-dimensions is given by:

$$T - T_0 = \frac{Q}{4\pi k} e^{-\frac{v\beta}{2\alpha}} \frac{e^{-\frac{v\beta}{2\alpha}}}{R} \qquad 2.16$$

The solution of heat transfer equation for two-dimensions is given by:

$$T - T_0 = \frac{Q'}{2\pi K} e^{\frac{v\beta}{2\alpha}} K_0\left(\frac{vR}{2\alpha}\right) \qquad 2.17$$

Where Q' gives the rate of heat per unit length, Q is the rate of heat, K is the thermal conductivity, and R is the distance to the heat source. Unfortunately this solution gives incorrect results for temperatures near or within the experimental beam diameter. Bunting and Cornfield's solution (1975) has been able to overcome these limitations by using a cylindrical heat source, or by using a finite element or finite numerical method.

The standard moving heat source solution was simplified by Swift-Hook and Gick (1973). Their model consisted of a moving line heat source to represent a continuous laser weld. To get the shape of the fusion zone, this was indicated by the location of the isotherm that corresponded to the melting temperature.

The keyhole plays an important role in laser welding and was neglected in these earlier models. Klemens (1976) was one of the first to incorporate the formation of the keyhole into laser welding modelling. A moving cylindrical vapour-filled cavity (keyhole) formed by continuous vaporization of material due to a laser beam was assumed in the model. The shape of the cavity was determined by a balance of the liquid flow and surface tension, which tends to close the cavity, and the continuous vaporization which tends to maintain the cavity. Based on the heat flow, vapour flow, surface tension, and gravity the model only gives the qualitative analysis of the variation of the cavity radius with the depth and the shape of the molten zone.

Andrews and Atthey (1976) further investigated the keyhole during laser welding. Their model consisted of a stationary beam and a semi-infinite molten weld pool. Gravity and surface tension effects were taken into account to predict the depth and the profile of the keyhole. The model assumed that vapour pressure inside the keyhole cavity was equal to the atmospheric pressure and neglected the vapour pressure distribution inside the keyhole. Additionally, the model assumed that there was no reflection from the surface and at the surface all the incident radiation was absorbed without any attenuation by the plasma. Also, there was no conduction and the entire absorbed energy was assumed to be used for evaporation and gravity was assumed to be the only restoring force. If the surface tension is included it reduces the depth of penetration (Andrews and Atthey 1976). This model is not suitable for predicting the temperature distribution during laser welding as it neglected heat conduction.

A model that analysed the temperature distribution, cooling rate distribution, and depth of melting as a function of various laser parameters due to a moving Gaussian beam, that included heating and melting regimes was proposed by Cline and Anthony (1977). This was a more realistic of model laser welding that assumed that the onset of penetration welding occurred when the surface temperature reached the boiling point. This was extended to model deep penetration welding.

By calculating the keyhole profile, deep penetration welding has been modelled (Kaplan 1994). This was done by finding the energy balance at the keyhole wall point-by-point.

Using the theory of heat flow by a moving line source of heat, the heat conduction of the keyhole was modelled.

To model experimental weld shapes Steen et al., (1988) used Rosenthal's solution for a point source on the top surface to model the broadening of the weld. The solution for a moving point source was used to derive a solution for a line source as the source strength varied along the length of the line (Akhter et al., 1989).

To model the shape of the fusion zone Resch and Kaplan (1998) used the solution from Akhter et al., (1989). The weld pool shape was determined from the profile of the melting isotherm (Hilton 1995), by using an analytical solution to the heat conduction equation.

The majority of models that involve the analysis of the keyhole assume that the keyhole is symmetric and either coaxial with the laser beam or displaced slightly. Moreover, these models assume that the surface tension pressure and the recoil pressure will determine the stability of the keyhole. For these assumptions to be true the models further assume that the keyhole remains within the area of the laser beam (Dowden and Kapadia 1995; Kaplan 1994).

2.12 Numerical Solutions

There are limitations that apply to analytical methods. However, numerical techniques are free from such limitations. This is because the volume to be analysed is broken down into smaller (control) volumes. Each of these volumes has its own values of heat input, thermal conductivity, density, and so forth. As has been discussed with analytical methods the heat source is concentrated in a point, line or plane, which does not apply to numerical methods. Real boundary conditions and temperature-dependent thermo-physical properties can be included in numerical methods. Additionally, numerical techniques can reveal the effect of different phenomena on the process as more detailed physics of the problem can be included.

The boundary element (Brebbia and Partridge 1992), finite difference (Becker 2004, Versteeg and W. Malalasekera 1996, Shyy et al., 1997), and finite element (Patankar

1982, Becker 2004), methods are the main numerical techniques, and work by solving the basic conservation equations such as Fourier's second law. Numerical techniques have advantages and have resulted in having models developed for heat flow in laser welding, and for many of the existing weld process. However, there has not been wide spread development of numerical models. There are two mains reasons for this. Such models do not easily show general trends and there is complexity in building such models.

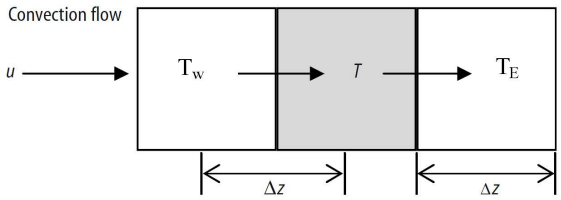

Figure 2.10. Example for the finite difference equation

For these methods a differential equation is defined into a finite difference form. For example, using Fourier's law, the element in figure 2.10, could be either heating up or cooling down:

$$\alpha \frac{\partial^2 T}{\partial z^2} = \frac{\partial T}{\partial t} - u \frac{\partial T}{\partial z} \qquad \textbf{2.18}$$

In finite difference form this is:

$$\alpha \left(\frac{((T_W - T)/\Delta z) - ((T - T_E)/\Delta z)}{\Delta z} \right) \approx \frac{T' - T}{\Delta t} - u \left(\frac{T_W - T_E}{2\Delta z} \right) \qquad \textbf{2.19}$$

Where T_W and T_E is the temperature in the "west" and "east" element, see figure 2.10. After one time interval, Δt, the temperature, T', is

$$T' = \left(u \left(\frac{T_W + T_E}{2\Delta z} \right) + \alpha \left(\frac{T_W - T_E - 2T}{\Delta z^2} \right) \right) \Delta t + T \qquad \textbf{2.20}$$

This equation, equation 2.20, is solved in its three dimensional version. The two gradient terms are centred on the time when $t = t$, which causes instability. To overcome this problem the Crank–Nicholson method is used.

The time term may be dropped and the solution is found using a process known as "relaxation" (Mazumder and Steen 1980). Mazumder and Steen (1980) produced one of the first laser welding models. It was a three dimensional model in which they assumed a Gaussian heat source with 100% absorption of the power, the work piece was of infinite length and the temperatures were in excess of the boiling point with radiative and convective heat loss. This model was then modified by Chande and Mazumder (1981), who took into account the radiative and convective heat loss, the latent heat of phase change and temperature dependent material properties.

The boundary element method was used (Lim and Chan 1995) to model deep penetration welding in one dimension. Lubrication theory was applied to the liquid region and non-equilibrium vaporisation; the solution was combined with each region using the boundary conditions.

To find the thickest work piece that could be welded with full penetration a formula was derived by Dowden and Kapadia (1995). Their model assumed a keyhole with a diameter three times bigger on the top surface than the bottom surface. They verified their results by comparing them with experimental work, and found good agreement.

Using the model of Hamoudi and Ducharme (1996), Norman et al., (1998) developed a model to calculate the growth rates of welds, the thermal gradients and temperature field. From this data they were able to predicate the cooling rates which they found in reasonable agreement with experimental data.

A hydrodynamic physical model of laser–material interaction was developed (Semak et al., 1999). This model included the effect of convection on melt flow and the effect of evaporation recoil pressure. It was found that at intensities corresponding to laser welding, cutting, and drilling due to melt ejection that the convective heat transfer

induced by recoil pressure was significant. The simulations also showed a secondary temperature maximum due to the motion in the molten zone outwards from the beam.

2.12.1 Current Numerical Models

The above numerical models are of note, primarily as they led to further developments in the field of numerical analysis of laser welding. Some contemporary models will now be mentioned to indicate the current state of the art that is used in investigating various phenomena associated with laser welding.

Using numerical analysis Cho et al., (2012) identified a number of laser welding properties. They found simulations that used a measured beam profile and a Gaussian-like beam profile produced similar results for the molten pool and the shape of the fusion zone. They concluded that using a Gaussian-like beam in a simulation did not diminish the accuracy of the simulation. The also concluded from their work that the effects of the Marangoni force in keyhole laser welding is insignificant.

To measure the melt pool shape and to gain the temperature distribution of the keyhole, Wang et al., (2011) developed a three dimensional computational procedure for this. They found that the recoil pressure is the main driving force for keyhole formation. Additionally, they found that large temperature gradients occurred on the surface of the keyhole.

To compute the thermal phenomena during pulsed laser welding, two numerical models were developed as a confirmation (Sabbaghzadeh et al., 2008). One of the models was developed using finite difference and the other using finite element. Sabbaghzadeh et al., were able to confirm that the pulse parameters of the laser beam determined the temperature contours and the depth of penetration.

For the work discussed so far not all of the parameters influencing the welding process have been implemented in a numerical analysis. A three dimensional finite element model has been developed for butt joining of thick AH36 shipbuilding steel plates (Tsirkas et al., 2003). The work considered a Gaussian distribution heat flux with a moving heat source conical in shape that modelled a keyhole formation. The thermal

solution was derived from a quasi-steady-state. The temperature dependent material properties and metallurgical transformations were also taken into consideration. Mechanical analysis was included by using a thermo-elasto-plastic material formulation with von Mises yield criterion coupled to a kinematic hardening rule. The work concluded that the welded panel distortions from the FEA agreed with their experimental measurements.

There are a number of published works on numerical laser welding; some of them have been discussed above. Currently published work shows that several improvements have been made to the work discussed above, and include:

- The development of hybrid analytical and numerical models.
- The use of adaptive meshing and remeshing schemes.
- Incorporating into the model an experimentally predetermined intensity profile of the laser beam.

2.13 Post Weld Shift

The optoelectronic package containing the laser diodes including pump lasers can come either as a 14-pin butterfly package or dual-in-line package. In both cases the optical fibre is attached to the laser diode package to couple the laser diode waveguide to the fibre. This process whereby the optical fibre is aligned with the laser diode and is fixed in place is also referred to as fibre pigtailing. The alignment tolerances required for optimum light coupling between the laser waveguide and the optical fibre need to be precise with a typical accuracy in the submicron range. Once the alignment of the fibre and the laser waveguide has been optimally coupled they are fixed it place. Methods such as soldering and epoxies can be used. More commonly laser welding is used, due to its long term reliability and ruggedness (Mobarhan et al., 2000 and Mueller and Valk 2000). Laser welding also has a number of other advantages which include precise positioning of the weld spots, local heating of the joint parts, narrow heat affected zone, ease of automation, high welding speed, enhanced design flexibility, clean, high energy density, low heat input and an efficient process (Zhou & Tsai, 2008; Kazemi & Goldak, 2009). Also another key features is the ability to weld without filler materials which is considered a distinct advantages (Pang et al., 2008)

The rapid solidification of the laser weld spots causes material shrinkage. This causes misalignment of the optical fibre and laser source and is known as post weld shift (PWS), and has also been referred to as welding-induced-alignment-distortion (WIAD). The PWS is typically in the range of a few micrometres to over 10μm (Song et al., 2009). This is the main disadvantage of laser welding. The previously aligned components are misaligned from their optimum relative position as the molten metal of the weld solidifies. The solidification creates shrinkage forces that cause the shifting of the components and reduces the light coupling efficiency. The minimizing of PWS is one of the greatest challenges for the packaging of optoelectronics. Within this area research concentrates on the minimizing the PWS and of accurately predicting it (Shaw et al., 2001, Kuang et al., 2000, Park et al., 2000).

A number of papers have been produced discussing PWS. Of the earlier work only thermal analysis was used, the more recent papers include thermomechanical coupling. Most of the models tend to focus on butt and lap welding of the optoelectronic package. Additionally, all the work concentrates on either the TO (transistor outline) can or weld clip geometry, see figure 1.3. None of these geometries relate to the Oclaro package geometry that was used in this work, although the OPISA methodology can be applied to the other geometries.

Frewin and Scott (1999) compared the simulated temperature profile and the shape of the melted zone, and discuss the use of defocusing the laser welding beam on penetration depth and the weld spot diameter. The temperature variations against time as well as position of the spot weld are discussed by Yeung and Thornton (1999) for the transient thermal behaviour of spot welding. Cheng et al., (1997) studied the penetration depth of welding at different gold thickness coating of Invar-Invar joints. They used a two dimensional axisymmetric model to study the penetration depth of welding at different gold thickness. They compared the experimentally measured penetration depth and width of the weld zone with the simulated temperature profile. The work that has so far been discussed used a single weld spot and no mechanical analysis was done. Hence, PWS caused by mechanical deformation of the weld structure and the use of multiple weld spots had not be studied by these researchers.

Using a modified model of Cheng et al., (1997), Kuang et al., (1999) used it to study the mechanism of crack formation and von Mises stresses. With further work this group (Kuang et al., 2001) developed a two dimensional model with two weld spots that included thermal-plasticity. They studied the effect of forming the weld spots using a balanced and unbalanced laser energy beam, and discussed the deformation of structures with nodal displacement.

A three dimensional model has been developed (Deshayes et al., 2003), to study PWS by thermomechanical analysis and the fatigue life of a dual-in-line package. The study used electrical resistance that produced Joule heating to approximate laser heating. Using different heat source equations to describe the laser heating process and using volume heating instead of surface heating transient PWS has been studied (Chang et al., 2002). Different weld spots due to conduction welding and keyhole welding were obtained, and discussed in relation to PWS.

The study of weld spot location and unbalanced welding laser energy has be investigated (Labudovic et al., 2003), by using a three dimensional model. It was found that the simulation was able to predict PWS when compared to experimental data. Furthermore the study concluded that misalignment can be minimized by control of the laser beam energy delivery system.

Lin et al., have done a series of experiments to investigate PWS. The have shown (2003, 2005) that the shape of the pulse and the welding sequence influence PWS. They concluded that PWS can be minimised by using an appropriate laser pulse shape and laser welding sequence. This group of researchers (Lin et al., 2007) has shown that the design of the weld clip that is used affects PWS. They used seven different types of weld clips which they analysed using FEA. They concluded that PWS was controlled within a minimal range by an appropriate design of the weld clip and the laser welding sequence.

Others have relied upon experimental techniques (Song et al., 2009) to compensate for PWS. This is done using a laser hammering technique that relies upon the sequencing of the weld spots. After sequencing the weld spots misalignment due to the PWS were

compensated by laser hammering. Finite element analysis has been performed to verify this (Kuang et al., 2012). The criticism of this technique is that it increases the assembly time and hence increases production costs.

2.14 Conclusion

This chapter has fulfilled the first two objectives. The chapter detailed a review of the background to the theoretical aspects of laser welding. The chapter starts with a review of the thermomechanical aspects of the laser welding process, how laser welding occurs. A number of complex physical phenomena are involved. Starting from the heating of the metal surface by Fresnel absorption, the absorption of the laser energy is governed by the Beer-Lambert law. At the atomic level there is an understanding of how the material heats up due to the Bremsstrahlung effect.

Specifically there are two modes by which laser welding occurs. The mode is dependent on the power output of the laser. Conduction mode welding produces shallow wide weld spots, at lower laser power. Keyhole mode welding produces deep narrow weld spots, and requires higher laser power.

During laser spot welding a local area is heated up rapidly resulting in high thermal gradients. This results in a non-uniform temperature distribution. The work piece expands as a result, but the expansion is restrained by the surrounding cooler bulk. As a consequence this gives rise to thermal stresses. Plastic strains develop in the weld region due to the yield limit being lower in the area of elevated temperature.

The hot metal in the weld zone contracts during cooling, causing the joint to shrink. The cold metal surrounding the joint restrains the contraction. Plastic deformation occurs due to stresses which are in excess of the yield stress, causing buckling or distortion.

In the melted weld pool stresses are released and can be assumed to be zero. During the solidification of the weld pool the metal starts to shrink and to exert stresses on the surrounding weld metal and HAZ. These stresses remain in the material after welding

and result in unwanted distortion. The residual deformations are usually called welding distortions.

There was a review of the literature of how other researchers in the field modelled the laser welding process using analytical and numerical techniques. Numerous analytical models have been published and the majority are based on the solution for a line or point source. Using numerical techniques a number of issues that plague analytical techniques have been overcome. However, numerical methods are not without their own issues. Nevertheless numerical techniques are the method of choice in welding research.

There is a lack of research that explains the physical relationship between the parameters of the heat source and the final weld shape and size. Additionally, as of yet it there may be other welding parameters that influence the formation of the weld shape. The heat source used for welding simulations may probably be limited to apply to certain types of welding processes since accurate welding parameters replace the estimation of the weld shape. Due to these limitations a predetermined heat source model is generally used. This allows defining the laser heat source for accurate welding simulations. To define the heat model for a welding simulation measurements which include the size and shape of an existing weld spot are used.

Where the interest of the simulation is heat and fluid flow and their effects on the formation of the melt pool, complex welding heat transfer has to be incorporated. This will take into account solid, liquid, and gas heat energy exchanges and will allow for better prediction of the final weld shape (Ion 2005, Moraitis and Labeas 2008).

The literature on laser welding shows that for solid mechanics calculations thermo-fluid computations are not generally performed together. These are two very different simulations that require a fully coupled thermo-fluid and thermomechanical analysis integrated together.

Numerical modelling and simulation of welding is a difficult and challenging problem due to the complex mechanisms involved. The different physical phenomena of the welding process have been generalized into the fields shown in figure 2.6. The fields are

strongly interrelated and couple with each other. The creation of a numerical model that accounts for all the physical effects and their couplings would be large and complex. However, such a model has been produced (Tsirkas et al., 2003). The work did not produce any overwhelming results to suggest that such an all-encompassing simulation yields better results. By use of appropriate assumptions welding research focuses on a particular area of welding without incorporating all the physical phenomena. Thus welding research is to choose simplifications without invalidating the research focus.

The review of the current work being conducted in post welding shift indicates that work has been done using both experiments and FEA. The emphasis naturally is on the reduction of PWS. The two main features of the research have been focused on either using optimum component geometry or on post welding realignment methods to reduce PWS. Neither of these has been satisfactory in giving the type of results that would be usable within an industrial setting. As such this research is still on going.

Chapter 3

Surrogate Modelling Technologies

This chapter covers the third objective to review the tools and techniques used to develop the surrogate model of the micro laser welding process. Additionally, there is a review of the use of design of experiments and response surface methodology in welding research. These tools and techniques, of which there are a number, were used to develop the OPISA methodology. They generally fall within the domain of design of experiments and response surface methodology and are used to develop the surrogate model, and will be discussed in this chapter.

3.1 Design of Experiment

For a surrogate model to link the inputs to the outputs, this is derived empirically from the experimental data. To develop such a model empirical work in the form of experiments are performed. In an experiment, in order to observe the effect on the response, one or more process variables, called factors, are changed. Ordinarily one factor is changed at a time to see its effect on the response. This is inefficient, and does not take into consideration the effect of interaction between the factors. A more robust and efficient technique that allows the changing of several factors at the same time is the statistical design of experiments (DoE).

The use of DoE starts with a discovery phase, where the factors of interest are identified, figure 3.1. Usually experimenters cannot always be sure which factors are of statistical significance. So a list of factors is identified by expert opinion. This can result in a large number of factors. Where there are numerous factors screening experiments can be used to whittle them down and identify the statistically significant factors.

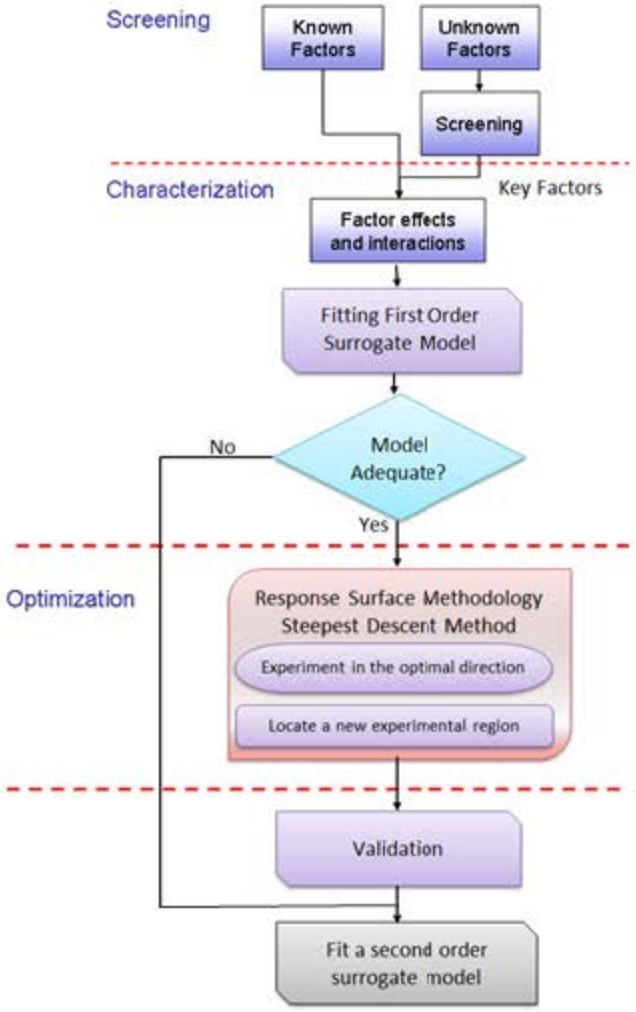

Figure 3.1. An outline of the methodology used to develop the surrogate model.

Either full factorial or if there are many factors or if material is not readily available then a fractional factorial experiment can be conducted. For this study screening experiments were not used, as only five factors were identified that were thought to contribute to stress generation in the fibre, and would be screened during the sensitivity analysis. There were other factors, however they would not have been amenable to any form of change, as they were necessary for the setup of the laser welding equipment.

The characterization phase, figure 3.1, identifies the interactions between the factors, which will require a higher resolution if fractional experiments had been performed, or possibly full two level factorial experiments. Up to this point approximately 80% of the processes capability can be identified (Myers et al., 2004). Even if there is curvature in

the system, the process can be optimised using response surface methods (RSM), which is the optimisation phase. The central composite design (CCD) and the Box-Behnken design (BBD) are the tools that can be used to develop a response surface (Montgomery, 2012). In this work a second order model was not developed. However, if the first order model is inadequate a second order model will need to be developed.

The optimisation phase consists of building a response surface surrogate model. This is created from the design of experiment data. The response surface of the process is traversed using a steepest descent (or ascent) algorithm to find a new location on the response surface where the process is at its optimum.

The final step is the validation, which requires using the optimised levels of the factors that have been identified, to verify the results of the experiment. The next phase would be to develop a second order model, which currently is not considered in the OPISA methodology. If the curvature is strong in the surrogate model, a second order surrogate model needs to be developed.

3.1.1 Surrogate Model Assumptions

In any model building process assumptions are made. There are two assumptions of particular of interest in general and will be discussed here.

Surrogate models that are polynomial approximations are only suitable for smoothly varying outputs. So that outputs over the experimental range must be continuous and should be reasonably smooth. Since a sharp fall in the response values will be missed by an approximating polynomial, as polynomials assume that the underlying response surface is a smooth curve.

For a piecewise smooth response surface, the experiment has to be broken up into a series of experiments which investigates each shape separately. A jagged, non-smooth surface cannot be successfully approximated by a polynomial.

The other assumption checks if the residuals are well-behaved (Montgomery et al., 2006). A residual is the difference between the observed and predicted response, and

gives the experimental error. The experimental data is used to estimate the parameters of the model, and it is the model that is used to predicate the responses. The inspection of residuals indicates if the surrogate model is appropriate and the assumptions are reasonable.

3.2 Tools and Techniques

A number of methods are used to analyse the DoE data, develop the surrogate model and to ensure its validity. All these methods require that the data to be normally distributed. The methods that are used are summarised in figure 3.2.

The initial step before any work can proceed requires the checking of the DoE data to ensure that it is normally distributed, for which the Anderson-Darling (Stephens 1974). test is used. If the data is non-normal, the data can be transformed by using a Box-Cox transformation or a Johnson transformation, which are standard and well established statistical procedures.

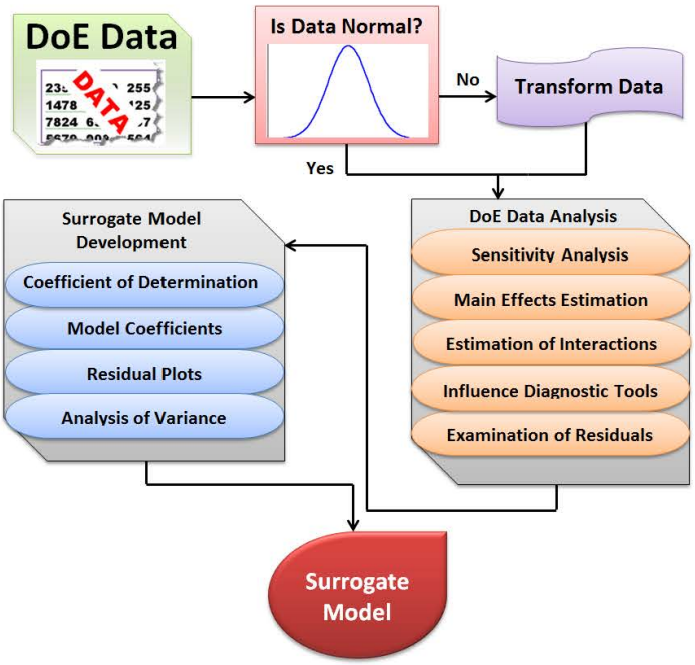

Figure 3.2. Methods used to analyse the DoE data and to develop a valid surrogate model.

The next step essentially consists of analysing the data generated from the design of experiment. There are two aspects to this analysis. The selection of the surrogate model will depend upon the sensitivity analysis, whereby it is determined which effects and interactions to include in the model, this will be discussed in the chapter six. Additionally, the main effects and interactions of the process are also determined at this stage. The other aspect of the analysis is to identify any data points that may unduly affect the rest of the data. This is known as influence diagnostics, and two main tools, Leverage and Cook's distance can be used.

The final step in the analysis is the development of the surrogate model. The model coefficients are determined. A number of surrogate models are iteratively processed until a model that fulfils the modelling assumptions is selected. The selection partly depends upon the examination of the residuals. It also depends upon an inspection of the coefficient of determination. The analysis of variance is a statistical procedure to check if the coefficients of the surrogate model have been appropriately selected, this will be discussed in chapter six. All the techniques just discussed above, combined help to develop a valid surrogate model.

3.2.1 Examination of Residuals

Residuals represent elements of unexplained variation in the fitted model. This is regarded as a form of error, and hence the same assumptions apply to them as they do to errors in general. For residuals it is assumed that they are normally and independently distributed with a mean of zero and with a variance at constant value.

For the surrogate model that will be developed the predicted values should be found to be higher and lower than the actual values, and should occur with equal probability. The residuals should be normal distributed. Hence, the level of the error should be independent of the:

- Factor settings used in making the prediction
- When the observation occurred in the study
- The size of the observation being predicted

If these assumptions are not met, the model cannot be accounted for as the residuals contain structure. The original model will need term(s) that represent the structure to give a better fitting model.

A number of graphical techniques can be used to demonstrate residual normality. Generally the frequency histogram can be used if the sample size is more than 50. The resulting graph should outline a bell shaped curved indicating a normal distribution.

Where the sample size is less than 50, a more sensitive technique is used, the normal probability plot. This is a plot of the cumulative probability of a point versus the residual value on normal probability paper. This will produce a straight line if the distribution is normal. A dot plot is overlaid and is the collection of points on the left y-axis. It shows the distribution of the residuals.

To use a normal probability plot:

- The residuals are sorted in ascending order.
- The cumulative probability of each residual is calculated, equation 3.1.
- The calculated p-values are plotted against the residual value using normal probability paper.

$$G_{i-th\ residual} = i/(N+1) \qquad \textbf{3.1}$$

Where:
G is the cumulative probability of a point
i is the order of the value
N is the number of residuals

If the points come from a normal distribution, they should form a straight line on the normal probability plot. Obviously the line may show some departure from a straight line which is acceptable. If the line makes an "S" shaped curve this would suggest a bimodal distribution, and if there are breaks in the middle of the distribution that will also indicate non-normality.

To test for time dependency, since the observations tend to be taken in the order of execution, a plot of the residuals against the case order or time order are made. Such a plot is referred to as a run sequence plot.

3.3 Steepest Ascent Method to Process Improvement

Once a suitable surrogate model has been established it is used to approximate the true response surface, which usually is a first order polynomial model. This model can be used to locate a new response region that will improve the process. The method of steepest ascent, or descent, can be used to locate the new response region. The method consists of the process of building a model from the design of experiments and the sequential search for the region of improved response. The design of experiments that are normally used are two level factorial designs, although fractional designs can also be used.

The steepest ascent (or descent) process consists of a number of steps, beginning with fitting a first order model using an orthogonal design. Since the response, the stress in the fibre is being minimised a path of steepest descent is computed. Otherwise the path of steepest ascent is computed if the response is to be maximised. The path is so computed so that there is a maximum decrease in the response. Experimental runs are then conducted along this path to find another path of steepest descent or ascent. The process will show the response improving. The process is stopped once there is a decline in the response. This decline in the response is due to the deterioration in the first order model.

3.3.1 Determining the Path of Steepest Descent

The signs and the magnitudes of the regression coefficients of the first order model will determine coordinates of the path of steepest descent. The movement of a factor x_i is proportional to the magnitude and in the opposite direction of its sign of its regression coefficient. This will give the path of steepest descent. If the same sign of the regression coefficient is used, this will give the path of steepest ascent. This path is perpendicular to the lines of constant response, as this is the most rapid movement (steepest descent) towards a small response value. Consider a first order regression model, equation 3.2.

$$\hat{y} = b_0 + b_1 x_1 + b_2 x_2 + \cdots + b_k x_k \qquad 3.2$$

The path of steepest descent produces a minimum estimated response with the spherical constraint:

$$\sum_{i=1}^{k} x_i^2 = r^2 \qquad 3.3$$

Points, $x_1, x_2, x_3, \ldots, x_k$, are being sought for which $\hat{y}$, is minimised from a fixed distance, r, from the centre of the design. All the x's will be at infinity by minimising the fitted response, $\hat{y}$, from the first order model, hence constrained optimisation is used. Lagrange multipliers are used to solve this optimisation problem. Partial derivatives with respect to x_j $(j = 1, 2, \ldots, k)$ are used for minimising:

$$L = b_0 + b_1 x_1 + b_2 x_2 + \cdots + b_k x_k - \omega \left(\sum_{i=1}^{k} x_i^2 - r^2 \right) \qquad \mathbf{3.4}$$

ω is the Lagrange multiplier. With respect to x_j the derivative is

$$\frac{\partial L}{\partial x_j} = b_j - 2\omega x_j \quad (j = 1, 2, \ldots, k) \qquad \mathbf{3.5}$$

The coordinate of x_j of the path of steepest descent is given by setting $\partial L / \partial x_j = 0$:

$$x_j = -\frac{1}{2\omega} b_j \qquad (j = 1, 2, \ldots, k) \qquad \mathbf{3.6}$$

The value $1/2\omega$ is positive for the steepest ascent and is negative for the steepest descent.

3.4 Review of DoE and Response Surface Methodology in Welding

A number of researchers have investigated the use of design of experiments and response surface methodology for the welding process. The work involves correlating the welding input parameters with the desired welding output parameters to improve the welding process. To this end generally two research areas have been developed. This

includes empirical methods based on welding experiments, and mathematical modelling based on the statistical design of experiments and response surface methodology.

In order to predict the penetration, width, reinforcement height and width to penetration ratio of an arc welding process, fractional factorials have been used to model this (Raveendra and Parmar 1987). The work was done using thick low carbon structural steel plate with arc welding. The input parameters that were selected were arc voltage, welding current, welding speed, gun angle and nozzle-to-plate distance. A number of models were developed that were used to predict either the bead geometry or the parameters needed to obtain the desired bead geometry.

Others have developed linear regression equations using data from a design of experiments (Yang et al., 1993), to predict the melting rates, total fusion area, penetration, deposit area, bead height and bead width. This was for a submerged arc welding (SAW) process using ASTM A36 steel plate. The input parameters that were used were the electrode extensions range, welding voltage, welding current, welding speed and electrode diameter. Their results showed that the linear regression equations were useful for computing the various features of the submerged arc welding process.

The influence of electron beam power, welding velocity, distance from the main surface of the magnetic lens to the focus point and the distance between the magnetic lens and the sample surface on the welding depth and width electron bean welding, have been investigated (Koleva 2001) in electron bean welding. A design of experiment was done using austenitic steel to establish the depth and width that would lead to the optimal welding conditions using a response surface.

Based on previous work (Gunaraj and Murugan 1999) a model was developed to relate the weld bead volume to SAW parameters (Gunaraj and Murugan 2000a). It was shown as welding voltage increases the bead width and dilution increase and the penetration is reduced. With further work (Gunaraj and Murugan 2000b) a sensitivity analysis was performed to predict the effect of the other bead parameters on the total volume. Using response surface methodology, the total volume of the weld bead was optimised (minimised). This work was developed further (Gunaraj and Murugan 2002) to

investigate the effect of SAW parameters on characteristics of the heat affected zone of the weld.

Using response surface methodology the relationship between the process parameters of beam power, welding speed and beam incidence angle and the weld bead parameters of penetration, bead width and area of penetration were for laser welding were investigated (Manonmani et al., 2005). The surrogate model of the response surface was experimentally validated and was found to be in good agreement with the experimental work.

To determine the critical process variables of gas metal arc welding, design of experiments was implemented using a full factorial experiment at two levels with three process variables (İç et al., 2012). Using amour steel for the experiment the process variables that were investigated were the welding groove angle, the welding groove geometry and the welded joint (and compression loading). The output parameters that were used were yield point, tension or compression strength and the modulus of elasticity.

Using a CWNd:YAG laser to weld Austenitic stainless steel (AISI 304), the effects on the depth of penetration of the weld and the weld bead width were studied (2009). A design of experiment using three levels with a Box-Behnken design used laser power, welding speed and shielding gas flow rate as the process parameters. Using an artificial neural network and multiple regression analysis a model was derived for the prediction of the penetration of the weld and the weld bead width.

Laser butt welding of Ti 6Al using a CO2 laser was investigated (Khorram et al., 2011). Using a design of experiments to establish a response surface to optimise the bead geometry, welded zone width, heat affected zone width, welded zone area, heat affected zone area and penetration depth. The input welding parameters were the laser power, welding speed and focal point position. The multi-response optimisations were used to optimise the welding process. The results were validated and showed that the developed model was accurate with a low percentage of error.

3.5 Conclusion

This chapter has discussed the third objective of this work. The chapter reviewed the different methodologies that will be used to develop a surrogate model. The chapter also reviewed the design of experiments and response surface method in relation to welding.

There are a number of key factors that affect the thermomechanical generation of stress in the optical fibre. In order to asses these key factors in an efficient and resourceful manner design of experiment methodology will be used. This has been reviewed in this chapter, and also the assumptions that need to be made to use this methodology. All the techniques that are used in the OPISA methodology require the data to be a normally distributed. Hence, the initial analysis is to check for normality. If the data is from a non-normal distribution it will require transformation using either a Box-Cox or Johnson transformation, both techniques are standard.

After ascertaining the data to be normal using the Anderson-Darling test. A number of techniques are used to analyse the data to determine the main effects and the interactions. Additionally, the data is checked to ensure that there are no outliers that may unduly affect the data, and that the modelling assumptions are fulfilled.

The surrogate model is developed by establishing the coefficients of the model. A number of models are produced. The model that is selected is one that fulfils the assumptions of the modelling process and had a good coefficient of determination. Once an empirical surrogate model has been developed, to improve the process, the path of steepest descent methodology is used, which is also been discussed here.

There was also a review of the DoE and response surface methodology in welding research. Welding processes have a large number of interrelated parameters which range from the setup of the welding equipment to the material properties. With such a complex physical process as welding, research has shown DoE and response surface methodology has given insights to optimise the various welding processes.

Chapter 4

Thermomechanical Modelling of the Laser Welding Process

This chapter covers the fourth objective, the development of a thermomechanical model that captures the welding of the sleeve and ferrule. The chapter also covers the fifth object, the understanding of the evolution of the temperature fields, the von Mises stress and displacements of the optical fibre.

Accurate prediction of the weld induced stresses and the variation of temperature with time, the heating and cooling phases within the weld spot requires an understanding of heat transfer of the weld pool. Hence, the objective of this part of the study is to understand heat transfer during the formation of the weld. In particular, the work seeks to identify the temperature distribution and the thermal cycles. This knowledge is necessary to understand the development of the residual stresses and the extent of the distortions in the weld piece.

In this chapter the discussion will initially focus on the setup of the optoelectronic package and the welding process involved in attaching a steel sleeve to a steel ferrule. The fibre capsule and the types of bonding and their merits in attaching to the fibre capsule are also examined. The different types of welds are investigated with their relationship to the laser setup and welding of the butterfly package.

The chapter will culminate in the building of a number of high fidelity models, which are based on the Oclaro optoelectronic package. These models are used to investigate the heating and cooling of the weld spot and the stresses produced by simulating welding of the sleeve and ferrule.

4.1 Introduction

The optical fibre within the fibre capsule requires precise alignment with the optical source within the butterfly package. Sub-micrometre alignment accuracy is critical for efficient optical performance. Optical alignment requirements are generally more precise than those required by electronic packages (Vernooy 2004). To achieve such accuracy and then to maintain it requires appropriate joining techniques. Depending on the package configuration, either butterfly package or dual-in-line package, three primary joining techniques are used, epoxies adhesives, soldering or laser welding, (Jang, 1996). In this work the optoelectronic package configuration that is peculiar to Oclaro was studied.

Using epoxies within confined spaces is difficulty, and requires specialised equipment. Epoxies require curing time and also produce outgas or curing residues, this is a disadvantage as it can affect the optical path and the piece will not be reworkable.

Soldering does allow for post bond adjustments due to bonding misalignments. Compared to soldering and adhesives, laser welding allows higher production rates and easier automation. Additionally, the use of laser welding has a number of advantages–

- High weld strength to weld size ratio, resulting in a join that is comparable to the parent material (Kazemi and Goldak, 2009). This results in a deep and narrow weld shape.
- Low heat input into the weld, resulting in reduced distortion of the work piece (Fassani and Trevisan, 1999).
- Ability to weld heat sensitive components.
- The heat affected zone (HAZ) is characteristically smaller and narrower than using conventional welding (Zhou and Tsai, 2008).
- Accurate welding, and amenable to automation (Sherry et al., 1996).

As with all welding techniques, laser welding does have some disadvantages:

- The main disadvantage of laser welding is the misalignment caused by stress due to severe thermal gradients as a result of the intense energy input from the laser. This can cause misalignment in excess of ten micrometres. The piece can be reworked to correct this (Hayashi and Tsunetsugu, 1996).

- Due to the lasers focused spot size it requires close fitting joints, as ability to bridge a gap is limited.
- Focus shifts in the focusing optics can occur due to the high power outputs.
- The fibre-optic coupling and other optical components are highly sensitive to dust particles.
- High operating and equipment costs.

4.2 The Oclaro Welding Setup

It is important to achieve efficient coupling between the optical fibre and the butterfly package laser source. Alignment between the fibre and the laser source is one of the most important and critical factors that affects the efficiency of the optoelectronic package. Of the two package configurations, the use of the butterfly package allows high power output, speed and reliability as compared to the dual-in-line package, (Tsai et al., 2011).

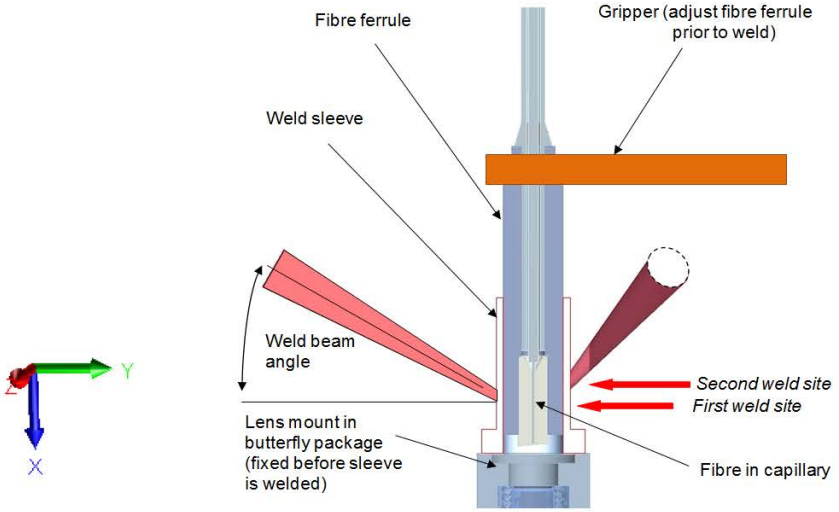

Figure 4.1. The setup of the Oclaro fibre capsule and the butterfly package prepared for laser micro welding.

For the Oclaro fibre capsule preparation for welding involves manually placing the fibre capsule in alignment with the lens mount which is part of the butterfly package. This initial process of ensuring the alignment of the fibre optic with the laser source can take a technician up to several minutes to achieve. Once this has been achieved the fibre

capsule is secured into position using a gripper, figure 4.1. This process takes place in an assembly cabinet as shown in figure 4.2; the inset shows the internals of the assembly cabinet. The operator station, figure 4.2, is normally manned by an individual technician. The complete process of pre-welding alignment and post-welding alignment checking and readjusting takes approximately ten minutes per butterfly package.

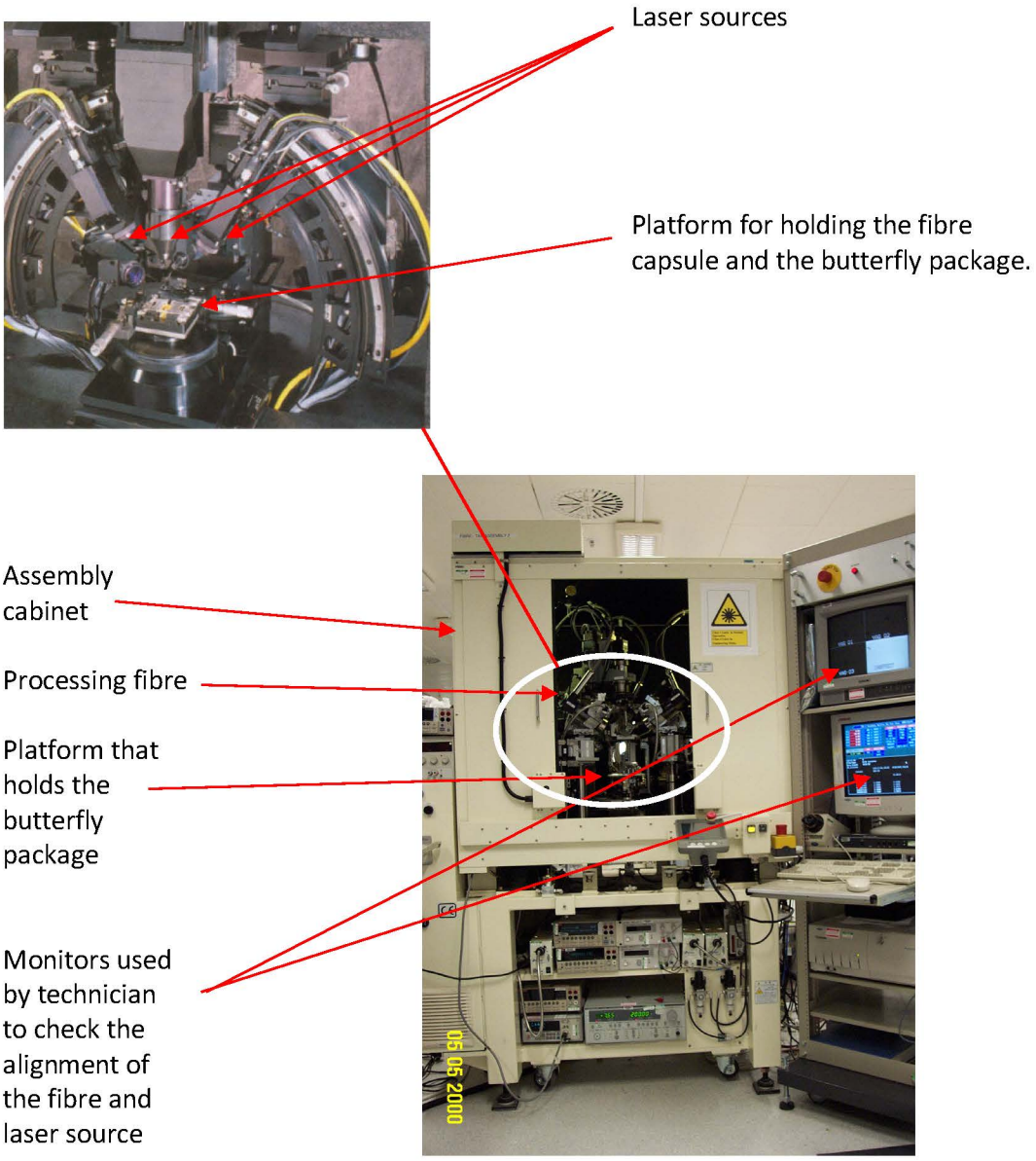

Figure 4.2. Laser welding station (picture courtesy of Oclaro).

The process of micro laser spot welding is done using a Nd:YAG (neodymium-doped yttrium aluminium garnet; $Nd:Y_3A_{l5}O_{12}$) laser source. The Nd:YAG laser has power in the range of 0.3-3 kW commercially, and in the lab up to 12 kW.

The Nd:YAG laser is used to weld the steel sleeve to the steel ferrule using a series of six weld spots. The firing of multi-beam lasers, see figure 4.3, is used to produce the weld spots, which form within a few milliseconds.

The multi-beams according to the manufacturers of the laser systems are of equal energy (Luminomics n.d., Unitek Miyachi n.d.). However, it has been found that this is not necessarily the case, as there is some energy variation in the beams (Fraser 2008).

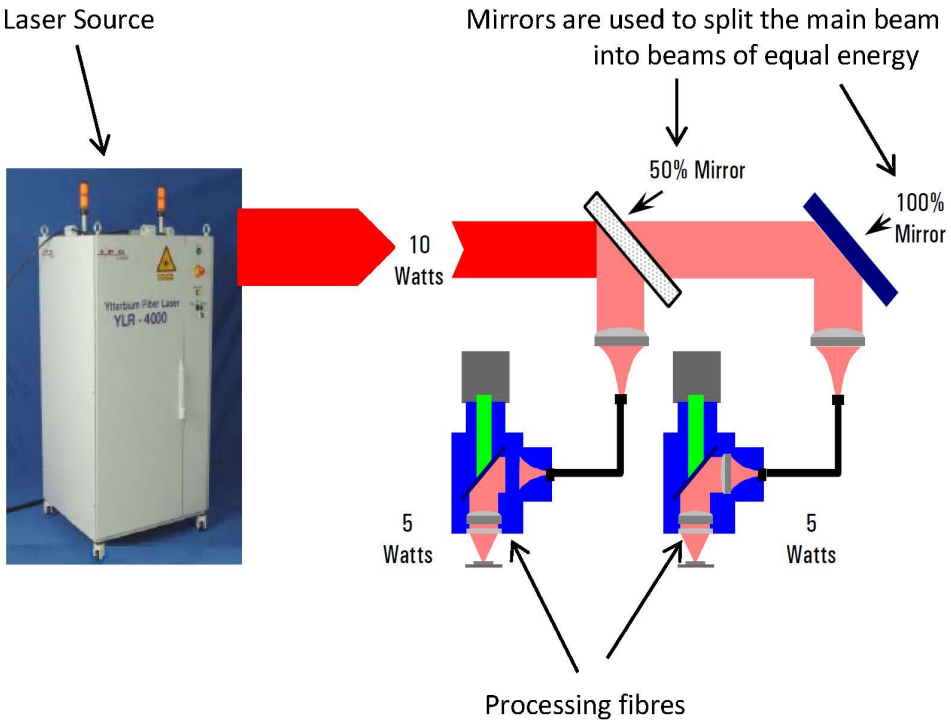

Figure 4.3. The Nd:YAG Laser beam is split by a beam processer. (Adapted from Luminomics n.d)

One of the main disadvantages of using laser welding is the severe thermal gradients due to the intense energy input which can cause stress in the components of the package. The effects of the thermal stress can results in misalignment of the fibre and the laser module. A movement of a few micrometres to in excess of 10μm have been observed (Hayashi et al., 1996). These post-welding movements can normally be compensated to ensure maximal efficiency of the fibre-laser alignment.

4.3 Oclaro Laser Welding Process

4.3.1 Laser Setup

The welding system used by Oclaro consists of either a Luminomics (Luminomics n.d.) or a Unitek Miyachi (Unitek Miyachi n.d.) pulsed Nd:YAG laser which has a wavelength of 1064nm. The system uses a variable beam attenuator to split the single beam into three laser beams of equal power, figure 4.3.

4.3.2 Joint Design

There are a number of joint geometries possible with laser welding, as laser welding is a non-contact process that is able to weld into areas with limited access. The most common types of weld geometries are shown in figure 4.4.

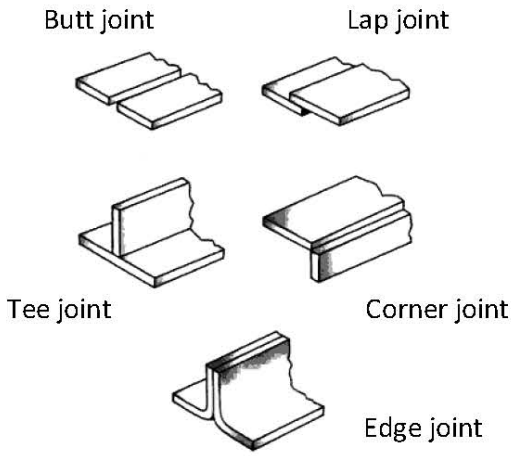

Figure 4.4. Joint geometries available with laser welding, other types of geometries are variations of these (adapted from Lancaster 1986).

Attaching the sleeve to the ferrule, stake welds are used on lap joints. The sleeve is thinner than the ferrule, which is a key requirement. Another requirement is that the joint interfaces are a close fit, as laser spot welding is an autogenous process; no filler material is added during welding (Pang et al., 2008). Hence, if the interfaces are not close enough the weld will not bridge the gap between the interfaces.

4.3.3 Parts Geometry

The parts geometry and materials can be seen in figure 4.5. The core of the optical fibre consists of glass. The optical fibre is covered with an ultraviolet coat and the fibre is contained in a protective Hytrel tube. The tube is held in place inside the ferrule using an epoxy adhesive, see figure 4.5.

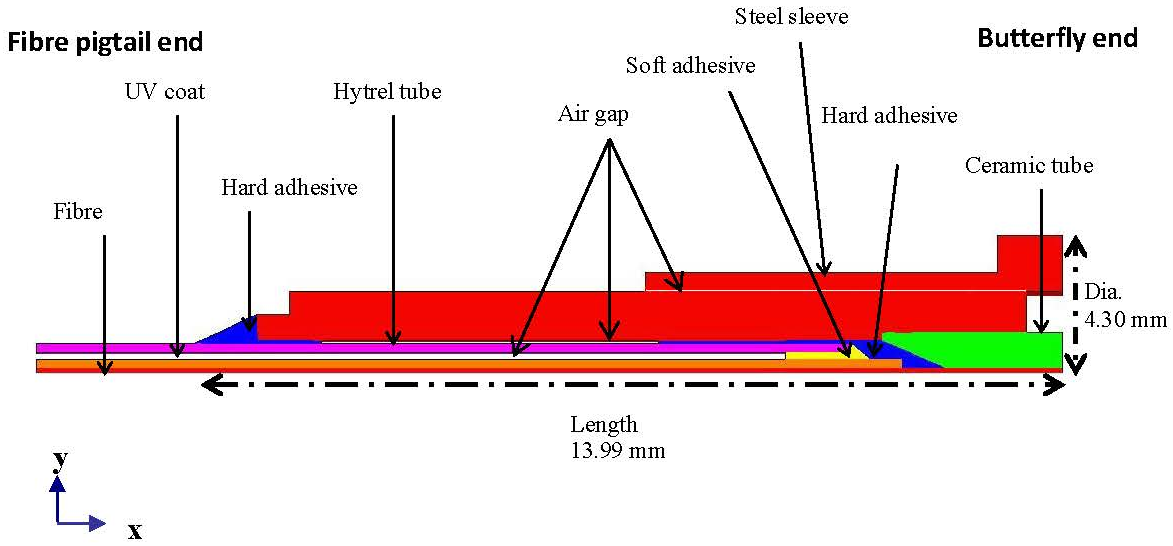

Figure 4.5. Geometry and the materials of the fibre capsule.

At the butterfly end, because of its location this adhesive has been found not to set fully, and appears soft in sections of the package, figure 4.6. At the opposite end the adhesive has fully set and is referred to as the "hard adhesive". At the location of the "soft adhesive" the plastic (Hytrel) tube has been stripped. Before the fibre enters the zirconia ceramic tube the fibre has been stripped of the UV coat. The ceramic tube is held in place using epoxy adhesive, which in sections appears to have fully set, and is referred to as the "hard adhesive". The steel ferrule is then inserted into a steel sleeve. This is a sliding fit, and the two components are then welded together, figure 4.6 shows this geometry.

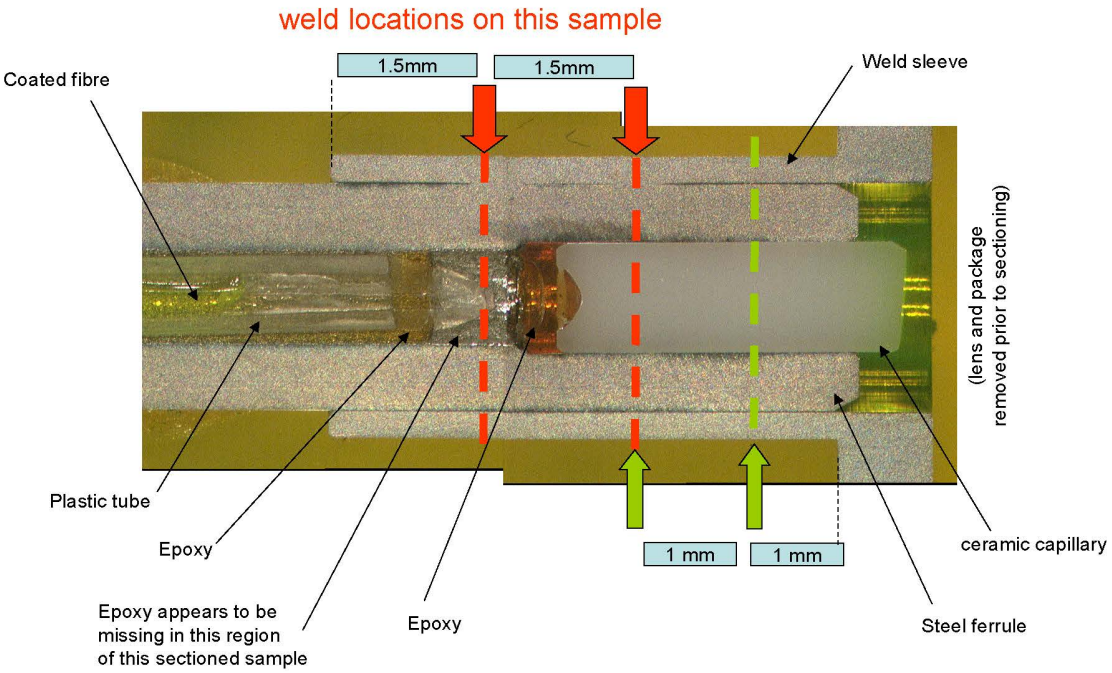

Figure 4.6. Longitudinal section of welded fibre tail, this section does not intersect the fibre. (Picture courtesy of Oclaro).

4.3.4 The Weld Spot

In figure 4.7, a transverse section of a laser spot weld from the fibre capsule was chemically etched to highlight the metallurgical features. The estimated volume of the frozen melt pool is approximately 0.04 mm^3. Analytical calculations show there must have been a heat input greater than or at least equal to 0.4 Joules. The engineering team of Oclaro measured the uncalibrated optical energy to be 2.7 Joules. The laser pulse was of a duration of less than seven milliseconds. The course grained region, CGR, figure 4.7, occurs in the high temperature heat affected zone, HAZ. The fine grained region, FGR, occurs in the partly melted zone. The partially transformed region, PTR, occurs in the low temperature heat affected zone.

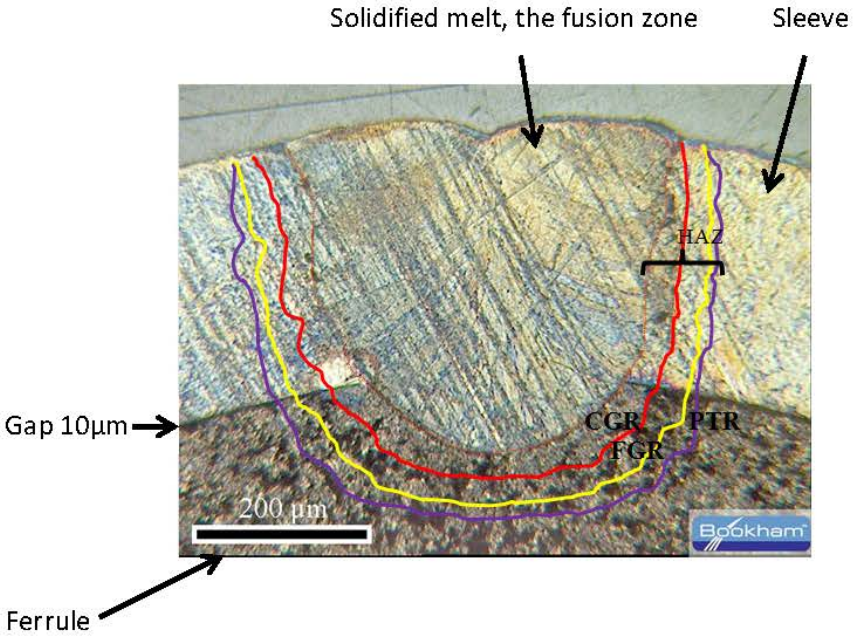

Figure 4.7. Transverse section of a laser spot weld, chemically etched to highlight metallurgical features. (Picture courtesy of Oclaro).

4.4 Modelling

The modelling work was done using FEMGV (Femsys, n.d.) which was used as a pre-processor and post processor. The finite element processor was PHYSICA (Physica, n.d.), whose code has been developed at the University of Greenwich and is customisable.

It can be seen from figure 4.8 the fibre capsule is symmetric around the fibre. At every 120 degrees there is a plane of symmetry giving three sections. Each section consists of the same geometry, hence only one third needs to be modelled.

To create the CAD model, an initial symmetric model was created that was of a two dimensional construct. This was rotated by 18 degrees to give the diameter of the weld spot. The 18 degree rotation is equivalent to a half millimetre rotation. The model was rotated a further 102 degrees, giving a total rotation of 120 degrees. This further rotation gave a one third model of the work piece, symmetric around the optical fibre. The model includes two weld spots, see figure 4.8. The model has a mesh density

comprising of 241,060 elements and 243,675 nodes. The area of the weld spot was finely meshed, see figure 4.9.

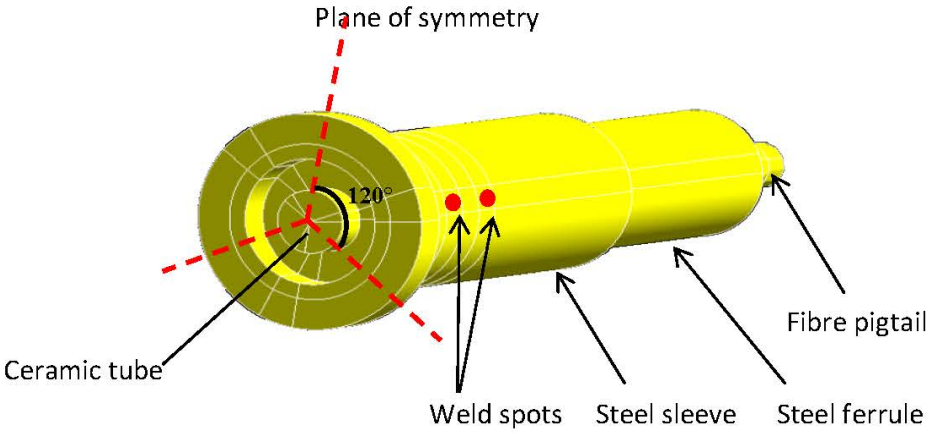

Figure 4.8. Three dimensional model of the fibre capsule showing the planes of symmetry at every 120 degrees.

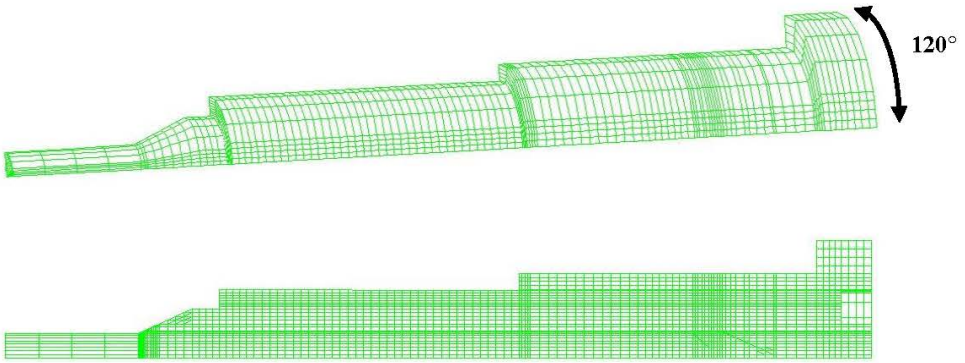

Figure 4.9. The mesh density of the model.

4.5 Modelling Assumptions & Material Properties

The increase in computing power and the advancement of FEA software has resulted in the feasibility of three-dimensional simulations that can capture most of the physics, which usually require a large amount of data input. However, most of this data is not necessarily readily available, such as mechanical temperature-dependent and thermophysical properties and any changes due to phase transformation. Even using

experiments to gain such data is not easy to obtain. For this work such data was not available.

Detailed modelling of the weld pool physics is complex and includes buoyancy, surface tension driven convection, solid-liquid and liquid-vapour phase change, laser-vapour plume interactions and pool surface deflections (Russo et al., 1990; Kanouff and Greif, 1992). Detailed modelling of the weld pool physics is not necessary as only the thermal response of the part near the weld pool was of interest. Work done in the 1990's researchers noted that significant computational resources are necessary to model even simple weld pool geometries where stationary or continuous laser beams are simulated (Russo et al., 1990 and Radaj, 1992). Currently even with the increase in computational power others have noted that the physics of the weld pool can be neglected when the aim of the simulation is to investigate residual stresses due to welding (Mobarhan et al., 2000, Mueller and Valk 2000, Zhou & Tsai, 2008, Kazemi & Goldak, 2009, Pang et al., 2008, Song et al., 2009). For this work, the physics of the weld pool are not of interest and hence have not been modelled.

Table 4.1. The material properties for 304L stainless steel, and the laser settings used in the model.

Property	Value	Units
Density	8000	kgm^{-3}
Absorption coefficient	0.27	-
Solidus temperature	1693	K
Liquidus temperature	1727	K
Melting Point	1698	K
Heat of vaporisation	6330	$kJkg^{-1}K^{-1}$
Ambient temperature	298	K

With this in mind a three-dimensional model is developed. The material properties that were used are listed in table 4.1 and table 4.2, below.

In modelling the finite element model it has been assumed that –

- The laser is of equal power at each of the weld spots.
- The welds spot form simultaneously.

- The heat source is a Gaussian heat source.
- The air gap between the steel sleeve and ferrule is of 10 μm.
- All the components sit squarely in the air gaps.
- The weld spots bridge the gap between the ferrule and sleeve.

Table 4.2. The material properties used for the thermal and stress analysis

	CTE ppm/K	Thermal Conductivity W/m.K	Specific heat J/g/K	Density g/cc	Young's modulus GPa	Poisson's ratio
304L Stainless steel	17.5	16.3 (100degC) 21.4 (500degC)	0.5	8	200	0.248
Capillary (zirconia)	10	2.1	0.4	6	205	0.3
Fibre (glass)	0.49	1.6	0.7	2.1	73	0.17
Buffer coat on fibre (polymer)	120	0.2	1.5	1.1	1	0.5
Adhesive 1 (tube to fibre coat)	110	0.2	1.4	1.2	1.6	0.35
Adhesive 2 (fibre to capillary)	50	0.35	1.4	1.2	2.3	0.35
Hytrel Tube	135	0.25	1.0	2.2	0.55	0.45

The values of the CTE, Young's Modulus, density, specific heat and thermal conductivity, are considered temperature dependent. Because of the limited availability of the physical data, in the current simulations only properties at room temperature were taken into consideration. Once the model had been developed a number of experiments were conducted to ensure that the model was mesh independent (see figure 4.10). A number of experiments were also conducted to ensure the model was time step independent.

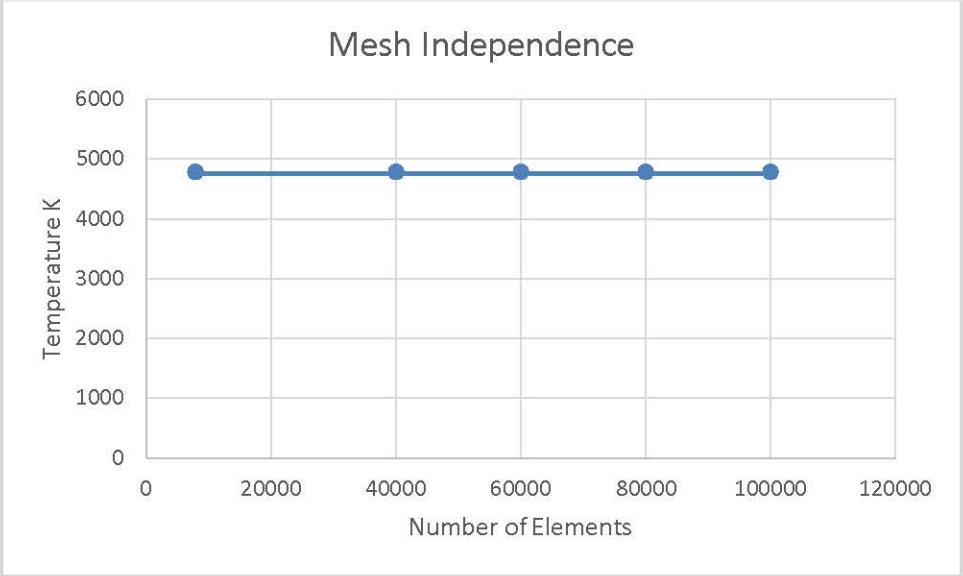

Figure 4.10. Graph showing mesh independence.

4.6 Boundary Conditions

For the heat simulation, the initial condition for the weld model is –

$$T = T_{\infty} \text{ at } t = 0 \qquad 4.1$$

The surface temperature and room temperature are denoted T and T_{∞} respectively and t is the time. So that

$$k\frac{\partial T}{\partial x}l_x + k\frac{\partial T}{\partial y}l_y + k\frac{\partial T}{\partial z}l_z - \dot{q} + h\left(T - T_{\infty}\right) = 0 \qquad 4.2$$

Where h denotes surface heat loss coefficient, lx, ly and lz the direction cosines to the boundary surface.

Different types of heat sources have been suggested (Goldak 1984, Radj 1992). Three main methods are used. One method is to apply a heat source whose size and heat density are then adjusted to retrieve a fusion zone with good agreement with a real weld. A second method is to use a surface distribution to simulate the laser. A very common

distribution used is the Gaussian distribution. The last method is to use a double ellipsoid heat source, which was first suggested by Goldak (1984).

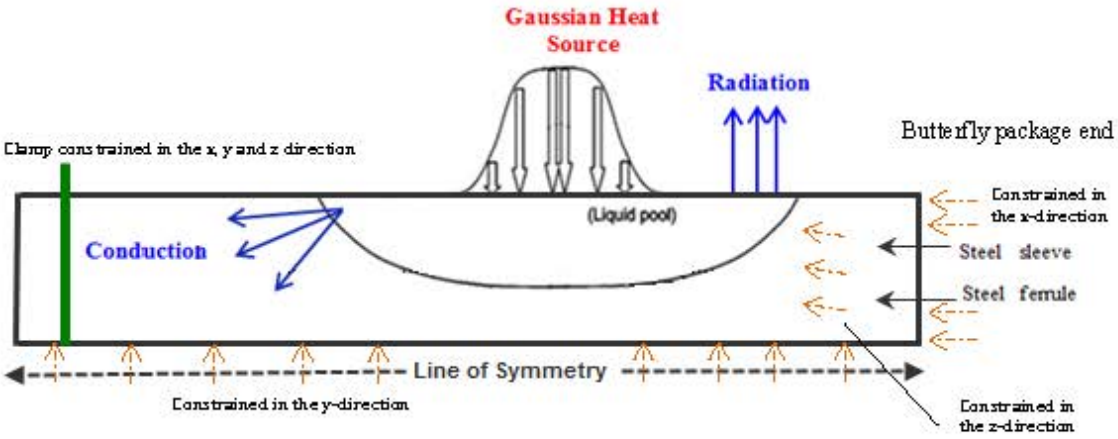

Figure 4.11. Diagrammatic representation of the boundary conditions used for modelling the weld spot (adapted from Zhang et al., 2003).

This method combines the first two types since it includes a surface distribution as well as a heat source within the material. For the simulations in this work only the second method, that of applying a heat source as a surface distribution to the material was used.

A three-dimensional Cartesian coordinate system is used in the calculation. Figure 4.11 is a diagramatic representation showing the boundary conditions that were used.

The heat flux at the top surface of the steel sleeve is given in equation 4.3. The first term of this equation on the right hand side is the heat input from the laser, defined by a Gaussian heat distribution.

$$k\frac{\partial T}{\partial z}\Big|_{top} = \frac{fP\eta}{r_p^2}e^{\left(-\frac{f(x^2+y^2)}{r_p^2}\right)} - s\varepsilon\left(T^4 - T_\infty^4\right) - h_c\left(T - T_\infty\right) \qquad \textbf{4.3}$$

Where, f is the power distribution factor, P is the total laser power, η is the absorption coefficient, r_p is the heat distribution parameter, s is the Stefan-Boltzmann constant, h_c is the heat transfer coefficient, and the material emissivity is given by ε.

The first term on the right hand side of equation 4.3 represents the heat input. The remaining terms represent the heat loss. The heat loss by radiation and convection are given in equation 4.4 and equation 4.5 respectively. At all other surfaces, the temperature is set at the room temperature, T_∞.

$$s\varepsilon\left(T^4 - T_\infty^4\right) \qquad \textbf{4.4}$$

$$h_c\left(T - T_\infty\right) \qquad \textbf{4.5}$$

4.6.1 The Mechanical Boundary Conditions

The mechanical boundary conditions need to ensure that the model is constrained in such a manner as to prevent rigid body motion.

The constraints on the model are based on the welding configuration of the geometry as shown in figure 4.1. The steel sleeve rests on the butterfly package, inside the steel ferrule the ceramic capillary and the optical fibre rest vertically on a lens mount, which is located inside the butterfly package. The steel sleeve, the ceramic capillary and the optical fibre hence cannot move in the *x* direction, see figure 4.1. For the FE model this is shown in figure 4.12.

Once the alignment of the optical fibre and the laser source has been achieved, the fibre capsule is held in place by a clamp, as shown in figure 4.1. For the FE model the fibre capsule at the location of the clamp is constrained in the *x*, *y* and *z* direction, see figure 4.11(b). Additionally, in the FE model the surface of the plane was constrained in the *z* direction see figure 4.11(b). The lower plane of the model was constrained in the *y* direction see figure 4.11(b).

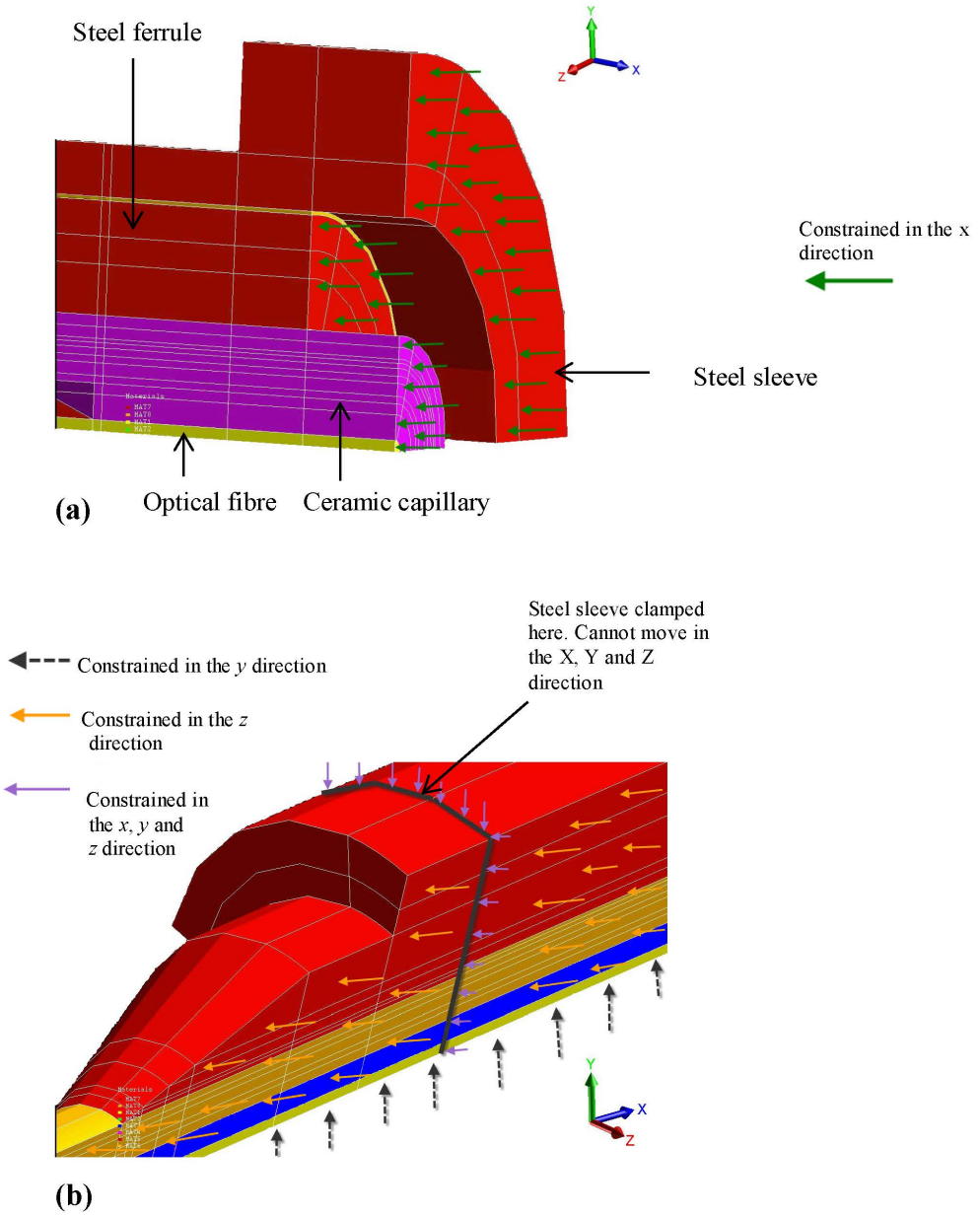

Figure 4.12. (a) and (b) Mechanical boundary conditions.

4.7 Simulation Results

4.7.1 Temperature Profiles

A graph of the temperature of the weld pool with increasing depth is shown below in the figure 4.13. The inset in the figure shows a line piercing the weld spot at the centre starting from the surface. This line indicates the location from where the temperatures

where noted. Apart from time $t = 0$ all the other time periods show varying levels of part of a Gaussian heat distribution with its typical bell shape, figure 4.13(b).

The graph in figure 4.13(a) is for the first four milliseconds, the period in which the laser is pushing heat into the work piece.

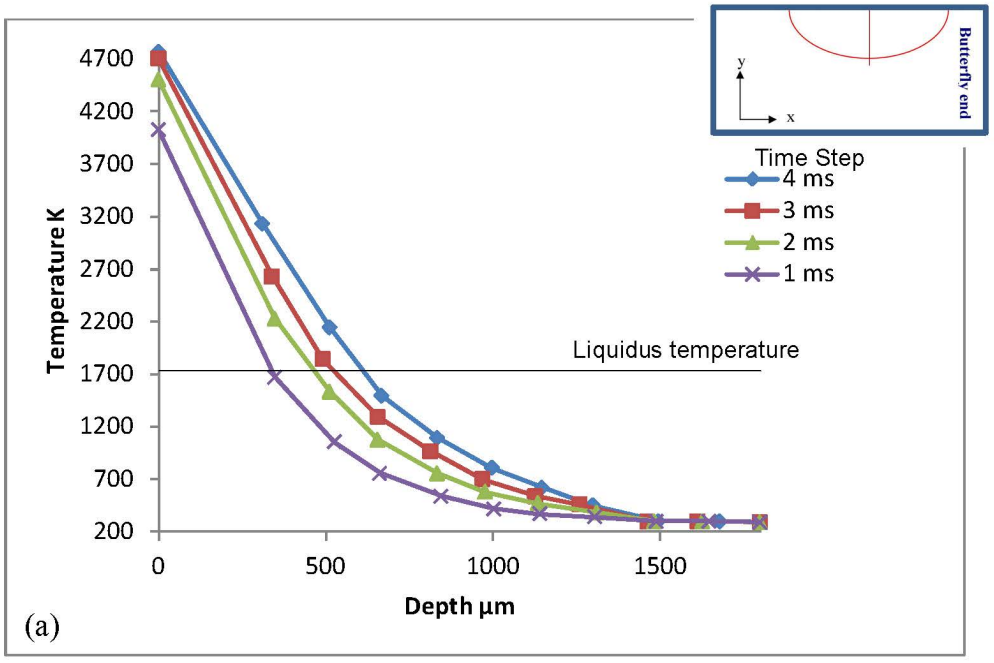

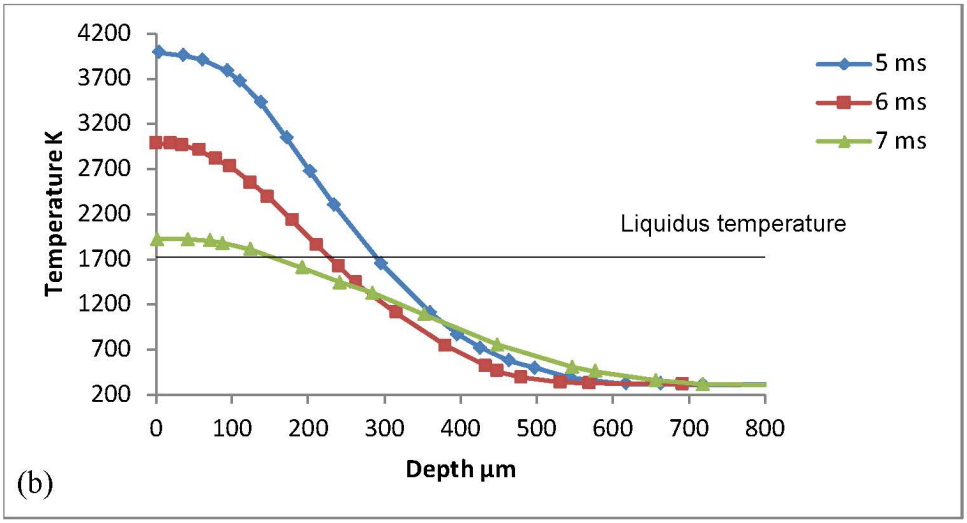

Figure 4.13. (a) and (b) Graphs showing the temperature with increasing depth of the weld spot.

During each time period the maximum temperature is observed at the surface of the weld spot, specifically in the centre. The heat penetration causes a change in the temperature to a maximum depth of 1472 μm into the work piece. From the surface of the spot where the temperature is maximal, going into the depth of the weld spot there is a steep temperature gradient as indicated by the curves of the graph which have a very steep slope. There is an exponential decrease in the temperature from the surface up to 1000 μm into the depth of the work piece. Beyond 1000 μm the temperature decrease slows down.

The liquidus temperature is marked on the graph. The deepest penetration of the liquefied metal can be found during the fourth millisecond of the pulse, at a depth of 640 μm. For each time step the depth of penetration of the molten metal increases during the first four milliseconds. The metal melts during the first four milliseconds at a rate of 175 mms^{-1}. Once the laser stops pulsing heat is lost as it is conducted into the bulk of the weld piece, and also due to radiation, which hampers the penetration of the heat into the depth.

The graph, figure 4.13(b), shows the cooling curves for the weld spot after the first four milliseconds. As the time period increases the slope of the curves decrease, and the typical bell shape of the Gaussian distribution becomes less pronounced. This is to be expected since with increasing time the heat content of the system decreases. However, there is still molten steel at the surface, even though solidification has started.

At the centre of the weld spot on the surface the temperature will always be the highest since this is where the laser beam's spot is focused to deliver the power. It is from here that temperature then radiates outwards and into the depth of the work piece. These graphs also give an indication of the maximum depth of the weld spot.

The graphs in figure 4.14 show the surface temperature across the weld spot, as indicated in the inset. The distance starts from the butterfly end. The graph in figure 4.14 (a) shows the temperature distributions across the surface of the weld spot during the first four milliseconds the laser pulses. The curves show a similarity to a Gaussian distribution.

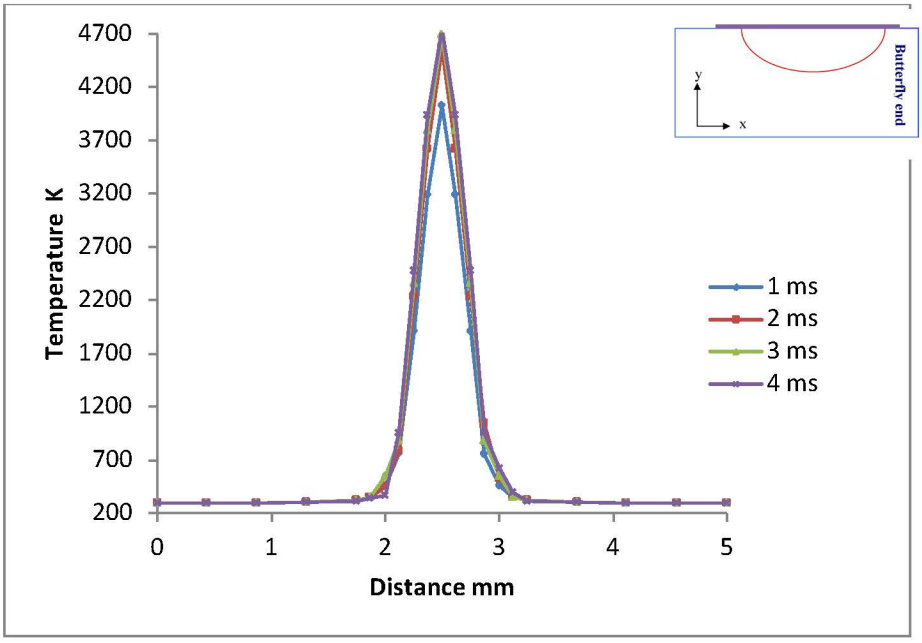

(a)

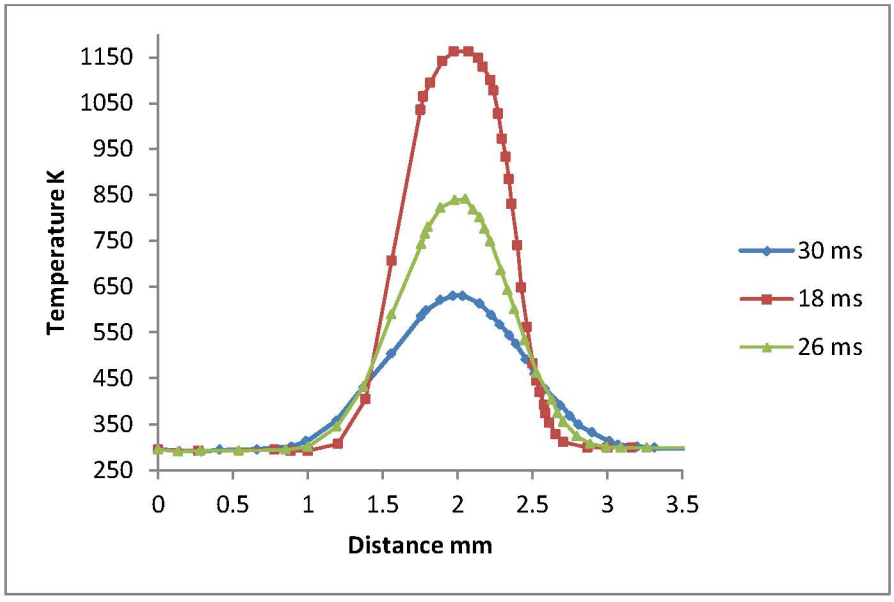

(b)

Figure 4.14. (a) and (b) Graphs showing the surface temperature across the weld spot, the location is shown in the inset.

The curves show the development of the temperature field that includes mainly heat input. Here the heat output is in the form of vaporisation of the steel sleeve (Ion 2005, He et al., 2006).

The graph figure 4.14 (b) shows the temperature for three later time periods during the cooling phase. Once the laser pulse has elapsed, the typical Gaussian distribution is observed. Here, there is only heat loss, and naturally as time progresses the slope of the curves decreases and flattens out the curves. This indicates the onset of solidification.

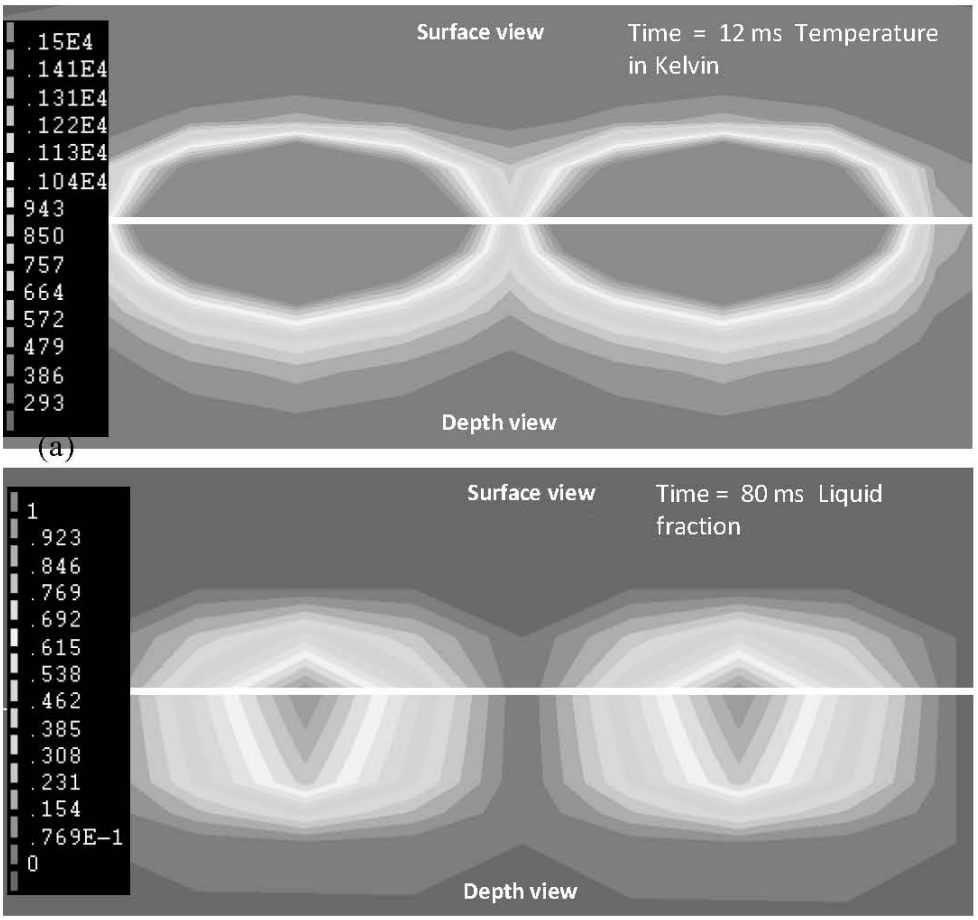

Figure 4.15. The development of the weld spot from two different views. (a) Shows the temperature in Kelvins. (b) Shows the liquid fraction.

The images in figure 4.15 are taken from the simulation. For each image there are two views shown simultaneously. The top part of each image shows the surface view and the lower part is a view of the plane showing the depth of the weld spot.

Figure 4.15(a) show the temperature at 12 milliseconds. The laser stopped firing eight milliseconds earlier and heat is being lost at the surface of the weld spot, and at the

sides of the weld spot the heat is conducted into the bulk of the sleeve. It can be seen from the figure that at the surface the heat has spread out and partially marks out the surface of the weld spot, as the weld spot has started to solidified. The lower part of this figure shows the temperature in the depth of the steel sleeve and ferrule. This region has also started to solidify.

Figure 4.15(b) shows the liquid fraction at 80 milliseconds. During this time period the steel has mostly solidified to form a solid weld nugget. The surface image shows the extent to which heat has affected the steel sleeve and ferrule. The same is also true of the depth view.

Figure 4.16 shows the graphs of the temperature measurement at various time steps taken from the centre of the weld spot, which is two millimetres from the butterfly end. The graphs show the maximum temperature achieved in the middle of the weld spot on the surface, the location is shown in the inset.

Figure 4.16 (a) shows a number of interesting features associated with the heat input from the laser whilst it is firing. It also shows the heating and cooling of the weld spot at its centre on the surface. During the first millisecond there is a rapid increase in temperature as indicated by the steep slope of the curve. During the next three milliseconds the temperature of the system increases but not as rapidly as the first millisecond. After the fourth millisecond rapid cooling starts.

During the first millisecond the temperature increase of the steel sleeve is at a rate of $373kKs^{-1}$. The heat content of the system has increased very rapidly. During this period some of the steel vaporises from the surface (Ion 2005, He et al., 2006). The vaporisation causes the temperature rate to decrease to $47.5kKs^{-1}$ during the second millisecond. As more of the heat begins to melt the steel the temperature rate falls further to $20kKs^{-1}$ during the third millisecond.

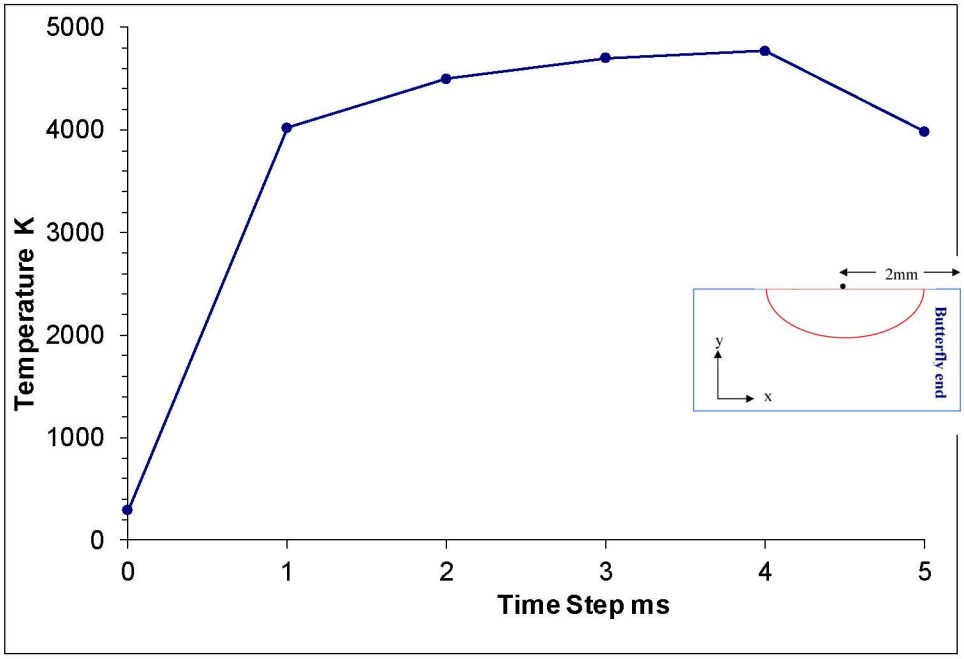

(a)

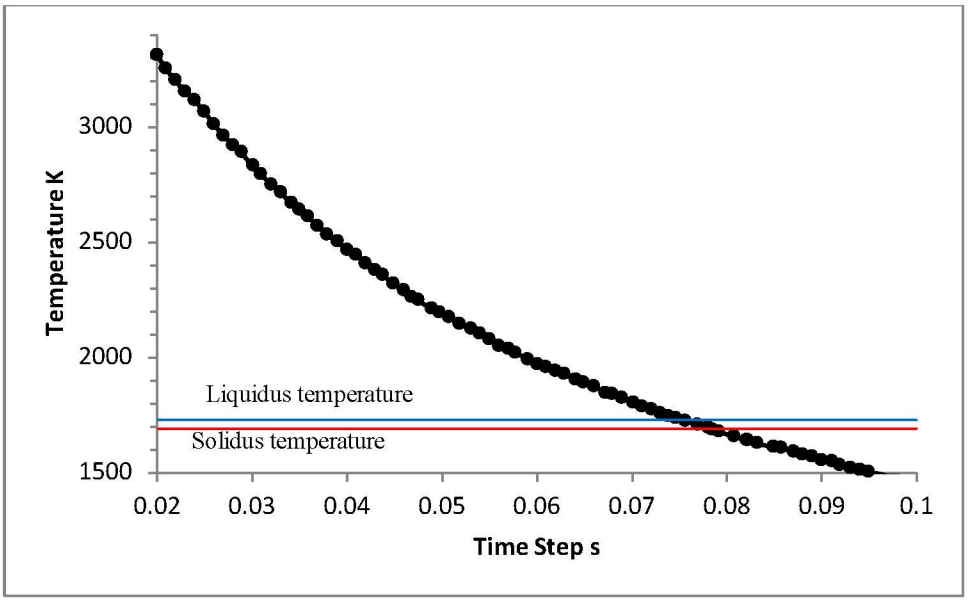

(b)

Figure 4.16. At various time steps, (a) the heating and (b) the cooling curve for the weld spot, at its centre on the surface.

From one to two milliseconds there is decrease in the heat rate, this can be attributed to the cooling mechanisms coming into play, but not to full capacity, as the temperature is still peaking. At four milliseconds the temperature peaks to a maximum of 4770 K, and

thereafter there is a rapid decrease in temperature. This is when the laser stops pulsing and heat is now being lost by conduction and radiation.

Beyond four milliseconds, when the laser has stopped pulsing, there is rapid and exponential cooling, as shown in figure 4.16(b). This can be accounted by the continuing effects of heat loss due to conduction and radiation. The trend line gives an indication of the rate of heat loss from the work piece, given by –

$$temperature = 3739.6e^{-10.03*timeStep} \qquad 4.6$$

The $R^2 = 0.9806$, and gives a good indication of how closely the trend line follows the original curve. The closer R^2 is to one the better the correlation between the trend line and the original curve.

4.7.2 Liquid Fraction

The formation of the liquid fraction is dependent on the local temperature, which initiates the melting of the steel and the formation of the liquefaction of the steel. Because of the high power of the laser the melting and subsequent liquefaction process traverses into the depth of the weld spot.

It is assumed that the liquid fraction L_f varies linearly with temperature (Kou and Sun, 1985).

$$L_f = \begin{cases} 1 & T > T_l \\ \dfrac{T - T_s}{T_l - T_s} & T_s \leq T \leq T_l \\ 0 & T < T_s \end{cases} \qquad 4.7$$

Where T_l and T_s are the liquidus and solidus temperature respectively.

In the graph of figure 4.17(a), at all-time steps the surface is liquefied and the maximum depth is liquefied up to 640 μm. The liquefaction starts in the first millisecond, when the

laser beam vaporises the steel. The graph in figure 4.17(a) shows that the maximum depth is reached in the fourth millisecond.

Beyond four milliseconds, with each time step the depth at which molten steel is found decreases, as cooling mechanisms start to come into play. Beyond the fourth millisecond the laser has stopped firing and the weld pool starts to cool. At each time step the depth of the weld pool starts to solidify, starting from the bottom of the weld pool and working towards the top of the weld pool, see figure 4.17(b).

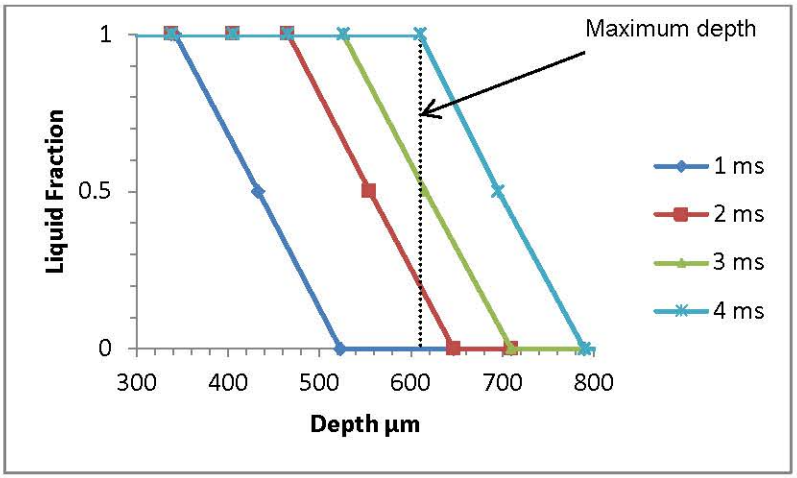

(a)

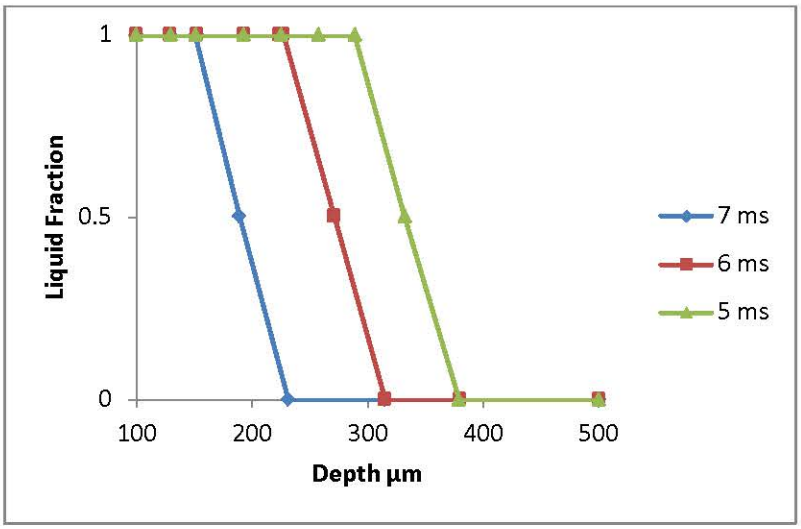

(b)

Figure 4.17. (a) and (b) The liquid fraction at various time steps and depths.

4.7.3 Heating and Cooling of the Weld Spot

During laser spot welding a local area is heated up rapidly resulting in high thermal gradients and resulting in a non-uniform temperature distribution. The graph in figure 4.18 shows the heating and cooling phase that occurs on the surface of the weld spot. The graph in figure 4.18 is a cross section of a hyperplane that is formed in three dimensional space for temperature, time step and the liquid fraction.

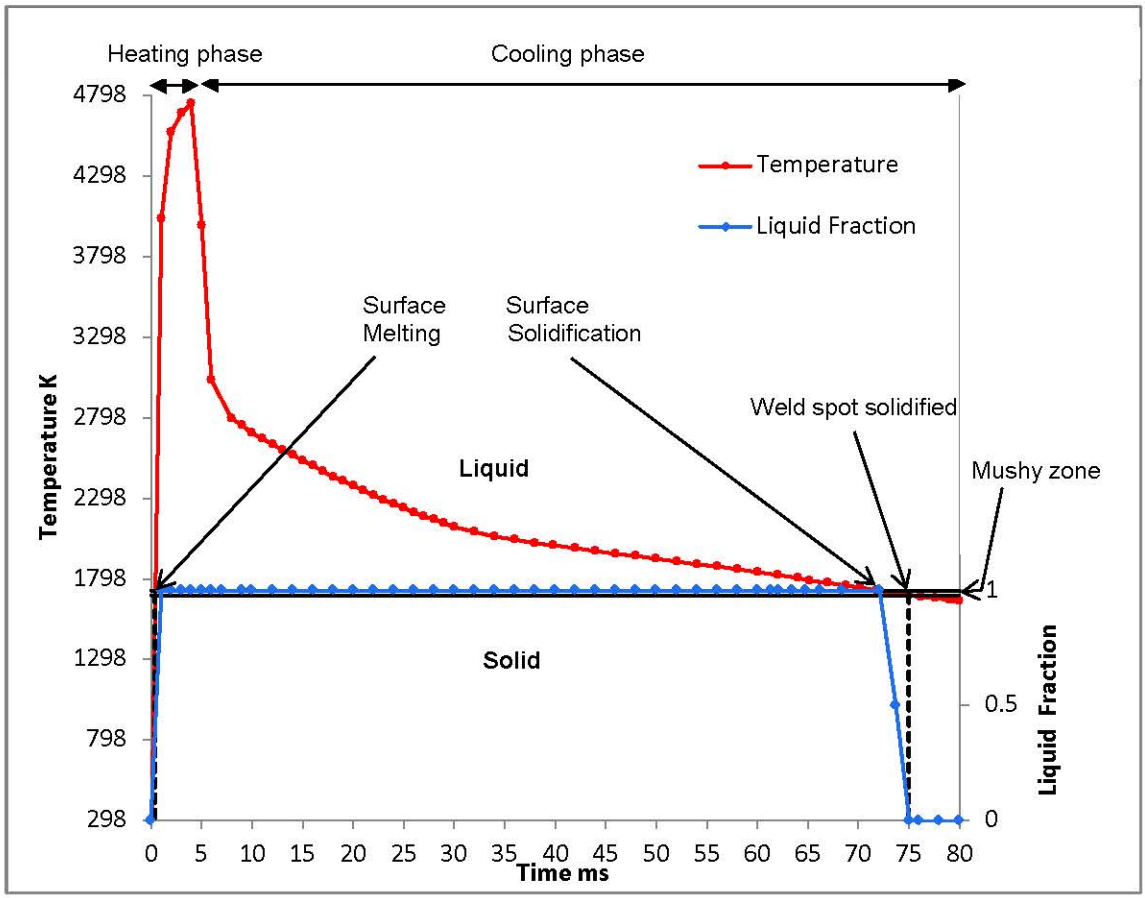

Figure 4.18. On the surface of the weld spot the evolution of the liquid fraction with respect to time, with the corresponding temperature at that time.

The heating phase occurs during the four milliseconds when the laser is firing. Initially when the laser fires not all of the laser energy is absorbed by the work piece. It takes 0.4 milliseconds before the surface starts to melt.

During the first four millisecond the temperature has rapidly risen in the work piece to a maximum and the maximum depth of melt is established. At the surface there is vaporisation of the steel. In the depth of the weld pool a keyhole forms.

Beyond the fourth millisecond there is a rapid exponential fall in the temperature. As the weld spot cools, at 71.8 milliseconds the liquidus temperature is achieved and the surface of the weld spot is in the mushy zone for 3.2 milliseconds. It takes 75 milliseconds for the weld spot to completely freeze.

4.8 Effective Stress

Stresses build up in three dimensions and can be summarised into an effective stress, also known as the Von Mises stress. The diagram in figure 4.19 shows the development of effective stress in the work piece 20 seconds after the formation of the weld spot. This diagram gives an indication of the magnitude of the residual stresses and the type of displacement that can be expected.

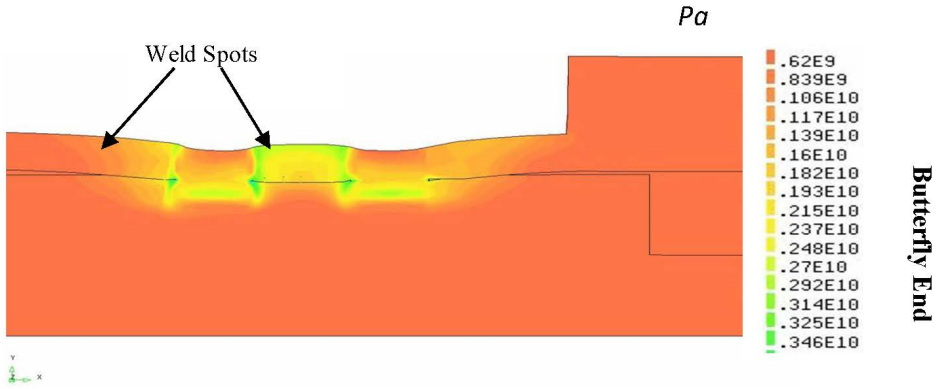

Figure 4.19. Model magnified by a factor of ten, showing displacements and stress.

After the weld pools have solidified the surface of the weld shows shrinkage. It appears to give a 'pinch' effect on the surrounding material. The surrounding material is drawn down towards and into the weld spot. This will result in the stress radiating down towards the optical fibre and outwards towards the ends of the work piece. However,

because of the different densities of the intervening materials between the weld spots and the optical fibre the effects of the stress are dampened and the stresses do not quite reach the end of the fibre pigtail.

The effective stresses very gradually increases from the tail end of the hard adhesive fillet. This levels out all the way along the fibre until the tail of the soft adhesive is reached, where there is slight dip, figure 4.20.

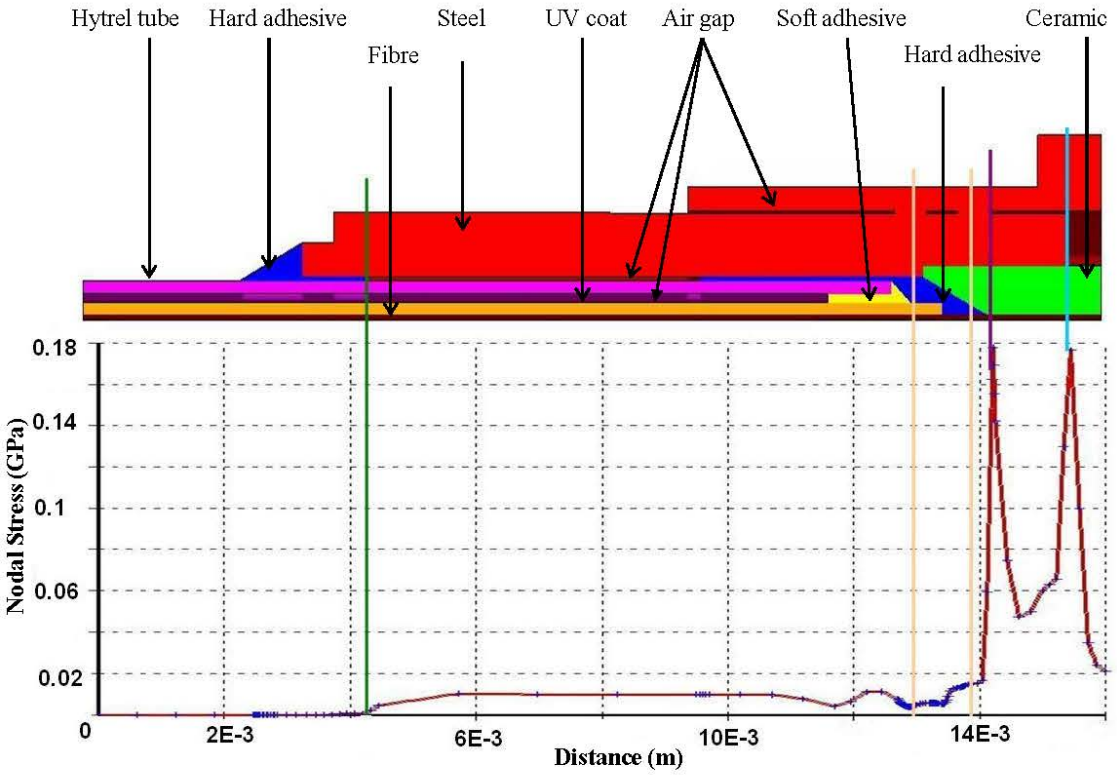

Figure 4.20. Plot of nodal stress along the distance of the work piece.

A graph was produced of the residual stress found along the length and located at the surface of the optical fibre, figure 4.20. In order to understand this graph a diagram of the work piece is superimposed above the graph showing the location of the stress along the different areas of the work piece. Peaks in the stress are observed at material interfaces such as the fibre and ceramic and the ceramic and ferrule interface. There is sudden and dramatic rise in the stress at the interface of the fibre entering the ceramic capillary. There is also a second peak at the ferrule and ceramic interface.

4.9 Displacements

The diagram in figure 4.21 shows the resultant displacements at a magnification factor of ten. As is to be expected the maximum displacement is seen in the weld spots near the surface. It follows the 'pinching' effect, of the material being drawn in towards the weld spots and radiating downwards. Most of the displacement appears to be absorbed by the steel sleeve. Only the location of the welding in the ferrule allows the displacements to continue into the body of the work piece. The displacements in the ferrule are greatly decreased. They appear to radiate towards the end of the pigtail as opposed to the butterfly end.

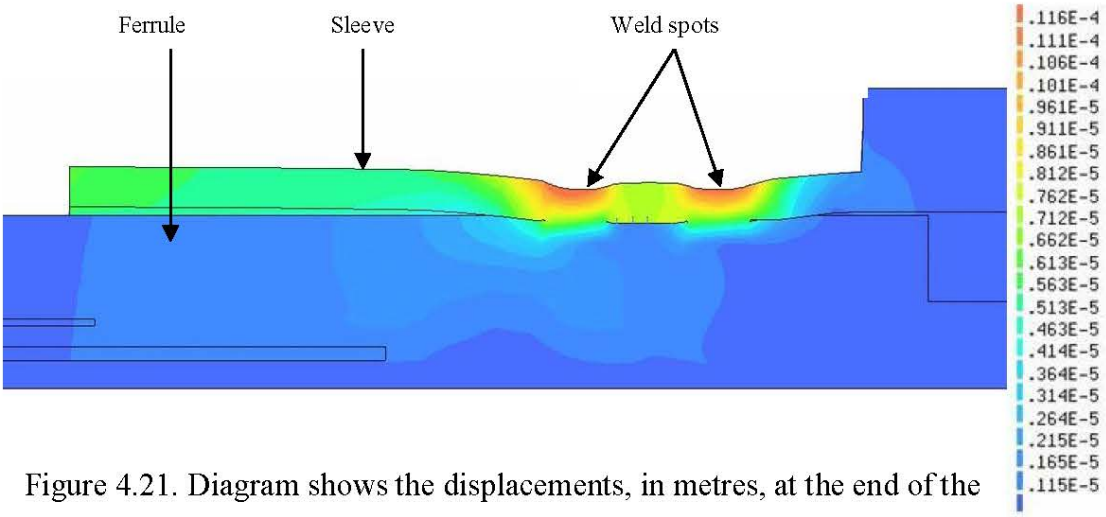

Figure 4.21. Diagram shows the displacements, in metres, at the end of the welding process at a magnification factor of ten.

The displacements of the fibre approximately follow the stress patterns of the fibre. The diagram in figure 4.22 is a graph of the resultant nodal displacements along the length of the fibre measured from the surface of the fibre. Above this graph is diagram of the work piece, indicating the approximate locations of the displacements.

The displacements start to increase at a steep rate of approximately 0.05 μm for each millimetre along the fibre, starting from the tail end of hard adhesive fillet. This can be explained by the soft nature of the materials allowing the fibre to move more freely.

The displacement peaks at the tail end of the soft adhesive. At the fibre and ceramic capillary interface there is peak in the displacement, due to the higher stresses in this

area, see figure 4.20. Once past this interface and into the body of the ceramic capillary there is a rapid decrease in the displacement of the fibre. There is a small peak in the displacement at the ferrule and ceramic interface due to high stress levels in this area, see figure 4.20.

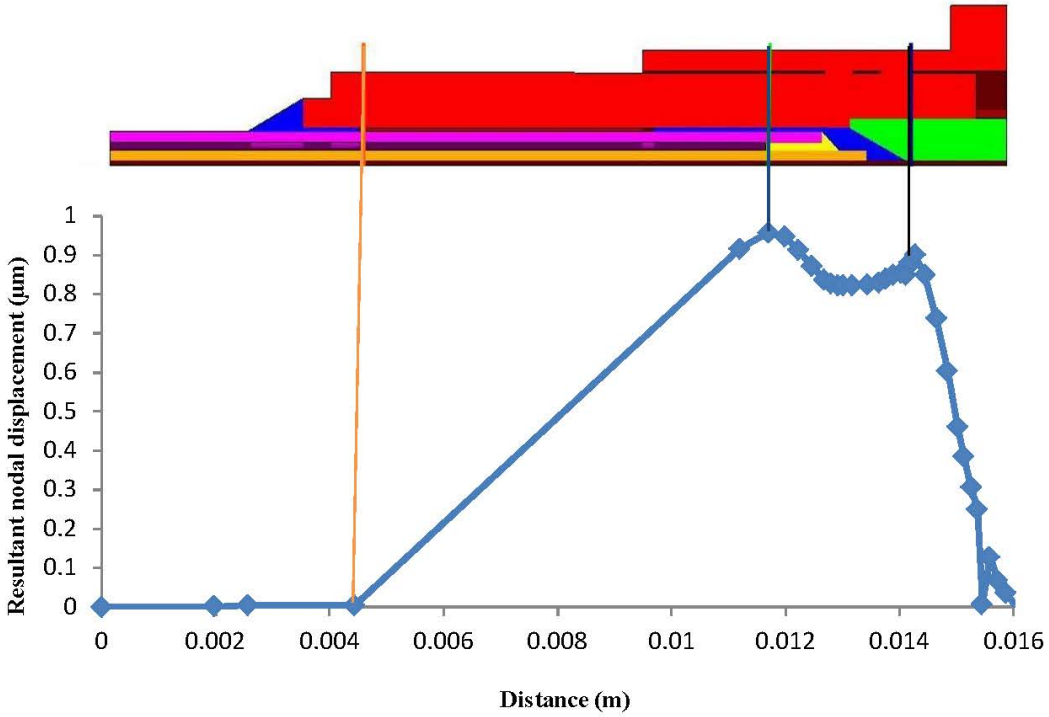

Figure 4.22. Shows the resultant nodal displacements (µm) along the length of the fibre (m), measured from the surface of the fibre.

A series of simulations were conducted to ascertain if it was possible to discover the relationship between the displacement or stress with the location of the weld spot. The welding simulations consisted of two weld spots made at various locations. The graphs of figure 4.23 show the relationship of stress and the displacement of the optical fibre for various locations of the weld spot. On each graph the inset indicates the distance from the centre of the weld spot from the butterfly end. The graph in figure 4.23 (a) shows the effective stress along the surface of the optical fibre. The graph in figure 4.23 (b) shows the displacement of the fibre at different locations for the weld spot locations.

From the graphs in figure 4.23 it is apparent that the weld spots which are the furthest from the butterfly end induce the least stress / displacements. However, no trend can be identified to locate the weld spots in an optimal location. Furthermore, due to the

welding parameters used at Oclaro the location of the weld spots far from the butterfly end were not feasible.

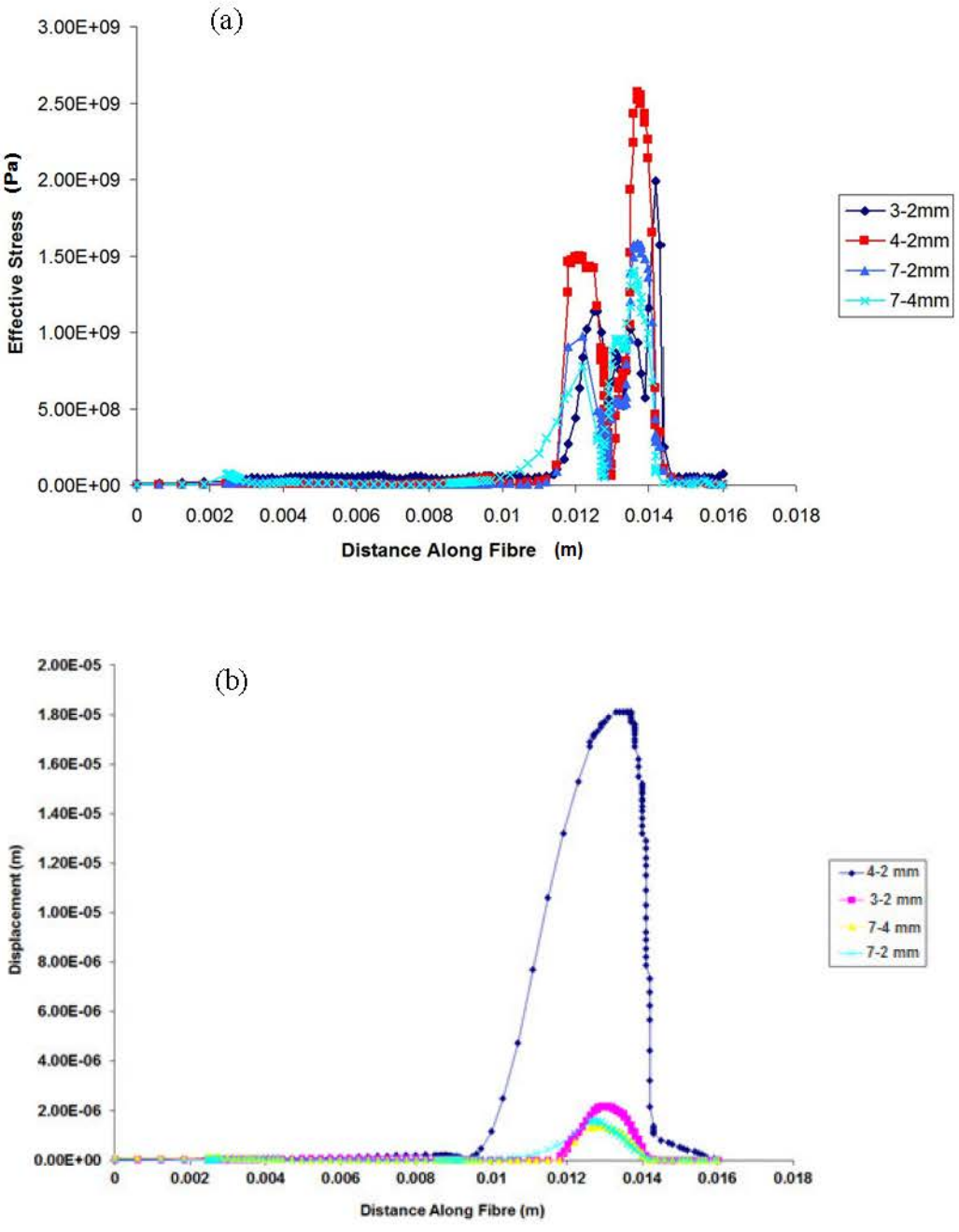

Figure 4.23. (a) Graph of the stress along the fibre. (b) Graph of the displacement along the fibre.

4.10 Conclusions

A number of numerical models were developed to simulate two weld spots at various locations from the butterfly end. The simulations showed that very high temperatures occur; the maximum temperature was of 4770 K. This temperature cannot be validated for this work, and others have found it to be challenging to use experimentation to confirm such temperatures (He el al, 2003). However, a survey of the type of temperatures found by others indicates that this can be a reasonable temperature to expect. The work of Shanmugam et al (2013) with micro laser spot welding has shown that the maximum temperature they achieved was 4707 K. This indicates the range in which the temperatures are likely to occur. This is not a like for like comparison with their work, as they used AISI 304 stainless steel and have taken into consideration the temperature dependent thermomechanical properties. Additionally, their geometry was simple, just a square thin sheet of steel. The work of Abdulateef (2009) with laser welding found temperatures of 5244 K. Desi and Bag (2014) with micro laser spot welding has shown that the maximum temperature they achieved was 3000 K.

It took 0.4 milliseconds of the laser pulse before the steel started to melt. Within this period most of the laser energy is reflected. Once the melt starts more of the laser energy is absorbed. Within the first millisecond the penetration depth of the weld spot is established. Also during this period the keyhole is formed and helps with absorption of the laser energy. Because of this the temperature starts to increase and peaks at four milliseconds. During this period all the cooling mechanisms of conduction and radiation come into play. At the end of the fourth millisecond the laser stops pulsing and there is rapid exponential cooling of the weld spot. The simulations showed that the weld spot completely freezes in 75 milliseconds.

The high thermal gradients that occur during laser welding cause localised expansion of the weld material. This expansion is constrained by the bulk of the cooler material. As the weld cools residual stresses develop as some areas cool and contract more than the other areas. This generates effective stresses that traverse deep into the fibre capsule.

The different components that comprise the fibre capsule are of differing densities, which affects the way the stress travels towards the optical fibre. At interfaces between

the package components and the optical fibre high levels of stress are observed. Since elasticity has only been modelled, the stress values will be expected to be higher than normal. The values of the von Mises stress generated in the fibre of the models are well below the yield stress value for optical fibres. Depending on the composition of the optical fibre the quoted yield stress ranges between 4.91GPa - 5.4GPa (Dwivedi and Glaesemann, 2011). It is the effective stress that causes the displacement in the optical fibre, and the misalignment with the laser source.

An additional aim of these simulations was to identify any relationship between the location of the weld spots and the stress induced and the displacement of the fibre. Since there appears to be a correspondence between the development of the effective stress and the displacement of the fibre. The generated stress can be taken as a response to the cooling of the weld spot and the misalignment with the laser source.

The only welding parameter that was studied in relation to these simulations was the location of the weld spots. Further welding parameters need to be included into the model which would change the stress patterns as compared to those currently observed. With this view in mind the next stage in the project was the design of experiments and the development of the surrogate model.

Chapter 5

Simplified Axisymmetric Model

This chapter fulfils the objective for the development of a high fidelity model that will be used with design of experiments. Clearly from the previous chapter the thermomechanical model is a sophisticated model in its development and the results it produced. Further the results show no clear cut indication of how the effective stress generated in the optical fibre can be related to the distance between the weld spots. To find such a relationship a design of experiments will be conducted. Ordinarily the model developed in chapter four would be used to develop the surrogate model using design of experiments. The industrial project partner was interested in changing the welding process and the model that was required was axisymmetric. A further requirement by the industrial project partner was the simplification of the FE model.

5.1 Modelling Considerations

The modelling of the weld pool physics requires the inclusion of buoyancy and surface tension driven convection, solid-liquid and liquid-vapour phase change, laser-vapour plume interactions and pool surface deflections. Capturing such physics is not always necessary and can be neglected. This has already been seen in work analysing distortions in welded structures through the heat distribution and modelling of welding, (Mobarhan et al., 2000, Mueller and Valk 2000, Zhou & Tsai, 2008, Kazemi & Goldak, 2009, Pang et al., 2008, Song et al., 2009).

It can be assumed that only a small shrinkage region needs to be considered as the welding consists of a weld location on an axisymmetric model. The temperature gradients will be high in the surrounding area. The local area in and around the weld location will see significant plastic deformation during the cooling phase due to the extreme temperatures.

When the material in the shrinkage region melts it is known as the mechanically molten state in which all stresses are relaxed (annealed). Up to this point in the simulation there are no residual stresses, therefore the heating phase can be neglected. When the material cools it regains its stiffness to produce the residual stresses and distortions, which are of interest. Hence, during the simulation a thermal load is assumed at the weld locations starting at a temperature of 1693 K the solidification temperature of steel (Lightfoot, 1930). Once the cooling of the material starts, residual stresses and distortions are produced as the contractions are resisted by the surrounding cooler material.

5.2 The Model

The model has changed from chapter four, into an axisymmetric model. This will be a three dimensional construct that is rotationally symmetrical about an axis. The axisymmetric model was developed as there is an interest by the project partners in investigating a change in the welding process to a continuous weld line to secure the sleeve to fibre capsule ferrule.

In addition to the three dimensional axisymmetric finite element model of the fibre package, another requirement of the industrial partner was the simplification of the geometry. The materials in the package that are captured in this model include steel, air, adhesive, Hytrel tube, UV coat, glass fibre and ceramic. The model is illustrated in figure 5.1.

The glass fibre is coated with a UV coat. This is protected by a Hytrel tube. The glass fibre lies at the centre of the system. A portion of the glass fibre as it enters the ceramic capillary is stripped of both the UV coat and the Hytrel tube. All these components are protected by the steel ferrule. Adhesive is used to maintain the position of the Hytrel tube and the stripped glass fibre in the ferrule. The ferrule is encased in a steel sleeve. The sleeve is attached to the ferrule by micro laser welding. There is an air gap between the glass fibre and the Hytrel tube. There is also an air gap between the sleeve and the ferrule, which may vary by up to 20μm.

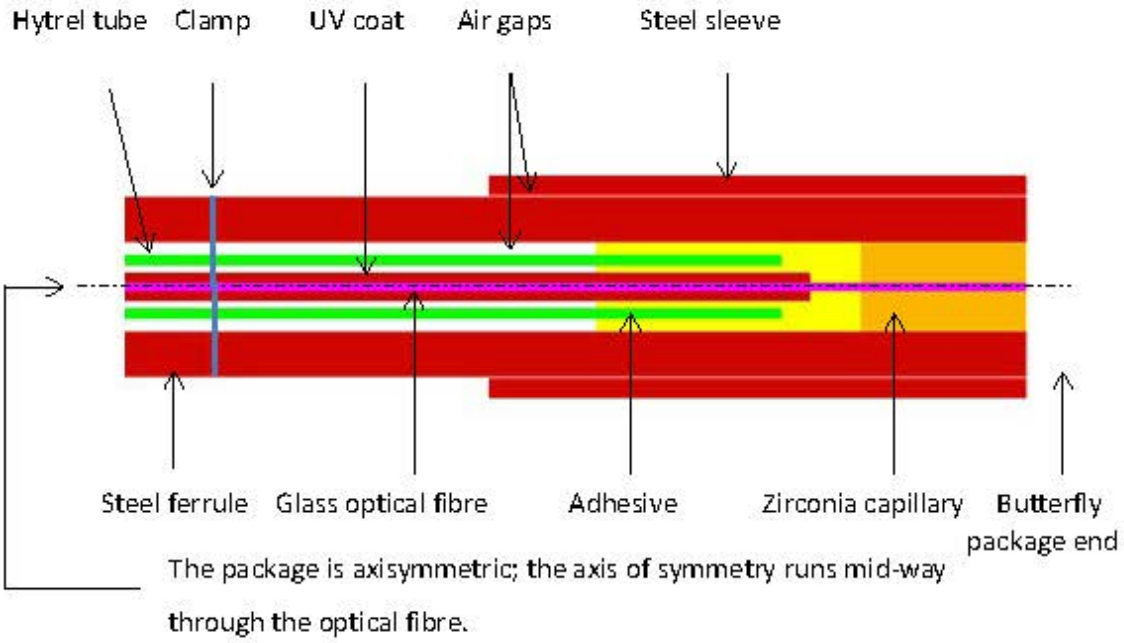

Figure 5.1. The materials and the geometry of the complete fibre capsule.

The two weld lines are represented as two weld locations on the axisymmetric model. The first weld line is located at one millimeter from the butterfly end as stipulated by the industrial partner. The location of the second weld line is given as the distance between the two weld lines, the interweld distance.

The modelling work was undertaken using FEMGV software package (Femsys, n.d.), as a CAD and mesh generation tool and also to post-process and visualise the analysis results. The multi-physics simulation package PHYSICA was used in this work as the analysis tool (Physica, n.d.).

5.3 Assumptions & Material Properties

The finite element analysis modelling is based on the following assumptions:

- The welds form simultaneously.
- The welds are formed successfully to bridge the gap between the sleeve and the ferrule.
- In the model it is assumed that all the components sit squarely in the air gaps.

- The simulation will start from when the temperature in the weld location is at 1693 K, the rest of the domain is at room temperature.
- The only heat losses that have been included in the model are radiation and conduction.
- All the materials are assumed to behave elastically.

The physical constants and material properties of the package used in the simulations are shown in table 5.1.

Table 5.1. The material properties, laser settings and constants used in the model.

	TCE ppm/K	Thermal Conductivity W/m.K	Specific heat J/g/K	Density g/cc	Young's modulus GPa	Poisson's ratio
Stainless steel 304L	17.5	16.3 (100degC)	0.5	8	200	0.248
Ceramic capillary (zirconia)	10	2.1	0.4	6	205	0.3
Fibre (glass)	0.49	1.6	0.7	2.1	73	0.17
UV Buffer coat on fibre (polymer)	120	0.2	1.5	1.1	1	0.5
Adhesive 1 (tube to fibre coat)	110	0.2	1.4	1.2	1.6	0.35
Adhesive 2 (fibre to capillary)	50	0.35	1.4	1.2	2.3	0.35
Hytrel Tube	135	0.25	1.0	2.2	0.55	0.45

5.4 Model Boundary Conditions

The initial condition for the weld spot is –

$$T = T_0 \text{ at } t = 0 \qquad 5.1$$

So that

$$k\frac{\partial T}{\partial x}l_x + k\frac{\partial T}{\partial y}l_y + k\frac{\partial T}{\partial z}l_z - q + h(T - T_\infty) = 0 \qquad 5.2$$

Where h denotes surface heat loss coefficient, l_x, l_y and l_z the direction cosines to the boundary surface. The surface temperature and environment temperature are denoted T and T_∞ respectively. The thermal conductivity and heat source are given by k and q respectively.

In this analysis, a thermal load of 1693 K, the solidification temperature of steel, is the initial temperature for the weld spot. For the remainder of the domain the initial temperature is set at room temperature, 298 K. Using a face patch for the weld location to which the boundary condition is specified. The source which is added per unit area to the face patch is set to 1693 K. Using a heat transfer coefficient the temperature of the weld spot is brought down to room temperature (298 K). As the weld spot cools stresses are generated in the weld piece.

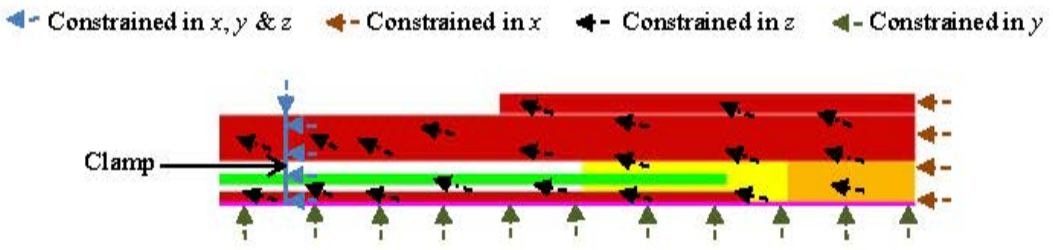

Figure 5.2. Mechanical boundary conditions.

The boundary conditions also include the mechanical boundary conditions. The same mechanical boundary conditions were used as in the previous chapter, see section 4.6.1. The model was constrained at the location of the clamp in the x, y and z direction. The face of the plane was constrained in the z direction. The model was also constrained at the lower surface in the y direction and at the butterfly package end in the x direction, see figure 5.2. A number of experiments were performed to ensure that the model was time step and mesh independent.

5.5 Numerical Analysis Results

This section details the finite element analysis predictions for designs that were developed for the DoE, as an illustration of the high fidelity modelling calculations.

5.5.1 von Mises Stress

A graph of the residual stress found along the length and located on the surface of the optical fibre is shown in figure 5.3. The models that produced the maximum and the minimum stresses as part of the design of experiment are shown in figure 5.3.

In order to understand the graphs in figure 5.3, a diagram of the work piece is superimposed above the graph indicating the location of the stress along the different areas of the work piece. The top graph shows the maximum level of stress achieved for the design of experiment which occurred at design point combinations of ABCD, see table 6.2. The lower graph shows the least stress achieved for the design of experiment which occurred at design point combinations of AD, refer to table 6.2.

In both graphs the stress peaks are observed where there is a change in the material interface. These being the adhesive / ceramic capillary interface and ceramic capillary / air interface. These peak stresses at the interfaces have also been discussed previously in section 4.8.

The materials of the fibre package with a higher density propagate the stresses better. There is a sudden and dramatic rise in the stress at the interface of the ceramic capillary and the adhesive as shown in figure 5.3.

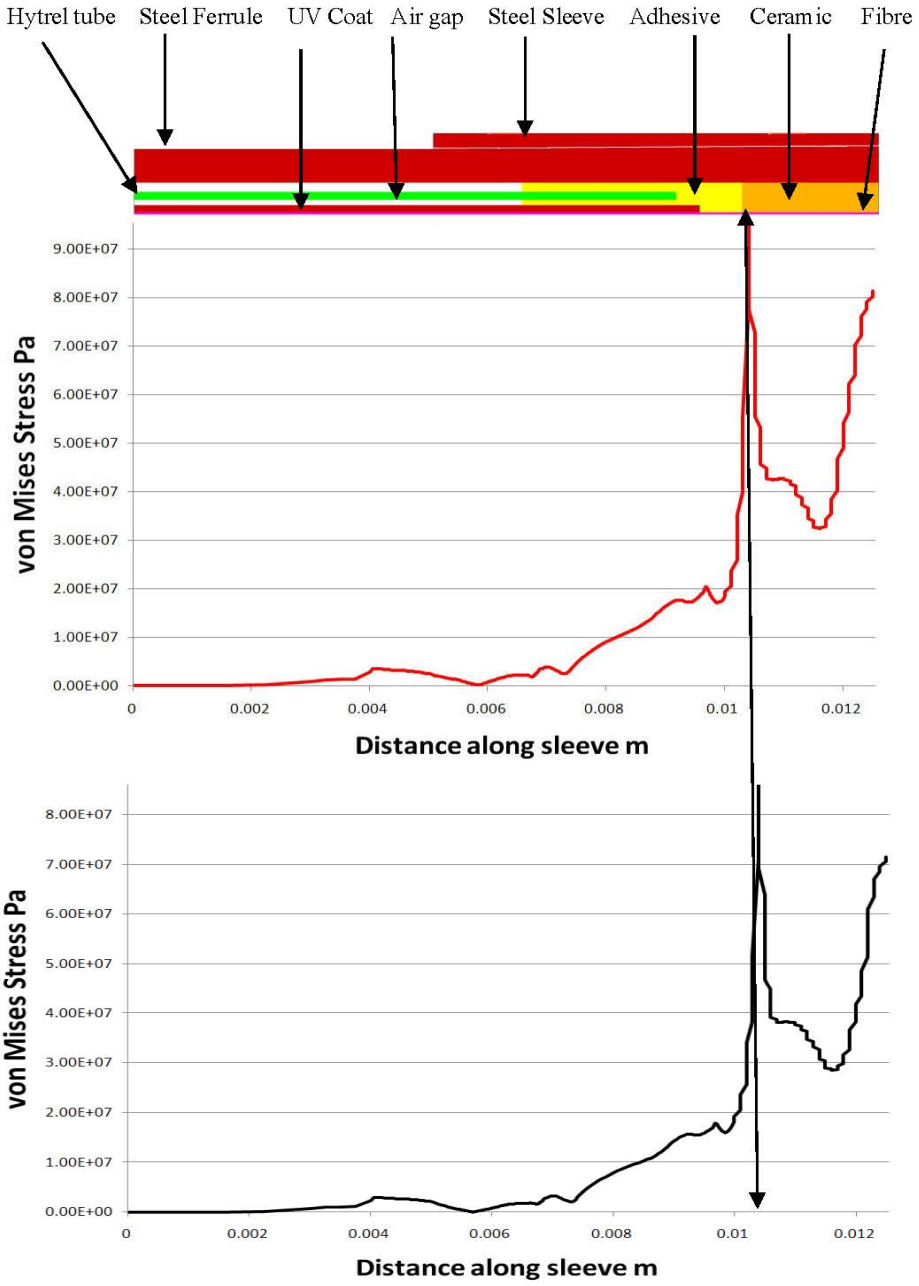

Figure 5.3. The stress profile along the length of the surface of the fibre.

Once the body of the ceramic capillary is reached, the levels of stress decrease. There is also a second peak at the ferrule and ceramic interface. At both the interfaces there are high levels of stress as indicated in figure 5.3, and are due to the coefficient of thermal expansion mismatch of the different materials.

The diagrams in figures 5.4 and 5.5 show the development of effective stress in the work piece. These diagrams give an indication to the type of stresses that can be expected.

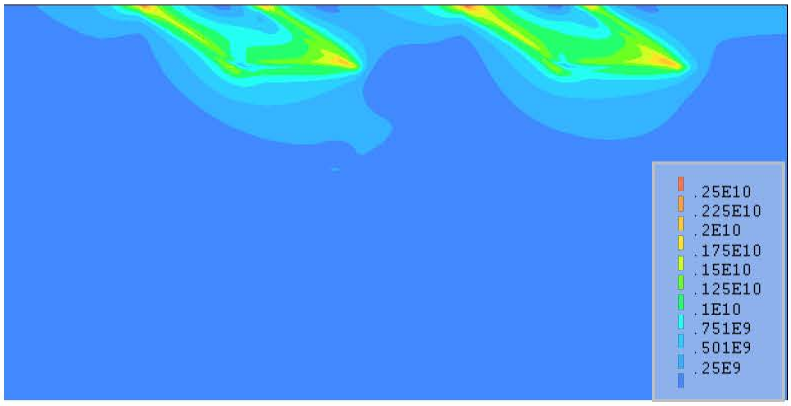

Figure 5.4. Weld locations showing the von Mises stress, the stress values are in Pascals.

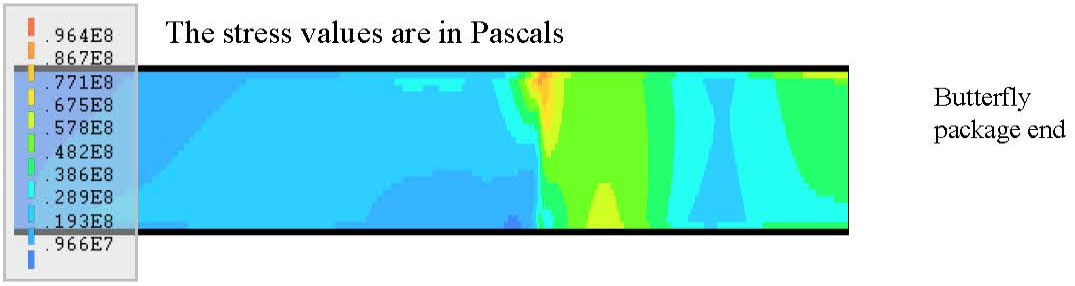

Figure 5.5. Stress in the optical fibre. This region of the fibre corresponds to the area below the weld locations shown in figure 5.4.

After the weld pools have solidified the surface of the weld shows shrinkage. It appears to give a "pinch" effect on the surrounding material. The "pinch" effect can be seen when displacement is visualised, see figure 5.6.

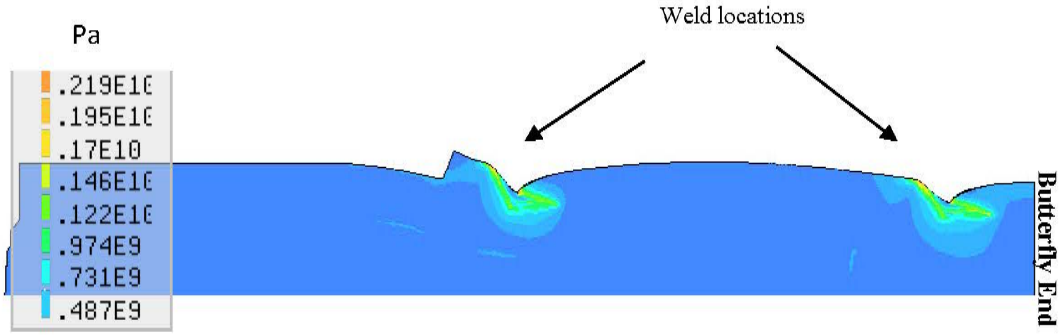

Figure 5.6 Stress pattern in fibre package. The resultant displacement has been magnified by a factor of ten.

As it is assumed the material will behave in a linear elastic manner, the magnitude of the observed stress values are higher than what would be expected. This is because in this model non-linear plastic material models are not utilised due to lack of sufficient data. The model can be easily updated to account for such non-elastic behaviour if this material data becomes available. The key prediction is the magnitude of the stresses, which will affect the fibre alignment.

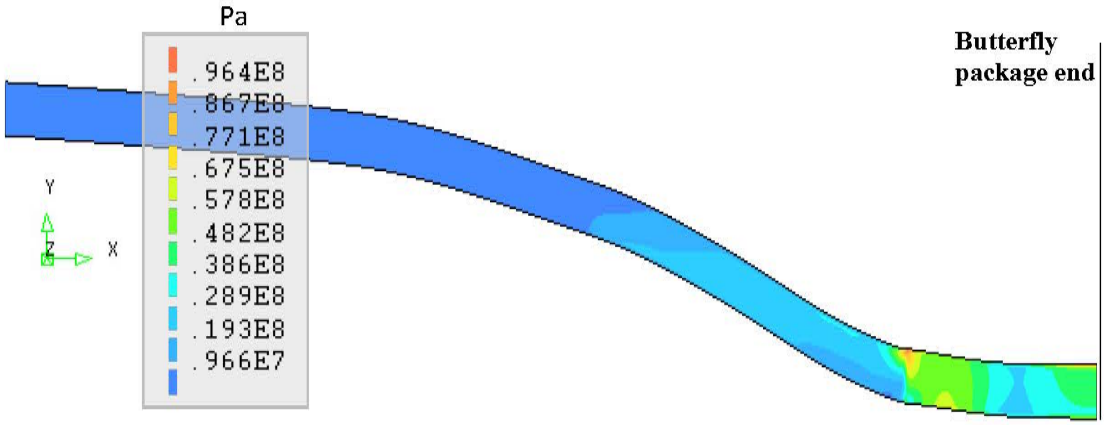

Figure 5.7. The stress pattern in the glass fibre optic. The stress values were measured on from the surface of the optical fibre. The resultant displacement has been magnified by a factor of ten.

5.5.2 Displacements

The diagrams in figures 5.6 and 5.7, show the resultant displacements using a magnification factor of ten to clearly visualise the deformation mode. As is to be expected the maximum displacement is seen in the weld locations near the surface. It is evident that the material is drawn in towards the weld spots. Most of the displacement appears to be absorbed by the steel sleeve.

It is evident that the surrounding material is drawn towards and into the weld location. This will result in thermal stresses propagating down towards the optical fibre. Because of the different intervening materials between the weld spots and the optical fibre the pattern of stress distributions across the package materials becomes non-linear.

5.6 Conclusion

The sixth objective of developing a simplified axisymmetric finite element model has been implemented in this chapter. There are advantages that a number of researchers in the field of modelling and simulations have identified for the need of keeping models as simple as possible (Lindgren 2001, Montgomery 2007 and Myers et al., 2009). The prime reason for simplification is cost in terms of resources. Additionally, detailed modelling of the physics of the weld pool, which are complex, were not included in this work, as this was not of interest and need not be modelled (Mobarhan et al., 2000, Mueller and Valk 2000, Zhou & Tsai, 2008, Kazemi & Goldak, 2009, Pang et al., 2008, Song et al., 2009). Had they been kept they would not have added any value to the results. Further, they would have added an extra burden in computational time and in developing the model.

Only the thermal responses of the weld spot were of interest and were developed in the model. Since the objective of the modelling was to predict the residual stresses in the weld piece once the weld had formed. The model was relatively less time consuming computationally and with respect to developing it. This model will now be used in the next chapter within design of experiments to develop a surrogate model.

The simplified model appears to model comparatively similar to the full three dimensional model of chapter four. In the weld locations the direction of the shrinking

in both models gives a pinching effect that goes inwards and towards the depth of the weld. The stress along the fibre in both models shows a similar stress pattern. The stress develops along the fibre and peaks at the material interfaces. The stress value at the surface of the weld spot are in the similar range for both models.

Chapter 6

Surrogate Modelling

This chapter covers the seventh objective of developing a predictive surrogate model. This involves analytical and computational techniques used with the design of experiments to develop such a model.

Even with the increase in computational power many computer simulations are resource intensive. This has already been mentioned regarding FEA, which involves the preparation of high fidelity models. Other resource intensive techniques include Monte Carlo simulations that can comprise of millions runs. The method used to overcome such issues involves the creation of a surrogate model of the system. Surrogate modelling is a process by which a complex model, which can be a computer model or a physical experiment, can be simplified as a function. Surrogate models are also known as metamodels.

The system behaviour of the micro laser welding induced residual stresses in the optical fibre are captured by using a set of orthogonal experiments in the form of a design of experiments. The design of experiments methodology allows the generation of the maximal amount of knowledge of a system using the least number of experimental runs. The experimental runs are in the form of FEA simulations.

The objectives of the design of experiments is to:

- Identify the key process variables, sensitivity analysis.
- Estimate a surrogate model, quantifying the dependence of the response variable on the process inputs.

The thermomechanical model developed in the previous chapter is used to determine the distribution of the post welding stresses in the optical fibre due to different process specifications.

The main steps of developing a surrogate model are illustrated in figure 6.1. The factors that affect the response are identified. In this work it will be the factors that affect the development of the residual stresses in the fibre which cause the displacement of the optical fibre.

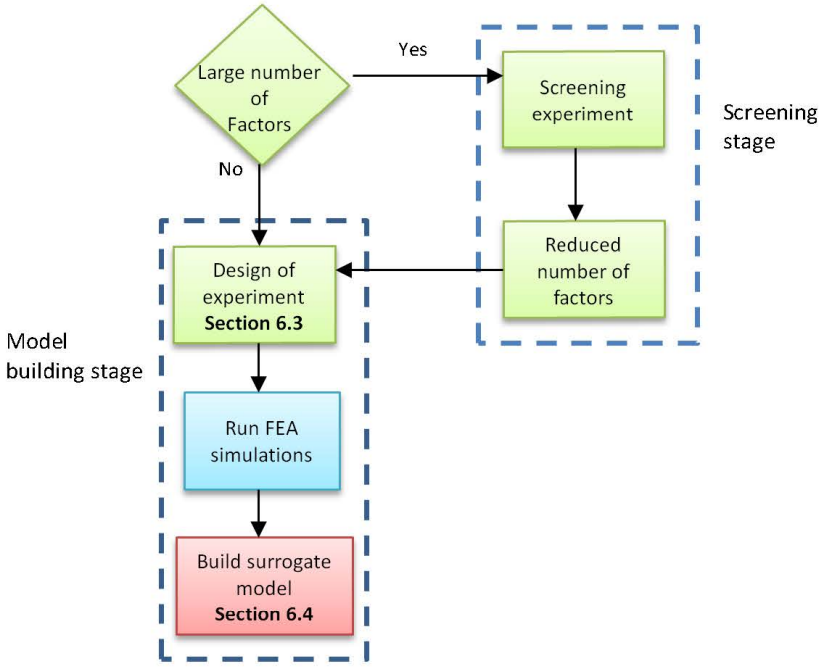

Figure 6.1. Design of experiments and surrogate modelling.

If there are a large number of factors which are thought to affect the response, then screening experiments, using fractional factorial designs of experiments are performed to identify the key factors. For the design of experiments (DoE) the runs will consist of FEA simulations, where each experiment will be represented by a FE model. To construct a surrogate model from the DoE data a least squares method is used to build a first order polynomial linear with interactions function.

6.1 Identifying the Key Process Parameters

After discussions with the engineering team at Oclaro, a number of design variables that are thought to contribute to the generation of post welding stresses were identified. This included the laser power, laser beam diameter and the type of steel used for the ferrule. Either for commercial reasons or for reasons that will affect the geometry of the weld spot these variables were ruled out. However, five other design variables that are thought to contribute to the generation of post welding stresses in the optical fibre were identified and investigated as part of this methodology. The design variables are:

- The inter-weld distance between the two micro weld spots. The first weld spot is one millimetre from the butterfly package end.
- The air gap between the sleeve and ferrule
- The angle of the laser
- The diameter of the weld spot
- Weld spot penetration depth.

The design variables are also known as factors or process parameters. The factors have a setting or level at which the welding process occurs. The levels that were identified were those that are used on the Oclaro laser welding machines. They range from the minimum to the maximum levels as identified by the Oclaro engineering team, see table 6.1.

Table 6.1. Limits of the factor settings

Design Variable	High Level	Low Level
Air Gap	20 μm	0 μm
Interweld Distance	4.7 mm	1 mm
Weld Diameter	0.7 mm	0.6 mm
Weld Penetration	640 μm	620 μm
Laser Angle	35°	30°

Different combinations of values for the above design variables that are used in the manufacturing process by Oclaro are combined as part of the design of experiments to construct a series of FEA models. These models are used to evaluate the post welding

stresses in the fibre optic. The data generated from the design of experiments is then used to construct a surrogate model in the form of an explicit polynomial approximation. This model is a function of the five design variables and can be used to perform a sensitivity analysis and evaluate the impact and significance of the parameters on fibre stresses.

The surrogate model will be used to fulfill the aim of the OPISA project. Which is to identify a welding location on the sleeve–ferrule package that minimises the stress and hence the displacement of the optical fibre, thus ensuring optimal fibre–laser coupling. The welding location has to be within the parameters of the welding regime and the weld piece geometry used by Oclaro.

The remainder of this chapter focuses on the analysis of the performance of the package within the entire design space defined by the five design variables and the ranges for their variation. The methodology of integrated design of experiments and surrogate modelling aids risk analysis and design improvement which is part of the OPISA methodology and will be discussed in detail in the next chapter.

6.2 The Design of Experiment and Results

A matrix is created to show all the possible combinations of high and low levels for each factor. This matrix is called an analysis or model matrix for the DoE. Table 6.2 shows the model matrix, where each factor setting for each level is given in coded form, so that the high level is "+1" and the low level is "-1". The design matrix for any full factorial experiment has columns that are all pairwise orthogonal and all the columns sum to zero. Orthogonality eliminates correlation between the estimates of the main effects and interactions.

The design variable limits that specify the design space under investigation are listed in table 6.1. The high and low level are based on the upper and lower values that can occur for the welding process as identified by Oclaro. A two level design was chosen as it has a number of advantages which include sequential experimentation and allows for simple graphical analysis of main effects and interactions (Box et al., 1978).

Table 6.2. Five factor full factorial design matrix with results of the experiment.

Combination	Factors					Result
	Air Gap A	Interweld distance B	Weld diameter C	Weld penetration D	Laser angle E	Stress GPa
1[1]	-1	-1	-1	-1	-1	0.1050
A	+1	-1	-1	-1	-1	0.0834
B	-1	+1	-1	-1	-1	0.1440
AB	+1	+1	-1	-1	-1	0.0942
C	-1	-1	+1	-1	-1	0.1200
AC	+1	-1	+1	-1	-1	0.0954
BC	-1	+1	+1	-1	-1	0.1640
ABC	+1	+1	+1	-1	-1	0.1100
D	-1	-1	-1	+1	-1	0.1080
AD	+1	-1	-1	+1	-1	0.0634
BD	-1	+1	-1	+1	-1	0.1470
ABD	+1	+1	-1	+1	-1	0.0820
CD	-1	-1	+1	+1	-1	0.1230
ACD	+1	-1	+1	+1	-1	0.0717
BCD	-1	+1	+1	+1	-1	0.1640
ABCD	+1	+1	+1	+1	-1	0.0966
E	-1	-1	-1	-1	+1	0.1060
AE	+1	-1	-1	-1	+1	0.0860
BE	-1	+1	-1	-1	+1	0.1470
ABE	+1	+1	-1	-1	+1	0.0940
CE	-1	-1	+1	-1	+1	0.1200
ACE	+1	-1	+1	-1	+1	0.0993
BCE	-1	+1	+1	-1	+1	0.1660
ABCE	+1	+1	+1	-1	+1	0.1140
DE	-1	-1	-1	+1	+1	0.1090
ADE	+1	-1	-1	+1	+1	0.0869
BDE	-1	+1	-1	+1	+1	0.1500
ABDE	+1	+1	-1	+1	+1	0.1020
CDE	-1	-1	+1	+1	+1	0.1230
ACDE	+1	-1	+1	+1	+1	0.0986
BCDE	-1	+1	+1	+1	+1	0.1230
ABCDE	+1	+1	+1	+1	+1	0.1690
Centre Point	0	0	0	0	0	0.0576

[1] By convention "1" is used to denote all the factors at the low level.

Ordinarily experiments contain random errors. It is assumed that the random errors are normally distributed with a mean of zero and a variance σ^2, written as $N(0,\sigma^2)$. To estimate the errors replicates of the experiment are performed. The experiments that were conducted in this study are based on using a thermomechanical FEA models. Such deterministic computer simulations would always generate identical responses from replicates; hence the design matrix contains no replicates.

In order to evaluate the stress for any particular set of values of the factors (so called design points), a FEA model was generated with those design parameters. The response was selected as the peak von Mises stress developed in the fibre after cooling of the weld spot had occurred. The performance of the package was judged based on the lower values for stress resulting in less misalignment between the optical fibre and the laser source and hence a lower risk of failure.

In this work, a full factorial DoE method is used. This is a design where all the level combinations of each factor are used equally. If there are n factors and the i^{th} factor has l_i levels, the numbers of design points (runs), j, in a full factorial design are given by:

$$j = \prod_{i=1}^{n} l_i \qquad \textbf{6.1}$$

This method specifies 32 (2^5) design points in the five-dimensional design space of the analysed design variables as shown in table 6.2. At each design point, a design variable is either at its low or high design limit. The 32 DoE points correspond to the corner points of the five-dimensional hypercube defining the design space of interest.

It is recommended, (Khuri and Cornell, 1996), that centre points, are also added to the experiment to test for curvature. The coded form for the centre point has the value of "0". As an example in figure 6.2, the design points represent a two factor design at two levels.

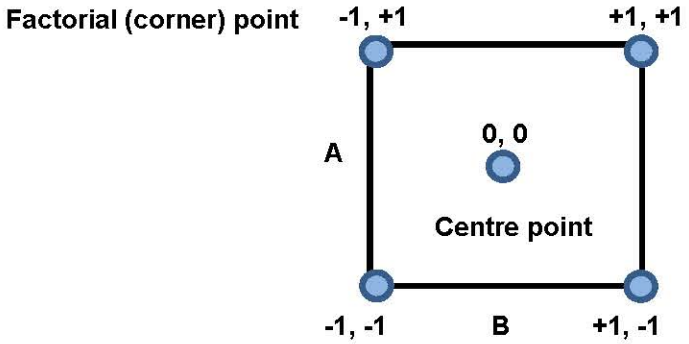

Figure 6.2. With two factors, A and B, the diagram shows the location of the centre point and the corner points, with the level of each factor in coded form.

The factorial (corner) points are the experimental runs and are set at their high and low levels. The centre point represents the experimental run when the factor levels are set at the half way point between the high and low level, see figure 6.2. The centre point will check for curvature in the response surface, see figure 6.3. The response will be either higher or lower at the centre point than the average response at the factorial points. Curvature is usually found when the factor settings are near a maximum or minimum response value.

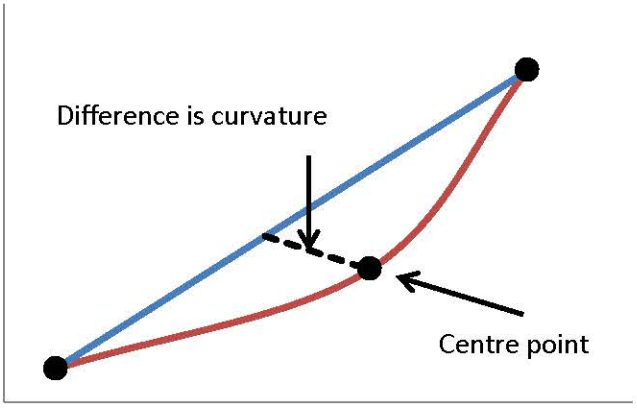

Figure 6.3. Test for curvature, which is usually present when factor settings are near a maximum or minimum response value.

6.3 Developing the Surrogate Model

The process of developing the surrogate model consists of a number of steps. Between these steps statistical techniques are used to ensure the validity of the modelling process. This process is summarised in figure 6.4, each of the numbers adjacent to the boxes refers to the section in this chapter.

To fulfil the assumptions of the modelling and the requirements of some of the statistical methods that will be used necessitates the data to be normally distributed. So the first step is to ensure the data is normally distributed by using the Anderson-Darling test. If the data is not normally distributed the data has to be first normalised using a Box-Cox transformation or Johnson transformation.

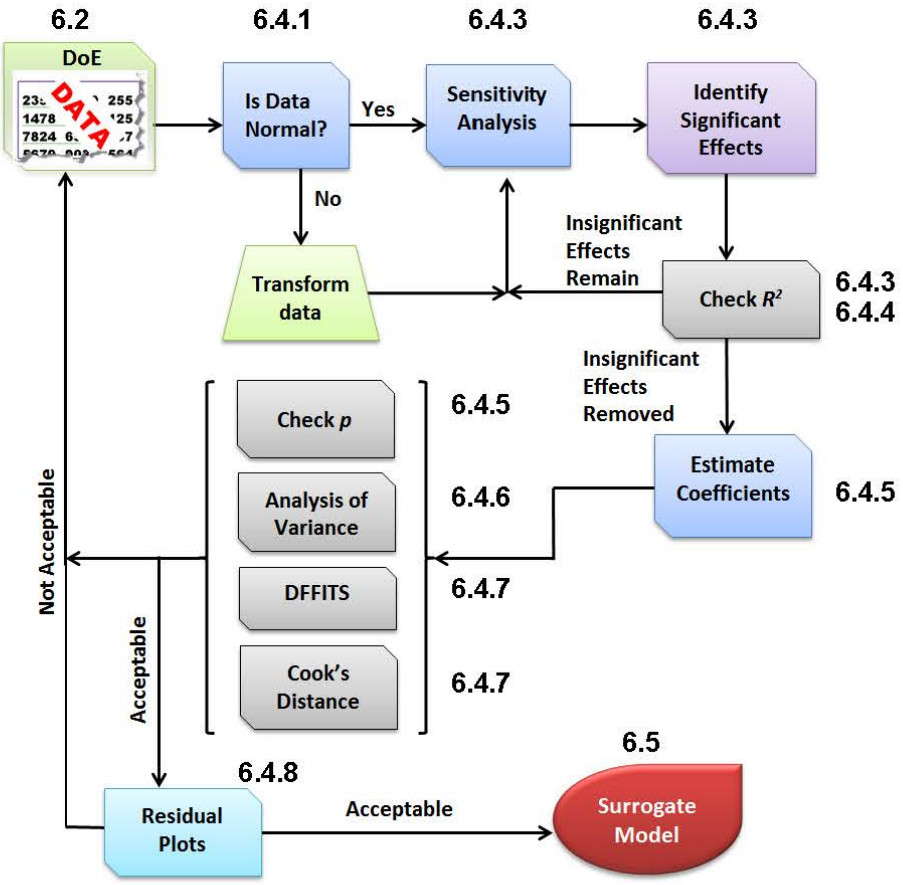

Figure 6.4. Summary of steps used to create the surrogate model, the numbers refers to the sections in this chapter.

Once it has been ascertained the data is normal, a sensitivity analysis, is performed to identify which factors should be kept in the model. This is an iterative process, and can involve several iterations to identify significant effects.

Next, the coefficients of the surrogate model are estimated. Once these have been estimated statistical techniques are used to confirm that the estimated coefficients did not occur due to chance alone, and are statistically significant. The accuracy and predictive power of the model is also checked. This also includes investigating the data points to identify any outliers or points that could cause any undue influence on the remaining data points.

Finally the plots of the residuals are inspected to establish that none of the assumptions have been violated in developing the surrogate model.

6.4 Analysis of the Results

The simulations from the DoE gave the results for the maximum stress in the fibre for each design point, as shown in table 6.2. The next modelling step is to build an explicit analytical surrogate model that can be used to make predictions for stress in the fibre, as a function of the five design variables being discussed. The principle is to use the available DoE data and to fit a mathematical model to this data thus having an explicit approximate expression for stress in the optical fibre.

The advantage of building the surrogate model is that once available it can substitute the set up and run of a finite element analysis model in evaluating any design point in the defined design space. Using a least squares method the surrogate model is constructed. The least squares method was implemented using Minitab v16 (Minitab, n.d), to give a linear with interactions polynomial function relating the design variables to the maximum stress in the fibre optic.

The general form of the surrogate model for the von Mises stress, σ_{vm}, in the fibre optic is given as:

$$\sigma_{vm} = c_0 + \sum_{i=1}^{5} c_i x_i + \sum_{j \geq i=1}^{5} c_{ij} x_i x_j \qquad \textbf{6.2}$$

Where x_i is the design variables and c_i and c_{ij} are the polynomial coefficients.

6.4.1 Normality Testing

The Anderson-Darling test is used to test for normality, which is defined as whether the null hypothesis, the distribution of the data is a normal distribution. The alternative hypothesis being the distribution of the data does not follow the normal distribution.

The test statistic is given by A^2, at a significance level of α at 0.05, the tabulated critical value is given as 0.787, and when α = 0.01 the critical value is 1.092. The null hypothesis is rejected if:

p <= α or A^2 > critical value

A visual inspection of figure 6.5(a) shows that the frequency histogram approximately follows a symmetrical bell shaped normal curve. The histogram data is overlaid with a normal curve which helps to assess the normality of the data.

However, a more accurate method of assessing normality is by using the data from the Anderson-Darling test. The A^2 value is less than the critical value of α at both 95% and 99%, the null hypothesis is not rejected, and it must be concurred that the data is normally distributed. Figure 6.5(a) also shows other summary statistics concerning the results data.

The probability plot, figure 6.5(b), shows the data approximately follows closely the reference line, which visually confirms that the data is normal. The reference line is the fitted cumulative distribution function which is based on the parameter estimates from the data. Because the data is normal the analysis of the data can proceed with respect to

the design of experiment. As estimating the effects, interactions and sensitivity analysis require the data to be normally distributed.

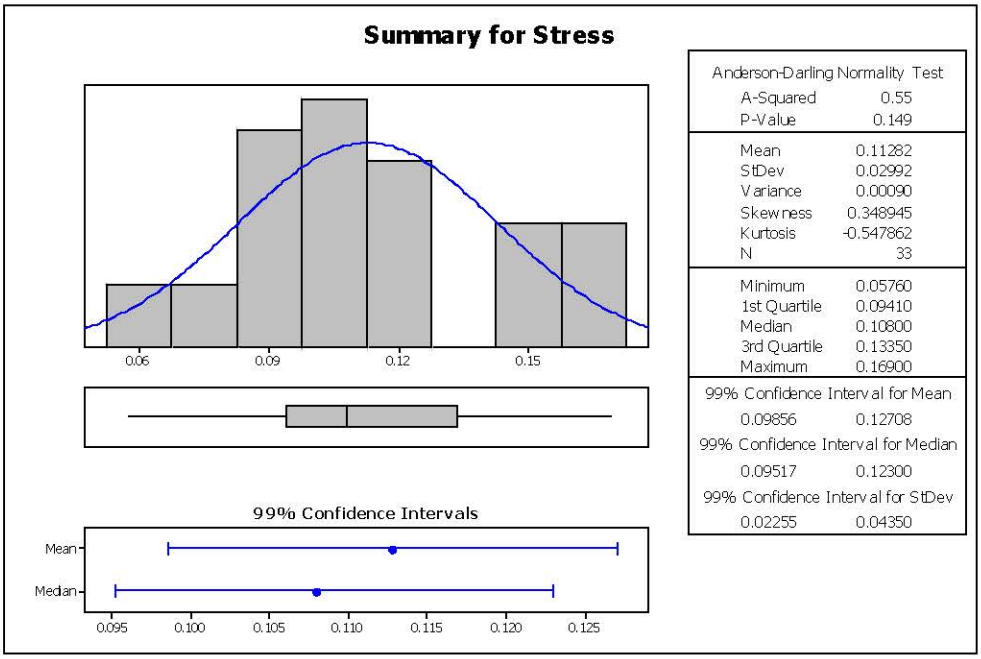

(a)

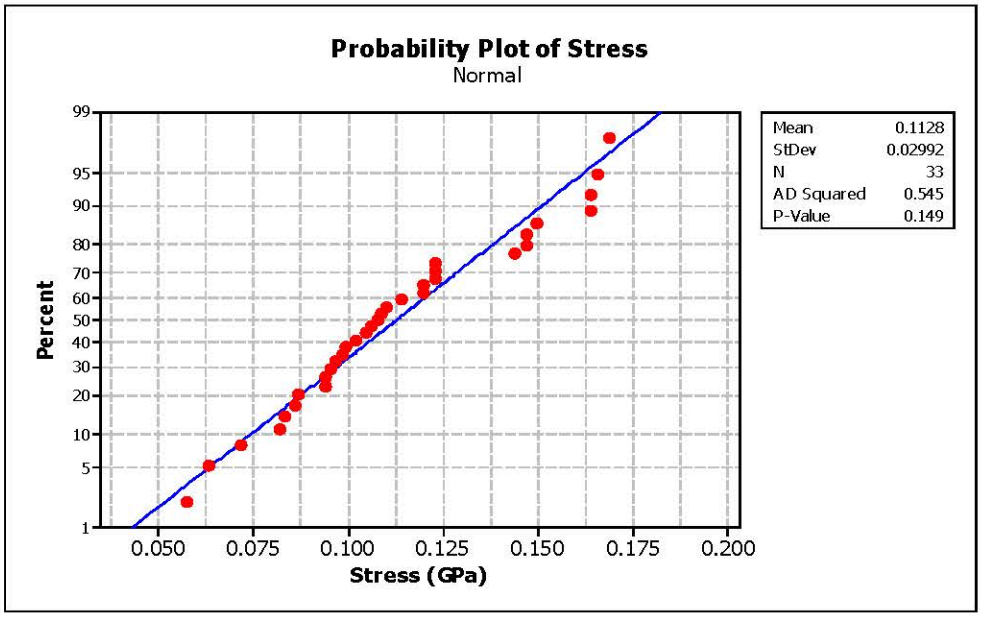

(b)

Figure 6.5. (a) The summary statistics for the generated stress values. (b) The normal probability plot for the generated stress values.

6.4.2 Interactions

The interactions plot, figure 6.6, shows the interaction effect of two factors on the response and compares the relative strength of the effects. The points are connected for the low and high level of the factor plotted on the x-axis, and this is for each combination of factors. The greater the angle between two lines greater the interaction between those factors.

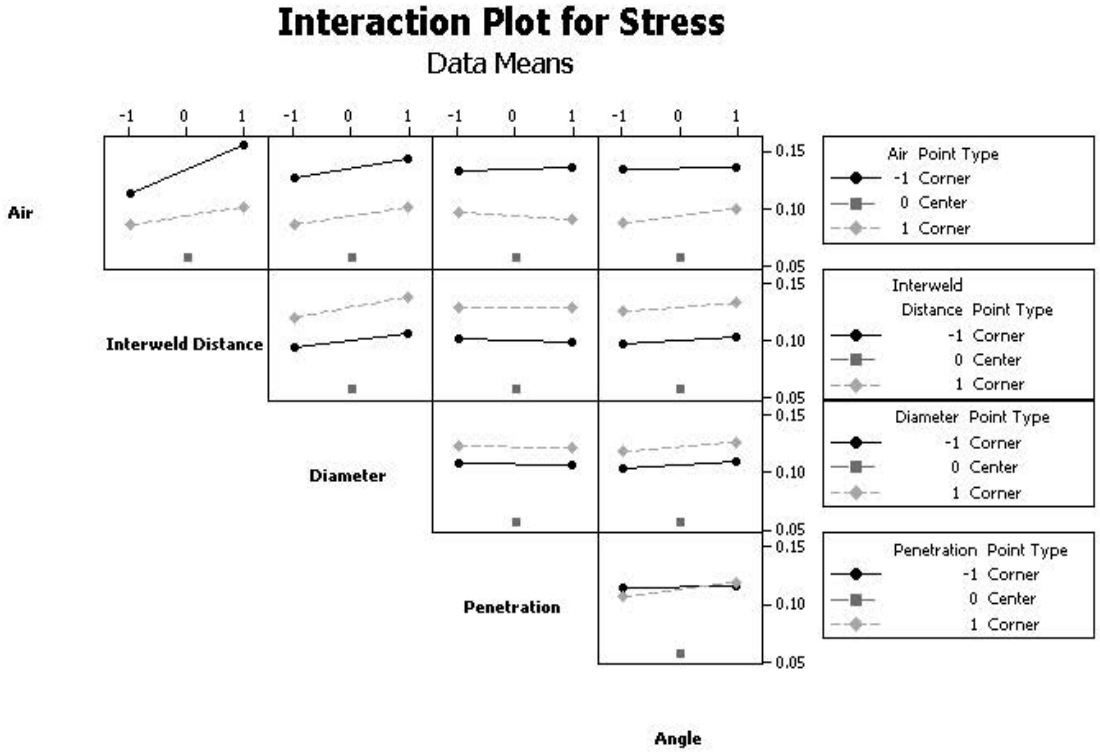

Figure 6.6. Interaction plot comparing two factors at a time.

An interaction is present when the change in the response mean from the low to the high level of a factor depends on the level of a second factor. If the lines are parallel to each other, there is no interaction present. This indicates the change in the response mean from the low to the high level of a factor does not depend on the level of a second factor.

If the lines are not parallel to each other, there is interaction present. The change in the response mean from the low to the high level of a factor depends on the level of a

second factor. The greater the degree of departure from being parallel, the stronger the effect.

From figure 6.6 the greatest interaction can be seen for the air gap and the interweld distance. The next strongest interaction is the air gap and angle. All the other interactions are not as strong as these. The penetration and the angle interaction is known as a cross-over interaction, since the lines cross over. This indicates that either one or both of the effects are not significant, even though there is an interaction effect. It is known from the discussion that follows that the angle has a greater significant effect than the penetration.

The advantage of using the interaction plot is that it gives a quick visual inspection of the factors that interact. As can be seen from the plot most of the factors have an interaction. How significant the interaction is and the direction of the interaction cannot be quantitatively gauged from the plot. The use of the normal effects plot gives this information and will be discussed in the next section.

6.4.3 Sensitivity Analysis

To investigate the sensitivity analysis and interactions, the normal effects plot and the Pareto chart of effects is used. To draw a normal effects plot the number of degrees of freedom for the error term determines how the plot is drawn. If there are one or more degrees of freedom then the normal scores (probabilities or percentages) can be plotted against the standardised effects. The reference line passes through the origin if normal scores are used. The reference line passes through 0.5 or 0 if probabilities or percentages are used. The reference line has a slope of one since this is where the points lie if all the effects are zero.

A sensitivity analysis is preformed to identify which effects should be included in the modelling process. The normal effects plot, figure 6.7, compares the relative magnitude of the main and interaction effects and also indicates their statistical significance. The reference line demarcates the effects that are significant and also shows the direction of the effects and interactions. All the points that lie to the right of the reference line indicate that the high factor setting results in a higher response than the lower setting.

All the points to the left of the reference line indicate that the lower factor setting results in a higher response than the high setting.

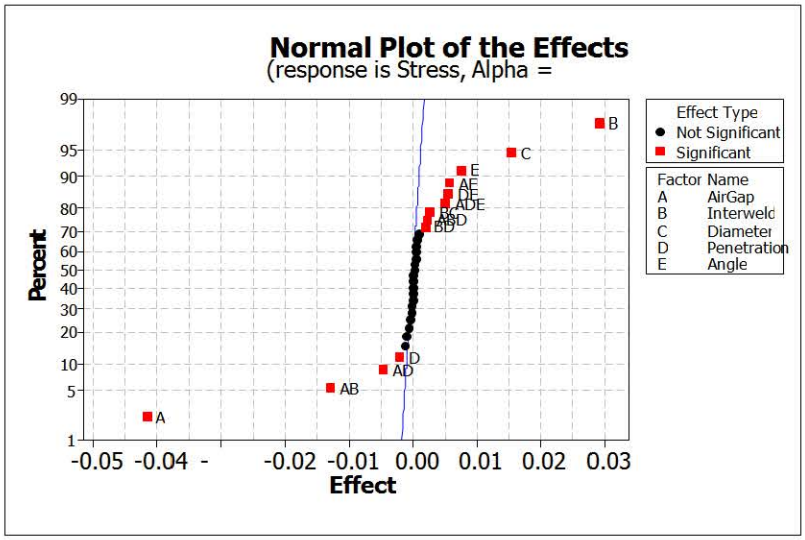

Figure 6.7. Normal effects plot.

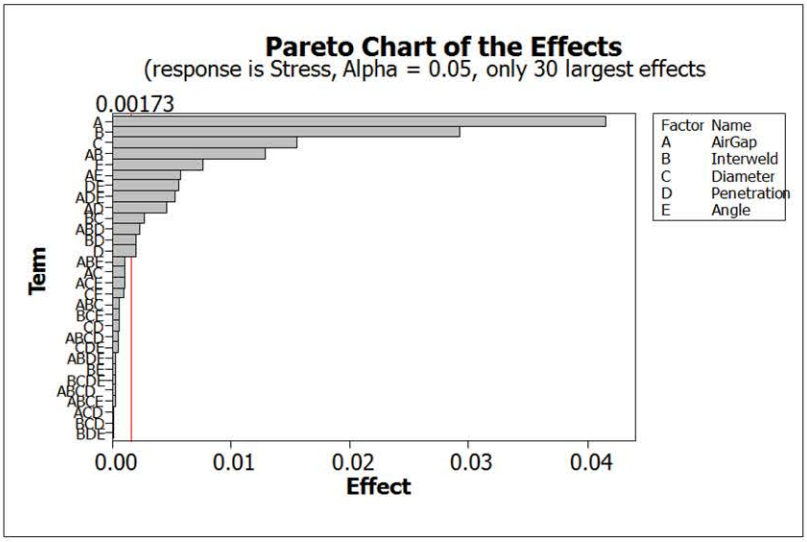

Figure 6.8. The Pareto chart of effects.

Where all the effects have been included, figure 6.7, there are a number of effects that appear not to be significant. There are no five and four factor interactions of any significance. This is to be expected, as four factor interactions and greater rarely occur (Box and Draper, 1987).

The Pareto chart of the effects can be used to help determine which effects are active. The Pareto chart uses the same alpha (α) as the normal plot to determine the significance of effects. The level of significance is also called the α (alpha) level. This is the probability of rejecting the null hypothesis when it is true, and is known as a type I error. The level of significance that was used in this work was at the level of 95%.

The Pareto chart compares the relative magnitude and the statistical significance of the main effects and the interaction effects. The plot shows in decreasing order the value of the absolute effects. The reference line demarcates the significant effects. It will show that the main effects and the interactions that are significant when α is at 0.05. The Pareto chart of the effects, figure 6.8, confirms the normal effects plot. The non-significant effects are not required in the model and are removed. A hierarchical model is needed to maintain the relationship between the main effects and the two and three factor interactions. Hence, only two and three factor interactions also included in the model.

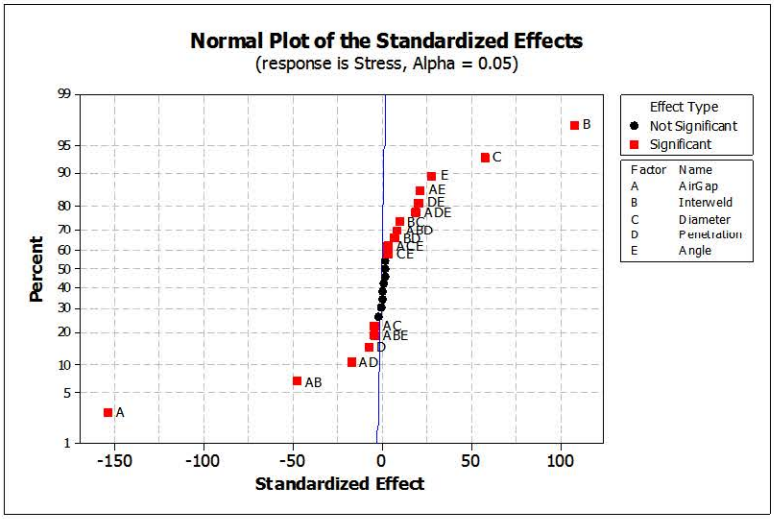

Figure 6.9. Normal plot of the standardised effects, with all four and five factor interaction removed.

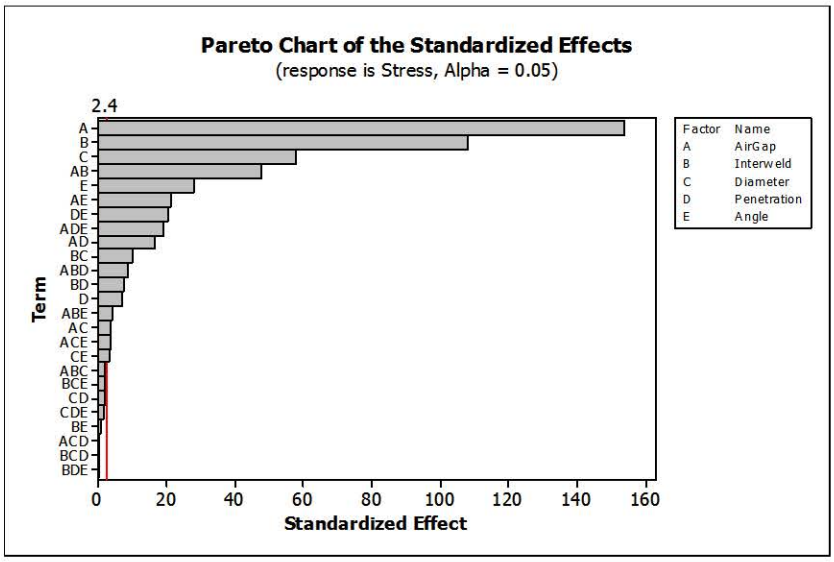

Figure 6.10. Pareto chart of the standardised effects, with all four and five factor interaction removed.

Figure 6.9 and figure 6.10 show that there are still some three factor interactions that are not significant. This process of checking the normal effects plot was repeated several times to identify non-significant effects and to remove them.

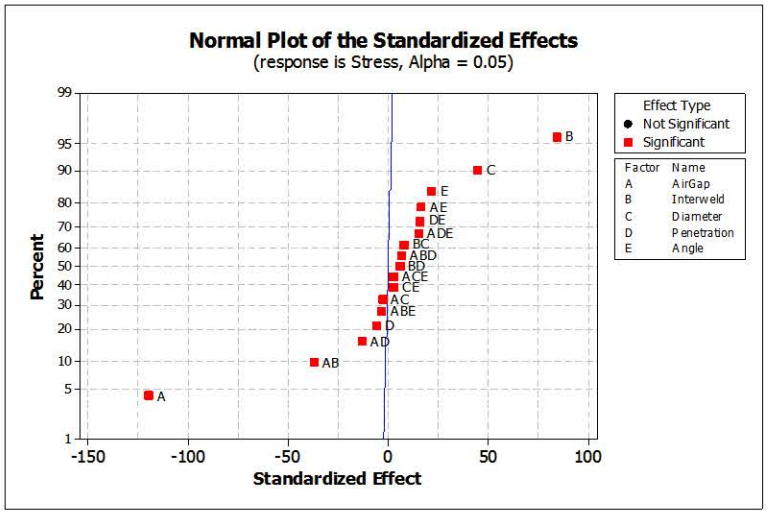

Figure 6.11. Normal plot of the standardised effects with non-significant effects removed.

The initial selection of effects and interactions to include in the model is based on figure 6.11 and figure 6.12. A number of effects are close to the reference line and will need to be investigated further and will depend on what other terms are included in the model. According to Daniel (1976), he estimated that for a two level design with four factors, gives on average four significant effects.

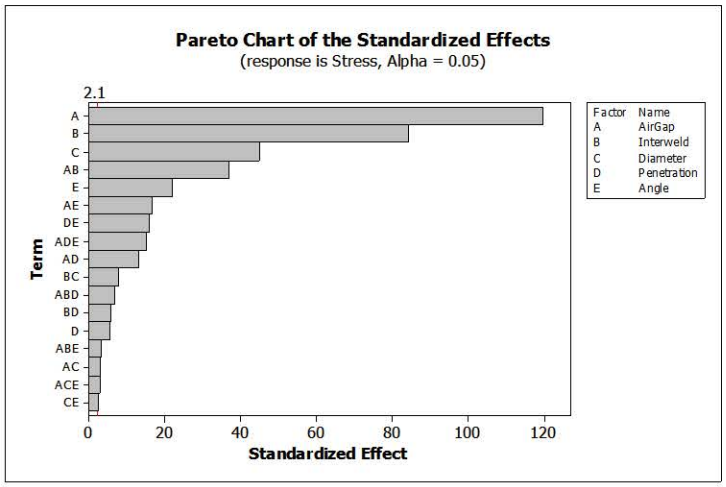

Figure 6.12. A Pareto chart showing the factors ordered from most significant to least significant.

So for a two level five factor design there should be about eight significant effects, almost twice as many as the 2^4 design. However, the number of significant effects will depend on how well the factors have been selected in the experiment. From the Pareto chart, figure 6.12, all the main effects are significant, hence for this design it appears that the factors have been reasonably well chosen.

The air gap appears to be the most significant effect, as the level changes from a low level to a high level of the factor the response decreases the most, as compared to any of the other factors. This indicates that the larger the air gap lowers the stress in the fibre. However, this factor by itself will not lower the stress in the fibre, as there are interaction effects that need to be taken into consideration.

The next most significant factor is the interweld distance, followed by the diameter of the weld spot and then the angle of the weld spot. For all three of these, as the factor

level increase from the lower setting of the factor the response increases. Hence, for all three of these factors the lower setting will produce a lower stress response in the fibre, but interaction effects have to be taken into consideration. The remaining factor, the penetration of the weld spot, is the closest item to the reference line, figure 6.11 and figure 6.12. It has some significance as it is not on the reference line. Its effect decreases the response at the higher level of the factor.

There are a number of two factor and three factor interactions shown on the plot which are significant. Most of the interaction effects are more significant than the penetration of the weld spot, but less significant than the other four remaining main effects. Interestingly the most significant two factor interaction is that of the air gap and interweld distance. This interaction comprises of the two main significant effects and as the interweld distances increases from a low level to a high level and the air gap distances increases from a high level to a low level the stress response decreases. From the plot in figure 6.11, it can be seen that individually the air gap at the high level decrease the stress response and the interweld distance at a high level increase the stress response. It appears the significance of this interaction is less than the significance of the air gap alone. This interaction reduces the effect of the air gap alone and reverses the effect of the interweld distance.

6.4.4 Significance of Two and Three Factor Interactions

Using the abbreviations from the Pareto chart in figure 6.12, there are two three factor interactions ABE and ACE, and two, two factor interactions AC and CE, which are borderline in terms of significance. It needs to be determined if they are significant when effects that were clearly not significant were not included in the model. To answer this question the coefficient of multiple determination needs to be examined.

The coefficient of multiple determination measures how close the data fits the regression line and is given by R^2. This is defined as the percentage of the response variable variation that can be explained by the model. Therefore, R^2 is a value between zero and one. Where a value of zero would indicate that the model does not explain any of the variability of the response data around the mean, and a value of one would explain all the variability. A higher R^2 value generally indicates a better fit of the data

for the model. However, there are issues with using the coefficient of multiple determination. If a model has many predictors a misleadingly high value is given for R^2, as it over fits the model. In fact as more predictors are added to the model the value of R^2 increases. To overcome these issues the adjusted-R^2 is used as it can be used to compare models with differing numbers of predictors.

To assess if the significance of the interactions ABE, ACE, AC and CE, six models were developed. The models differed in the combination of the interactions that were included, see table 6.3.

Table 6.3 shows the R^2 values, including the adjusted (*Adj-R2*) and the predicted (*Pr-R2*). During the analysis if the Pareto chart and the normal plot of the standardised effects showed any effects that were not significant they were recorded in the column marked *not significant*. The R^2 values, which is not of interest, generally decreases if an effect is removed.

Table 6.3. The coefficient of multiple determination for the adjusted and predicted values.

Model	Factors				R2	Adj-R2	Pr-R2	Not Significant
1	ABE	ACE	AC	CE	99.95	99.88	99.72	
2	0	ACE	AC	CE	99.91	99.81	99.58	CE
3	ABE	0	AC	CE	99.91	99.81	99.58	CE
4	ABE	ACE	0	CE	99.91	99.82	99.61	CE
5	ABE	ACE	AC	0	99.92	99.84	99.65	
6	0	0	0	0	99.82	99.69	99.43	

The *Adj-R2* values allow comparison of the six models that were generated, see table 6.3. With the effects ABE, ACE, AC and CE remaining in the model gives the highest value for the *Adj-R2*. The other five models gave a lowered value, indicating that these effects are significant and should not be removed from the model. The Pareto chart and the normal plot of the standardised effects for models two, three and four indicate that CE is insignificant. In model five CE is removed but this does not improve the *Adj-R2* value compared to model one.

To estimate how well a regression model can predict responses for a new observation, the predicted R^2 (*Pr-R2*) is used, see table 6.3. The *Pr-R2* values are calculated by removing each data point and estimating the model and then determining how well the model will predict the removed data point. This indicates that the model fits the data better with all three interactions included.

6.4.5 Estimating the Effects and Coefficients

The results from the design of experiments modelling process are summarised in table 6.4 for the model that was selected to be used. The effects column represents the response when there is a change in the factor from a high level to a low level. The higher the absolute value of an effect the greater the effect of the response. The sign of the effect shows which factor setting has a higher response.

Table 6.4. Summary of the estimated effects and coefficients for stress using coded units.

Term	Effect	Coef	SE Coef	t	p
Constant	0.11455	0.000174	660	0	0.000
Air Gap	-0.04153	-0.02077	0.000174	-119.65	0.000
Interweld Distance	0.02926	0.01463	0.000174	84.29	0.000
Diameter	0.01561	0.0078	0.000174	44.96	0.000
Penetration	-0.00194	-0.00097	0.000174	-5.6	0.000
Angle	0.00763	0.00382	0.000174	21.99	0.000
Air Gap * Interweld Distance	-0.01287	-0.00643	0.000174	-37.07	0.000
Air Gap * Diameter	-0.00102	-0.00051	0.000174	-2.93	0.011
Air Gap * Penetration	-0.00457	-0.00228	0.000174	-13.16	0.000
Air Gap * Angle	0.00576	0.00288	0.000174	16.58	0.000
Interweld Distance * Diameter	0.00269	0.00135	0.000174	7.76	0.000
Interweld Distance * Penetration	0.00199	0.001	0.000174	5.74	0.000
Diameter * Angle	0.00089	0.00045	0.000174	2.57	0.022
Penetration * Angle	0.00559	0.0028	0.000174	16.12	0.000
Air Gap * Interweld Distance * Penetration	0.00237	0.00118	0.000174	6.82	0.000
Air Gap * Interweld Distance * Angle	-0.00111	-0.00055	0.000174	-3.19	0.007
Air Gap * Diameter*Angle	0.00102	0.00051	0.000174	2.93	0.011
Air Gap * Penetration * Angle	0.00522	0.00261	0.000174	15.03	0.000

α = 0.05 R-Sq = 99.95% R-Sq(pred) = 99.72% R-Sq(adj) = 99.88%

A negative sign in front of an effect indicates a higher response from a low factor setting than a high factor setting. A positive sign indicates a higher response from a high factor setting than a low factor setting.

The estimated effects for each factor are calculated as:

$$effect = 2 * coefficient \quad \textbf{6.6}$$

Dividing the estimated regression coefficients by its standard error gives the t-statistic, which is used to estimate the p value. The p value is the probability of the coefficient occurring, if the real value in the population is zero. The p value is used to determine the significance of rejecting the null hypothesis. The p value ranges from zero to one. If the p value is less than the chosen value of α, the null hypothesis is rejected. The null hypothesis states that the coefficient is zero, whilst the alternative hypothesis states that it is not equal to zero.

The p values (table 6.4), were generated from the test statistic to give an indication if the result are statistically significant. It is apparent that all the effects are significant, since α = 0.05 and $p < 0.05$, for both main and interaction effects. These effects were retained in the model.

6.4.6 Analysis of Variance

A number of estimates have been made in table 6.4 regarding the model, this begs the questions how good are those estimates? The answer to this question can be gained from the analysis of variance, table 6.5. Here, the p-value can indicate whether a significant prediction can be made. All the p-values are very low (zero) and are less than α, hence the sources are highly significant. It can be concurred that they did not occur due to chance alone.

Table 6.5 also shows the sequential sum of squares (*Seq SS*) and the adjusted sum of squares (*Adj SS*). The values of both these columns are the same, which is to be expected as the design is orthogonal and does not contain covariates.

Table 6.5. Summary of the analysis of variance for stress (coded units)

Source	DF	Seq SS	Adj SS	Adj MS	F	p
Main Effects	5	0.02309	0.023090	0.00461815	1796.14	0.000
2-Way Interactions	6	0.00209	0.002097	0.00034951	135.94	0.000
3-Way Interactions	2	0.00026	0.000262	0.00013139	51.10	0.000
Residual Error	18	0.00004	0.000046	0.00000257		
Total	31	0.02549				

6.4.7 Influence Diagnostic Tools

The resultant coefficients of the model have been identified, but before the model can be used a search is made for any unusual observations. The statistical tools that can be used to find such unusual observations included Cook's distance and DFFITS. These tools are well established within regression analysis. The results for the selected model are shown in table 6.6.

Table 6.6. Cook's distance and DFFITS for the selected model.

DFIT	DFIT	COOK'S D	COOK'S D
0.046686	0.000324	-0.70473	-0.07363
0.106718	0.000238	-0.41308	0.0631
0.008575	0.000324	-0.38022	0.07363
0.031501	0.005955	-0.73732	-0.31643
0.029702	0.003811	0.11529	0.125287
0.25418	0.037218	0.13867	-0.80381
0.018586	0.003811	0.1261	-0.25287
0	0.064848	0	0.0766
0.003811	0.029702	-0.25287	-0.71529
0.135301	0.139383	0.11719	-1.3462
0.1372	0.029702	0.13029	0.11529
0.018586	0.122379	0.1261	-0.52667
0.106718	0.008575	0.11308	-0.38022
0.105044	0.127289	-0.40065	-0.09062
0.103667	0.008575	-0.36365	0.138022
0.032421	0.144886	-0.74836	0.125022

For Cooks distance a score of larger than $4/(n-p-1)$ will indicate an observation that is an outlier. Here p is the number of predictors in the model and n the number of observations. For the selected model a value of 0.1538 or larger will indicate an outlier. No outliers are indicated in table 6.6. For the DFFITS, an absolute value greater than $2\sqrt{p/n}$ will indicate a value that is influential and will need investigating. For the selected model the value is 0.7906 or larger. No such influential points can be identified in table 6.6.

6.4.8 Residual Plots

The analysis of the DoE data involves checking the data for any trends or if any anomalies can be identified. Inspection of the residuals is an initial starting point. The difference between the observed values and the fitted or predicted values is known as the residuals, and is given in equation 6.15.

$$e_i = (y_i - \hat{y}_i) \qquad \textbf{6.15}$$

Where the residual is given by e_i, y_i is the observed value and $\hat{y}_i$ is the predicted value. The residual plots for the selected model are shown in figure 6.13. The examinations of the residuals will help to determine if the ordinary least squares assumptions are being satisfied. If they are satisfied then the ordinary least squares regression will have produced unbiased coefficient estimates with the minimum variance.

(a)

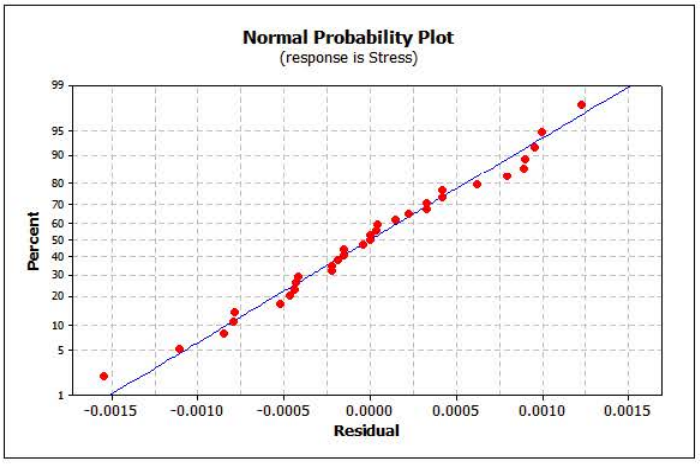

(b)

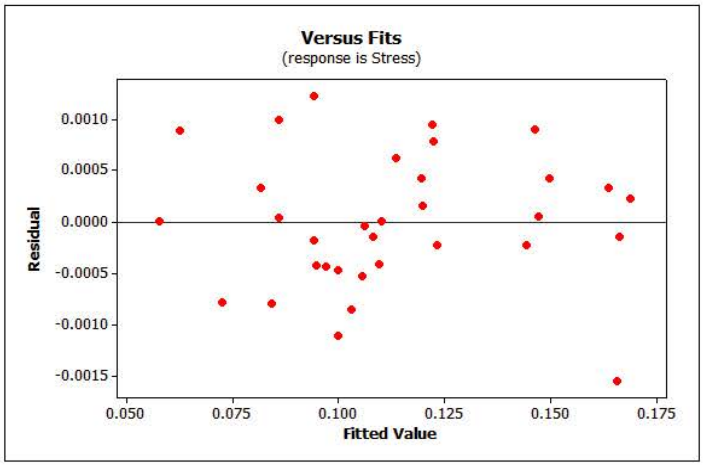

(c)

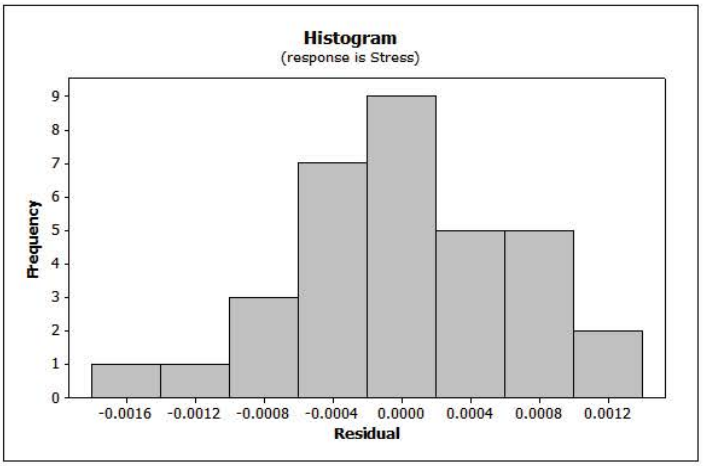

Figure 6.13 The residual plots, consisting of (a) normal, (b) fits, (c) histogram

The normal probability plot, figure 6.13a, is a plot of the residuals against their expected values when the distribution is normal. Generally the points on the plot should approximately follow the superimposed reference line. All the points appear to be following the straight line, which indicates that the data is normally distributed and that the design is balanced.

The residuals against the fitted values are used to check for a non-constant variance, missing terms or outliers. The residuals should be scattered randomly about zero. According to this plot, figure 6.13(b), the residuals are all scattered randomly about zero. This indicates that the assumption of constant variance is fulfilled and visually no missing terms or outliers exist.

The histogram of the residuals, figure 6.13(c), shows the spread or variation of the distribution and any unusual data regarding the fibre stress values which may exist, such as outliers or if the data is skewed. No such data is found in the analysis; the histogram appears to be approximately symmetrical following a bell shape.

6.5 The Surrogate Model

There is a coefficient for each term in the surrogate model. These coefficients are used to construct the polynomial equation representing the relationship between the response, the stress in the fibre, and the five design points. The polynomial for the von Mises stress in the fibre optic is given by equation 6.16. The model in equation 6.16 can be used to predict stress in units of GPa and the arguments are the values of the five design variables in uncoded values.

The empirical surrogate model that has been estimated is a multiple linear regression model and is based on the results in table 6.4. This model is a first order linear polynomial model with interactions, equation 6.16.

$$\begin{aligned} Stress = {} & \beta_0 + \beta_1 x_1 + \beta_2 x_2 + \beta_3 x_3 + \beta_4 x_4 + \beta_5 x_5 + \beta_{12} x_1 x_2 + \beta_{13} x_1 x_3 \\ & + \beta_{14} x_1 x_4 + \beta_{15} x_1 x_5 + \beta_{23} x_2 x_3 + \beta_{24} x_2 x_4 + \beta_{35} x_3 x_5 \\ & + \beta_{45} x_4 x_5 + \beta_{124} x_1 x_2 x_4 + \beta_{125} x_1 x_2 x_5 + \beta_{135} x_1 x_3 x_5 \\ & + \beta_{145} x_1 x_4 x_5 \end{aligned} \qquad \textbf{6.16}$$

Where:

$x_1 = AirGap$	$\beta_3 = 0.0078$	$\beta_{24} = 0.001$
$x_2 = Interweld$	$\beta_4 = -0.00097$	$\beta_{35} = 0.00045$
$x_3 = Diameter$	$\beta_5 = 0.00382$	$\beta_{45} = 0.0028$
$x_4 = Penetration$	$\beta_{12} = -0.00643$	$\beta_{124} = 0.00118$
$x_5 = Angle$	$\beta_{13} = -0.00051$	$\beta_{125} = -0.00055$
$\beta_0 = 0.000174$	$\beta_{14} = -0.00228$	$\beta_{135} = 0.00051$
$\beta_1 = -0.02077$	$\beta_{15} = 0.00288$	$\beta_{145} = 0.00261$
$\beta_2 = 0.01463$	$\beta_{23} = 0.00135$	

6.6 Conclusion

In some systems the exact relationship between the inputs and the outputs may be known which gives a mechanistic model. For the stress generated in the optical fibre due to laser micro welding, the underlying relationships are unknown. In such a situation design of experiments was conducted to approximate an appropriate empirical model. This empirical model is known as the surrogate model. This chapter has fulfilled the seventh objective of developing a surrogate model.

The five key variables, informed by the engineering team at Oclaro, were used in a design of experiment. This was used to evaluate the post welding stresses in the fibre optic of the numerical model using finite element analysis. A full factorial design of experiments consisting of the five factors at two levels was conducted to identify the surrogate model. Such two level designs in general are useful, and have three specific applications. Firstly they can be used in screening experiments to identify the important process variables out of many possible process variables. Next they can be used to fit first order surrogate models and can be used for the steepest ascent/descent method. Finally they can be used as the basis for creating other surrogate models. In this chapter the DoE was used identify the important process variables. The other uses will be specifically investigated in the next chapter.

This chapter has shown that a number of sequential steps are required to produce the surrogate model. The first step being to ensure that the data is normally distributed. In fact all the other steps hinge on this step, as they require the data to be normally distributed. The second step was iterative and needed several rounds to identify the significant factors and interactions as part of the sensitivity analysis. Once these were identified a number of statistical techniques were used to validate the initial model as being significant and not being due to chance. The final step was the model adequacy checking by analysing the residual plots. This has two specific purposes. To ensure that the selected model adequately approximates the true system, and to verify that the least squares regression assumptions were not violated.

Chapter 7

Uncertainty Analysis

This chapter covers the penultimate objectives, which are to:

- Perform the risk analysis.
- Improve the process inputs that minimise the stress in the optical fibre.
- Discover the capability of the process.

A surrogate model is used to investigate these objectives.

The main steps of the OPISA methodology are illustrated in figure 7.1. Part of the methodology has been demonstrated in the previous chapter. The remainder of the methodology will be demonstrated in this chapter.

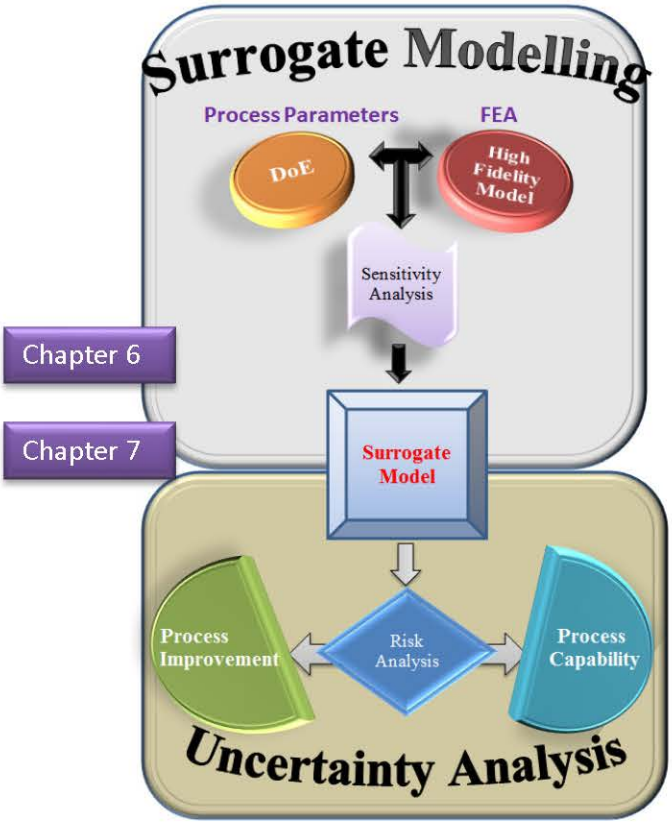

Figure 7.1. An overview of the OPISA methodology.

In the previous chapter a number of models were assessed to identify the key process parameters. From this a surrogate model has been constructed using a least squares method to build a first order polynomial linear with interactions function. The surrogate modelling process from the previous chapter will now be used to:

- Assess the risk analysis of the manufacturing tolerances of the design variables using Monte Carlo simulations.
- To improve the process, by using a novel Monte Carlo simulation with the steepest ascent optimisation algorithm which is part of the response surface methodology (Box and Draper, 2007). This is used to undertake design optimisation and to determine the optimal process parameters.
- Evaluate the capability of the welding process.

7.1 Risk Analysis

The definition of risk in this context is the probability of the occurrence of the magnitude of stress within a specified range. To assess the risk the surrogate model in equation 6.16 is used with a Monte Carlo simulation using Crystal Ball (Oracle n.d). This will allow the determination of the fibre stress variation when uncertainty and variation of the design variables are accounted for. Table 7.1 shows the type of distribution used, the estimated mean and the estimated standard deviations for each of the five design variables associated with a nominal package design for which the risk analysis is undertaken.

Table 7.1. The mean values, the estimated standard deviation and the distribution type used for the Monte Carlo simulation.

Factor	Name	Mean	Std Dev	High	Low	Dist.
1	Air Gap (µm)	10	3.3333	20	0	*Normal*
2	Interweld distance mm)	2.85	0.6167	4.7	1	*Normal*
3	Weld diameter (mm)	0.65	0.0167	0.7	0.6	*Normal*
4	Weld penetration (µm)	630	3.3333	640	620	*Normal*
5	Laser angle (Degrees)	32.5	0.8333	35	30	*Normal*

Ordinarily the magnitude of the mean and the standard deviation for the process variables is determined from the manufacturing process. Since there was no access to the fibre capsule components or the laser welding set up the mean and the standard deviation were estimated. It is assumed that the component measurements and the laser machine settings follow a normal distribution. A Monte Carlo simulation can be used to estimate the mean and standard deviation. Otherwise, the properties of the normal distribution can be used to estimate the mean and standard deviation, as done in this case. In a normal population 99.73% of the observations will be found within six standard deviations of the mean. The estimated standard deviation can be found from:

$$standard\ deviation\ estimate = \frac{largest\ possible\ value - smallest\ posible\ value}{6} \qquad \mathbf{7.1}$$

The Oclaro optical package has a range within which displacement of the optical fibre is acceptable as it causes no undue decrease in efficiency. With this in mind, to assess the risk of the process using six sigma methodologies a lower specification limit (LSL) of 0.0616 GPa of stress in the fibre and an upper limit (USL) of 0.1128 GPa for maximum stress in fibre are chosen arbitrarily to demonstrate the technique. A Monte Carlo simulation is run for five million trials. This Monte Carlo simulation is based on fibre stress evaluations from the surrogate model, which are fast and can accommodate such a large number of evaluations in a reasonable computational time. To run this simulation Crystal Ball (Oracle n.d), was used.

The Monte Carlo simulation uses the mean and standard deviation of each process variable to generate a random number that comes from a normal distribution to represent that process variable. This is repeated for each process variable, see figure 7.2.

Once a set of values has been generated for the five process variables they are passed into the surrogate model to obtain a stress value. This will represent a single iteration of the Monte Carlo simulation. This process is iterated as specified, and at each iteration the stress value and its frequency is noted.

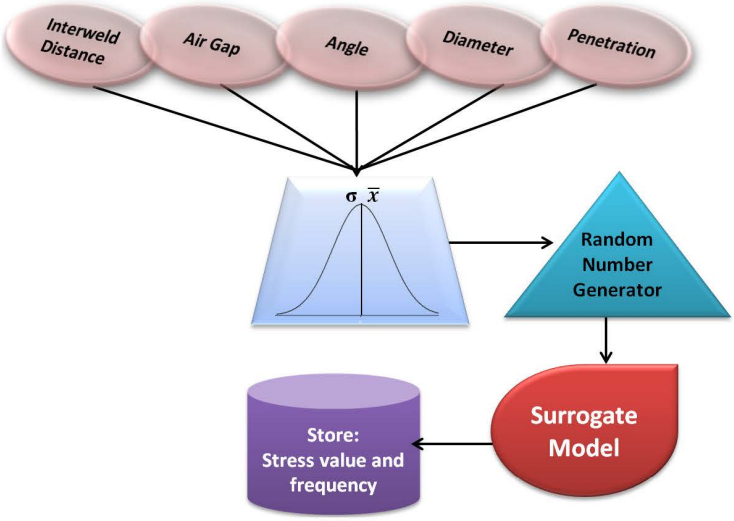

Figure 7.2. The Monte Carlo algorithm.

The predicted fibre stress response values are now used to understand how the uncertainties of the input design variables propagate into uncertainty and variation of fibre stress. The result of the Monte Carlo simulation is shown in figure 7.3.

The risk analysis, figure 7.3, shows that within the specified parameters, as given in table 7.1, only 36% of the parts fall into the range where the stress in the optical fibre is between 0.0616 GPa and 0.1128 GPa. It should be noted that the distribution produced as a result of the risk analysis is non-normal.

7.2 Process and Design Improvement

To improve or to optimise the process a response surface is created of the process. The surrogate model building procedure is used to create a model that can represent the true response surface. This model can be used to first establish the region in which the process is currently working. From here the model can be used to find a new region in which the process can be improved. The steepest path technique is used, which is a first order gradient based optimisation technique and works best when the process is far from the optimum (Myers et al., 2009).

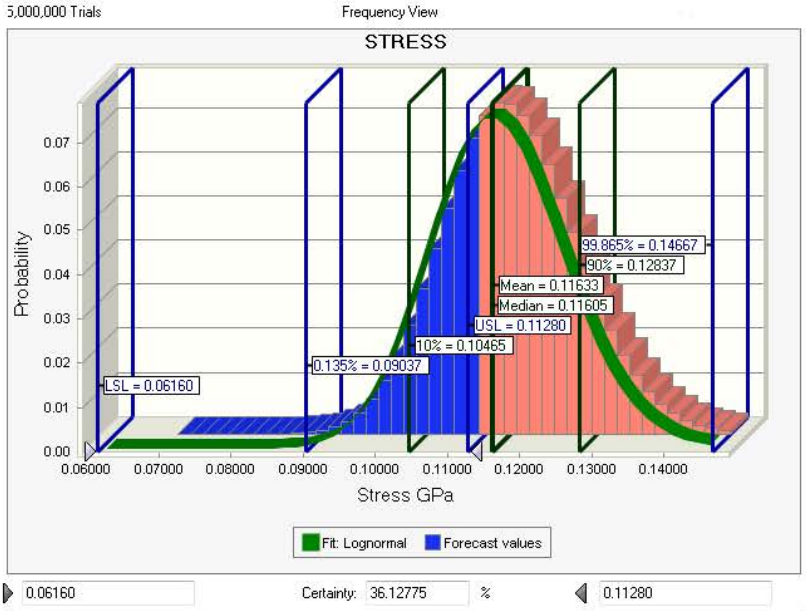

(a) Frequency Histogram

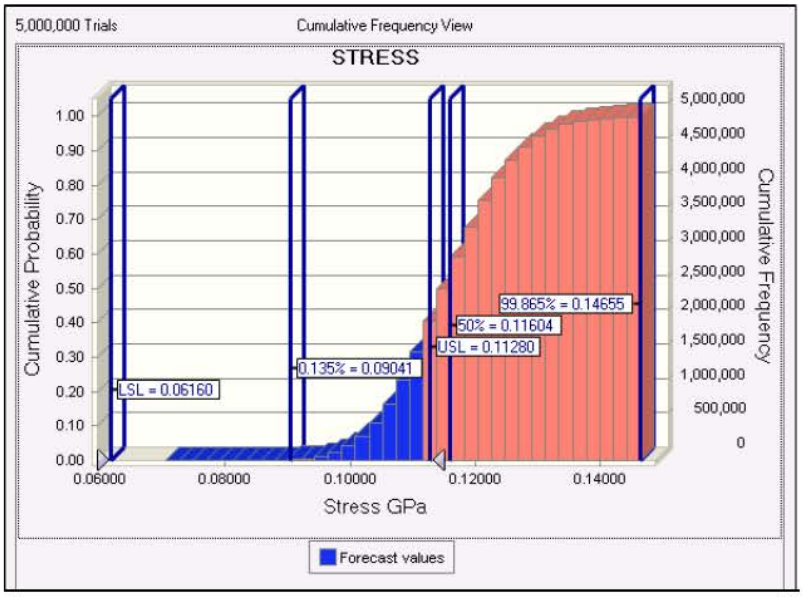

(b) Cumulative Frequency Histogram

Figure 7.3. (a) and (b) Five million trial Monte Carlo simulation showing risk of the process. The percentiles are also shown.

7.2.1 Model Checking

To use a surrogate model for the response surface, a first order polynomial function can be used. If the function has no interactions, this will give a hyperplane, with no curvature effects to worry about. However, the model developed in the previous chapter, equation 6.16 has a number of two and three factor interactions. The interaction terms that include the three factor interactions are strongly represented. A response surface from such a model would create a highly curved surface which will give poor results to locate the improvement of the process. To overcome the problems of curvature a new model has to be developed from the DoE data.

From the data of the DoE, a surrogate model is developed that has no two and three factor interactions. The coefficient of determination, R^2, is measured by using the regressor variables to obtain the reduction in the variability of the stress. This value was found for the model. From figure 7.4, a respectable value is shown for R^2.

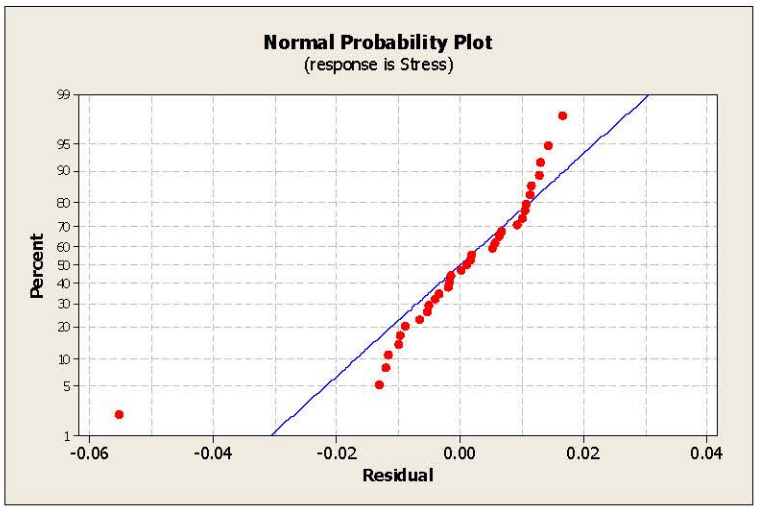

Figure 7.4 Normal probability residual plot and R^2 values for the main effects surrogate model.

However, the normal probability plot, figure 7.4, for the residuals shows a marked departure from normality, indicating a poor model, and it indicates that the least squares

regression assumptions are violated. Iteratively a number of surrogate models were produced using the same procedure as demonstrated in the previous chapter.

The final model that was selected was a first order polynomial the non-significant terms removed and the main effects and only the two factor interactions included, see figure 7.5.

The R^2 has significantly improved, figure 7.5(a). The residual plots, figure 7.5(a), (b) and (c) show that the model provides an adequate fit, with none of the assumption being violated.

R^2 = 98.44%
R^2 (pred) = 96.69%
R^2 (adj) = 97.80%

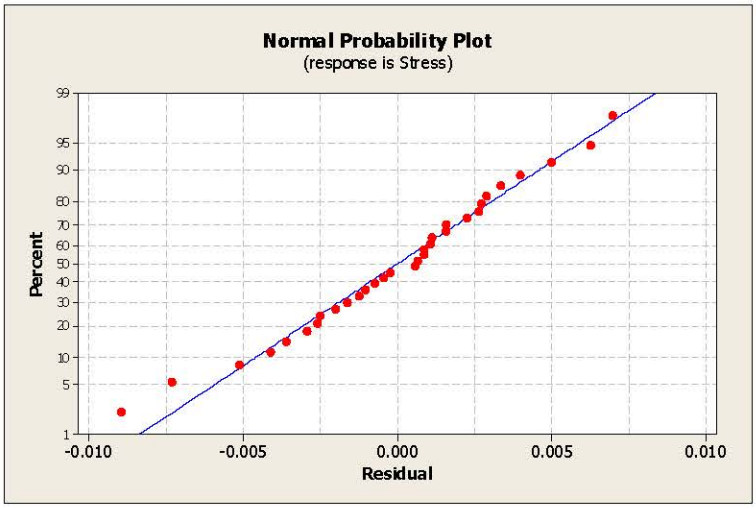

(a) Normal probability plot

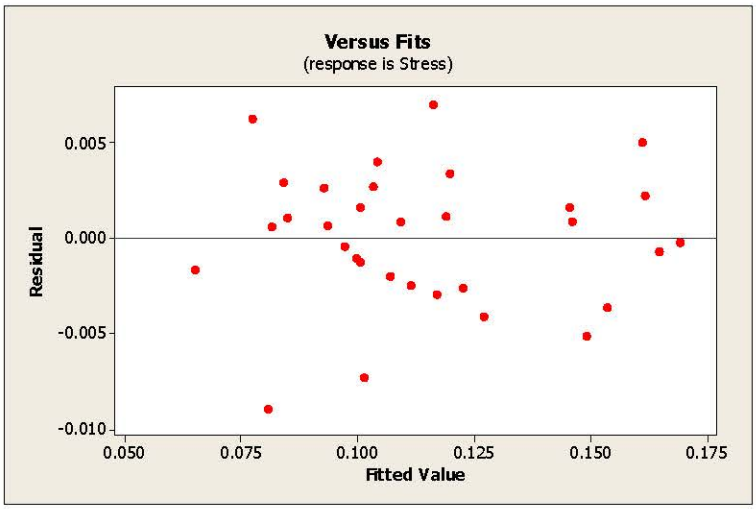

(b) Fits plot

(c) Histogram

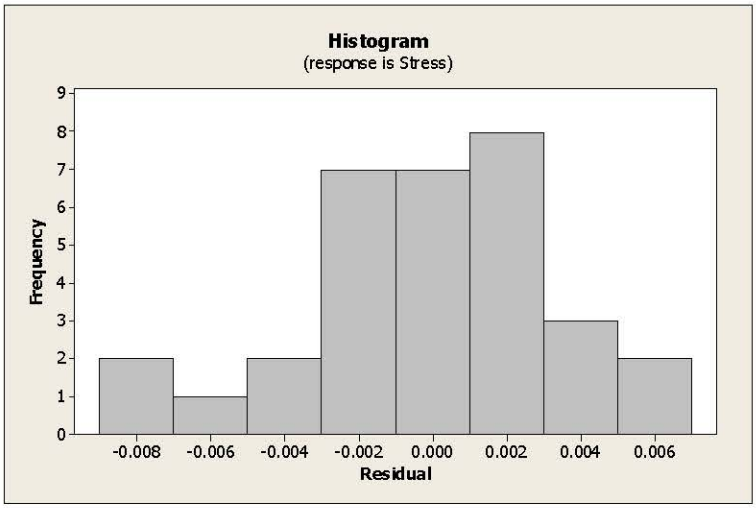

Figure 7.5. The residual plots for the selected first order model of the response surface.

Occasionally a disproportionate influence on the fitted regression model can come from a small subset of the data. This can be can be checked by inspecting DFFITS and Cook's distance, see table 7.2.

Table 7.2. Cooks distance and the DFIT values for the model developed in equation 7.2.

COOKS D	COOKS D	DFIT	DFIT
0.0955	0.0027	-0.0041	0.1611
0.0478	0.0007	-0.6919	-0.0805
0.0256	0.0012	0.5008	0.1073
0.0016	0.0303	0.1249	0.5459
0.0145	0.1480	-0.3747	0.4379
0.0613	0.0271	-0.7895	0.5154
0.0909	0.0041	0.9771	0.1986
0.0414	0.1427	0.6419	0.2606
0.0026	0.0184	0.1588	0.4225
0.1417	0.1456	-0.6826	-0.5237
0.0576	0.0098	0.7639	-0.3070
0.0093	0.0246	0.2999	-0.4912
0.0313	0.0002	-0.5556	-0.0420
0.0056	0.0019	-0.2327	-0.1354
0.0093	0.0038	0.2987	-0.1916
0.0227	0.0046	-0.4706	0.2092

For Cooks distance a score of larger than $4/(n-p-1)$ will indicate an observation that is an outlier. Here p is the number of predictors in the model and n the number of observations. For the selected model a value of 0.1538 will indicate an outlier. No outliers are indicated in table 6.6. For the DFFITS, an absolute value greater than $2\sqrt{p/n}$ will indicate a value that is influential and will need investigating. For the selected model the value is 0.7906. No such influential points can be identified in table 6.6. For the selected model no unduly influential points or outliers were found.

The final model, using the estimated regression coefficients for stress in uncoded units is shown in equation 7.2. It was selected with the non-significant terms having been removed and was used to construct a response surface figure 7.6.

$$Stress = \beta_0 + \beta_1 x_1 + \beta_2 x_2 + \beta_3 x_3 + \beta_4 x_4 + \beta_5 x_5 + \beta_{12} x_1 x_2 + \beta_{14} x_1 x_4 + \beta_{15} x_1 x_5 + \beta_{45} x_4 x_5 \quad \textbf{7.2}$$

Where:

$x_1 = Air\ Gap,\ x_2 = Interweld\ Distance,\ x_3 = Diameter,\ x_4 = Penetration,$
$x_5 = Angle,\ \beta_0 = 0.114547,\ \beta_1 = -0.0207656,\ \beta_2 = 0.0146281,$
$\beta_3 = 0.00780312,\ \beta_4 = -9.71875E-04,\ \beta_5 = 0.00381563,$
$\beta_{12} = -0.00643437, \beta_{14} = -0.0022843,\ \beta_{15} = 0.00287813, \beta_{45} = 0.0027968$

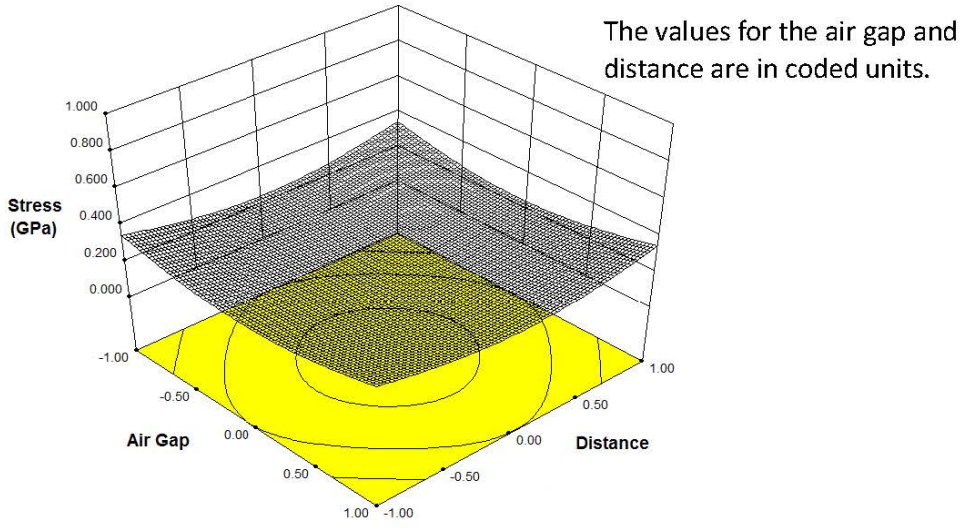

Figure 7.6. Surface plot between the air gap and distance between the weld spots for the stress.

The three dimensional plot shown in figure 7.6, gives a twisted plane for the response surface, this is due to the contour lines not being parallel because of curvature. When including interactions, especially if they are strong, curvature is found in the approximating model and observed as twisting in the response plane.

7.3 The Steepest Path Search

If the process involves maximising a response the steepest ascent is used which will result in computing a path that will maximise the response. If the process involves minimising a response then the steepest descent is used, which will result in computing a path that will minimise the response. The response of interest is to find values for the factors which will reduce the stress, so the path of steepest descent will be sought. The steepest path search is also known as hill climbing search and is referred to as a greedy search because it grabs the next good neighbour. As such it makes good progress towards finding a solution.

7.3.1 The Path of Steepest Descent

This is a sequential procedure which searches for the region of process improvement where the response, the stress in the optical fibre, is minimised. The technique involves moving from the current region to a region of improvement using a sequence of experiments. Because it requires a number of experiments to be performed, design economy and simplicity are of importance (Montgomery 2012). The technique is well established and is a textbook process that is well documented by a number of researchers in the field (Myers et al., 2009, Box et al., 2009, Montgomery 2012).

The technique requires starting from the centre of the experiment; this is where each factor is at zero in coded form. Experimental runs are then conducted to find another path of steepest descent. The process will show the response improving. The process is stopped once there is a decline in the response. The decline in the response is due to the deterioration in the first order model. For the purposes of demonstrating the response surface technique, instead of running a series of experiments the model in equation 7.2 was used to identify the response along the path of steepest descent.

To compute the path of steepest descent is, see section 3.3, a step size is chosen in one of the factors, usually the factor that has the largest absolute regression coefficient (Montgomery 2012). From equation 7.2, the air gap has the largest absolute regression coefficient. The step size has to be chosen with care. If the step size is too large it will overshoot the region of improved response. If the step size is too small it will show very slow improvement in the response, which can become overlooked. This indicates that the value of the step size is sensitive and needs to be carefully chosen. The values chosen here for the step size were on a trial basis.

From table 7.3, only two feasible experiments gave reduced stress values, during step one and two. However, the reduction in stress is higher than the values already obtained from the factorial experiments. This could be indicative that the current process is near the optimum, where curvature is more prevalent and interactions between the factors are important.

Table 7.3. The path of steepest descent computed for a step size of -0.46 using the air gap.

	Coded Units				Engineering Units			
	Step				Step			
Factor	1	2	3	4	1	2	3	4
Air Gap (µm)	-0.46	-0.92	-1.38	-1.84	5.36	0.72	-3.92	-8.56
Interweld distance (mm)	0.327	0.654	0.981	1.307	3.654	4.307	4.961	5.615
Weld diameter (mm)	0.174	0.349	0.523	0.697	0.517	0.535	0.552	0.57
Weld penetration (µm)	-0.02	-0.04	-0.07	-0.09	39.78	39.57	39.35	39.49
Laser angle	0.085	0.171	0.256	0.341	30.43	30.85	31.28	31.71
Stress (GPa)	-	-	-	-	0.097	0.079	0.062	0.044

There is a possibility that maybe an inappropriate step size was chosen and possibly that is why poor reduction values for the stress were achieved. To check for this another two step sizes were tested, see tables 7.4. Once again poor improvement was seen, and could be indicative of the process being close to the optimum.

Tables 7.4. The path of steepest descent computed for a step size of -0.90 (upper table) and -0.20 (lower table) for the air gap.

	Coded Units				Engineering Units			
	Step				Step			
Factor	1	2	3	4	1	2	3	4
Air Gap (µm)	-0.90	-1.8	-2.7	-3.6	1	-8	-17	-26
Interweld distance (mm)	0.634	1.268	1.902	2.536	4.268	5.536	6.804	8.072
Weld diameter (mm)	0.338	0.676	1.015	1.353	0.534	0.568	0.601	0.635
Weld penetration (µm)	-0.04	-0.08	-0.13	-0.17	39.58	39.16	38.74	39.01
Laser angle (Degrees)	0.165	0.331	0.496	0.661	30.83	31.65	32.48	33.31
Stress (GPa)	-	-	-	-	0.081	0.047	0.013	-0.02

	Coded Units				Engineering Units			
	Step				Step			
Factor	1	2	3	4	1	2	3	4
Air Gap (µm)	-0.020	-0.040	-0.060	-0.080	-0.160	-0.180	-0.200	-0.220
Interweld distance (mm)	-0.014	-0.028	-0.042	-0.056	-0.113	-0.127	-0.141	-0.155
Weld diameter(mm)	-0.008	-0.015	-0.023	-0.030	-0.060	-0.068	-0.075	-0.083
Weld penetration (µm)	0.001	0.002	0.003	0.004	0.007	0.008	0.009	0.010
Laser angle (Degrees)	-0.004	-0.007	-0.011	-0.015	-0.029	-0.033	-0.037	-0.040
Stress (GPa)	-	-	-	-	0.1144	0.1143	0.1142	0.1140

According to Box and Draper (1987) if the interactions between the factors are strong, as they are in this model, computing the steepest path may give erroneous results. The current view (Myers et al., 2009) is that computing a steepest path will differ only marginally from the true path where there are large interactions, and can lead to an extra round of experimenting to compensate for the errors in estimating the path.

7.3.2 Novel Application of Monte Carlo Simulation

The steepest path calculation is a well-established technique within the response surface methodology. As it requires a number of experiments to be performed it is a resource intensive technique, both in terms of investment of experimentation materials and time. Additionally, this can be exacerbated if a poor choice is made for the step size. The step

size is chosen according to expert opinion (Montgomery 2012), which can still leave room for doubt as to whether an appropriate step was chosen. To overcome this issue a more rigorous technique is proposed for selecting the step size using a Monte Carlo simulation.

A software application was coded in Java to run a Monte Carlo simulation to identify an appropriate step size. Inspection of the software code suggests that with minor adjustments additionally the Monte Carlo simulation could also be used to locate the optimal region of the response surface. It became obvious that if the Monte Carlo simulation can locate an optimal step size and then in turn it can be used to sample the response surface, could the Monte Carlo simulation be used to sample the response surface without the use of a step size? In light of this the following was implemented:

(a) Use a Monte Carlo simulation to find a step size and in turn sample regions of the response surface.

(b) Use a Monte Carlo simulation to find the optimal region without using a step size.

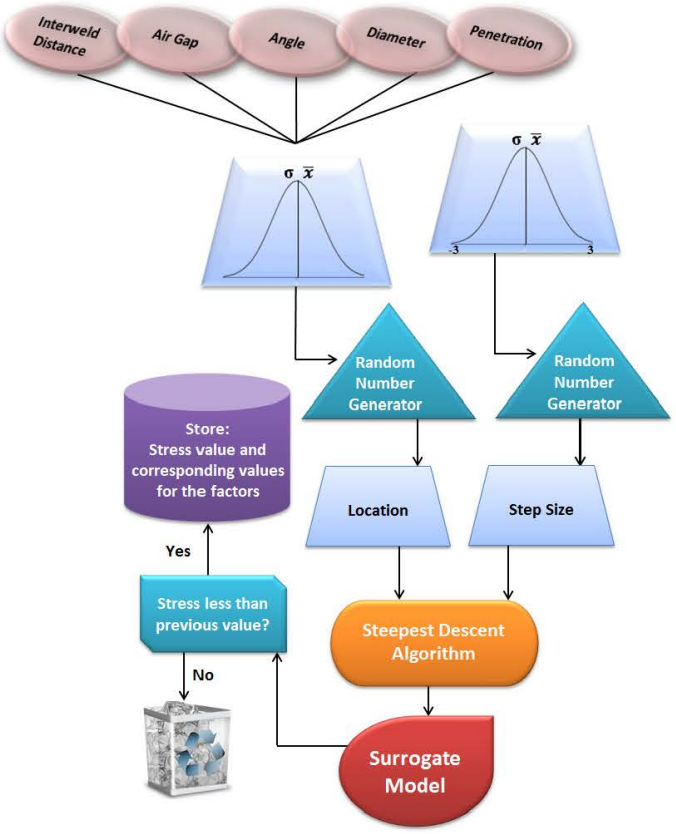

Figure 7.7. Monte Carlo simulation generating location and step size.

To find the optimal response using a Monte Carlo simulation for the process under study, the Java application used pseudo random numbers that were generated from a normal distribution using the Marsaglia polar method (Thomas et al., 2007).

The Monte Carlo simulation for method (a), randomly generated step sizes are used to search for a minimal response at locations randomly generated on the response surface and within the design parameters, see figure 7.7. The diagram shows that random values are generated from a normal distribution. For the step size a random number was generated between three and minus three micrometres. The value of three was chosen to ensure it was in excess of the initial step values which did give a decrease in the response.

Instead of starting from the centre of the experiment, a randomly generated location was used. For each factor a normal distribution was generated with a mean and standard deviation peculiar to that factor, see table 7.1. This was then used to generate a random location. This ensured that only the process space was sampled. For each step size, 20 steps were generated for each location.

The stress value that was generated was compared to the previously stored value. If the new stress value (response) was less than the previously stored value(s), this candidate optimal response was also stored. The results of this experiment are summarised in table 7.5, indicating the optimal values for the factors, the stress achieved and the step size found.

Table 7.5. Optimal values found using the Monte Carlo simulation for method (a).

		Number of step size samples	Locations sampled on the response surface			
		1000000	500000			
	Air Gap (µm)	Interweld Distance (mm)	Diameter (mm)	Penetration (µm)	Angle (Degrees)	
Stress (GPa) 0.0619	0.0111	4.9993	0.5051	49.7310	34.6151	Engineering units
Step size -0.297	-0.9999	0.9997	0.8016	0.9731	0.9230	Coded units

The number of step sizes that were sampled was 1000000. The response surface was then randomly sampled in 500000 locations. The time taken during the simulation to find an overall optimal value was 34 minutes. The total time to run the simulation was 50 hours and nine minutes and it yielded 8053 candidate optimal responses.

Figure 7.8 shows the range of the steps sizes and the candidate optimal responses, of which there was 8053. It appears that most of the candidate optimal responses were within a range of plus or minus 0.2 micrometre. There were no candidate optimal responses found with a step of plus or minus three micrometres. There were no candidate optimal responses less than 0.0619 GPa.

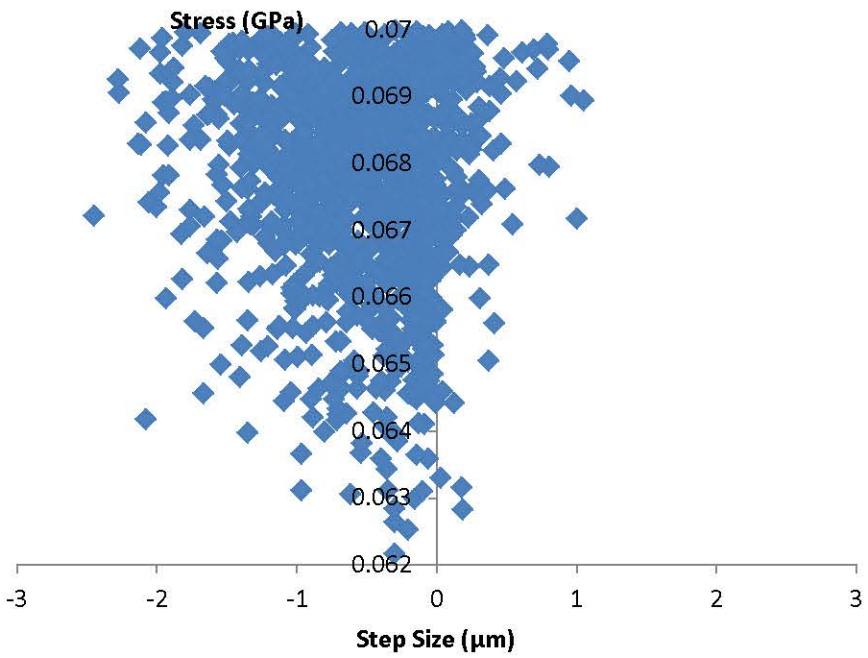

Figure 7.8. First Monte Carlo simulation method for the step size and the candidate optimal responses.

Figure 7.9 shows a frequency distribution of the candidate optimal responses. The graph indicates that the simulation sampled stress values at the higher end at a greater frequency than those stress values at the lower end.

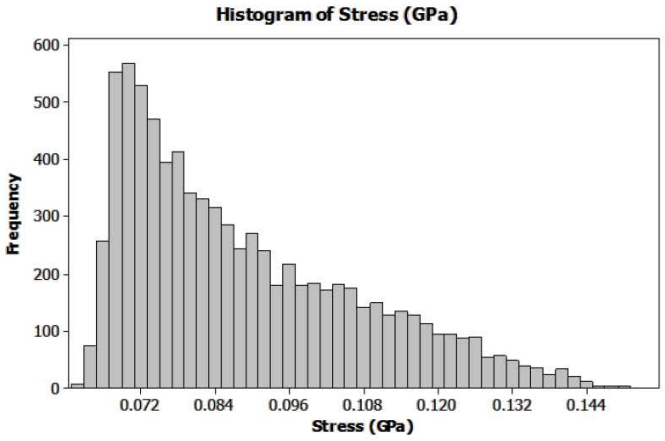

Figure 7.9. Frequency histogram of the candidate (minima) optimal responses for the Monte Carlo simulation for the step sizes.

The second Monte Carlo simulation (b), randomly searched the response surface for an optimal stress value, see figure 7.10.

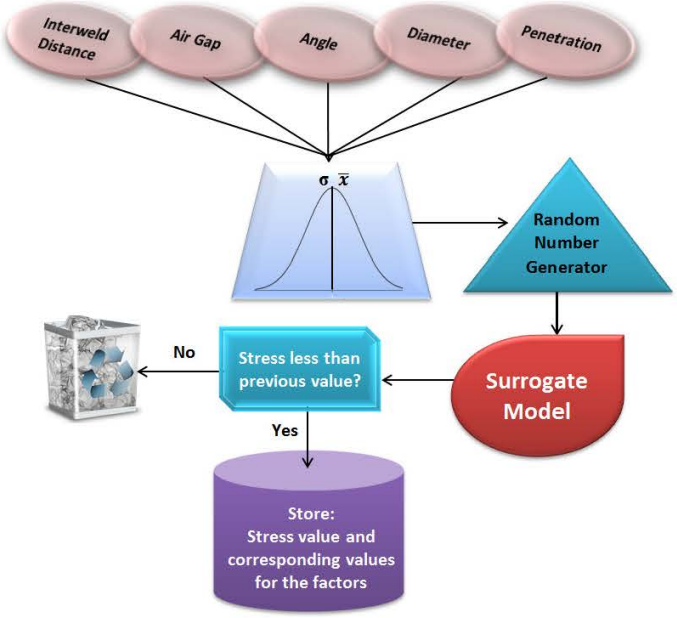

Figure 7.10. The second Monte Carlo simulation (b).

Random values from a normal distribution that fell within the design limits of the process were generated for the factors. The stress value that was generated was only stored if it was less than the previously generated stress value, table 7.6, summarises the findings. The total time to run the simulation was 89 hours and 34 minutes. A total of

100000000 locations were sampled, and iteration 17218093 identified the optimal location out of a total of 14 candidate optimal responses.

Table 7.6. Monte Carlo simulation used to sample the response surface.

Stress (GPa)	Air Gap (µm)	Interweld Distance (mm)	Diameter (mm)	Penetration (µm)	Angle (Degrees)	
0.0616	0.1717	4.9905	0.5943	49.5231	34.2912	Engineering units
	-0.9828	0.9952	0.9432	0.9523	0.8582	Coded units

The second Monte Carlo simulation (b), located a minimised response; hence there was no advantage in finding a step size first. The second simulation appears to have found the minimum which corresponds to a stress value of 0.0616 GPa. Nevertheless, this is still not as good as the values used for the factors when they are at their centre points. The prime reason for this being that this is the limit of the first order model, and further progress can only be obtained by the use of a second order model. The second order model was not developed as it was not part of the current OPISA methodology, and falls under future work.

7.4 Process Capability

The risk analysis of the data variation shows that the stress in the fibre follows a lognormal distribution, see figure 7.3. Capability indices are not applicable, as they require a normal distribution.

With normally distributed data the process capability indices C_{pk} and P_{pk} are of choice (Wu, et al., 2009). The performance of the process in relation to the process parameters and the process specifications are indicated by these indices which are dimensionless. From figure 7.3, the data is indicated to be non-normally distributed and appears to be of a lognormal distribution. This is confirmed from the calculations shown on the probability plots in figure 7.11. For the Anderson-Darling goodness of fit test the high p-value (p-value = 0.505 > 0.05) confirms the lognormal model. The lognormal

distribution is a good model for the stress data, as there is not enough evidence in the data to reject the null hypothesis.

In such situations of non-normality the options that are available include data transformation or the use of distribution free indices (Kotz and Johnson, 2002). The main issues of data transformation are that they are computing intensive (Tang and Than, 1999). Additionally, there are problems associated with translating the computed results with reference to the original scales (Kotz and Johnson, 2002; Ding, 2004).

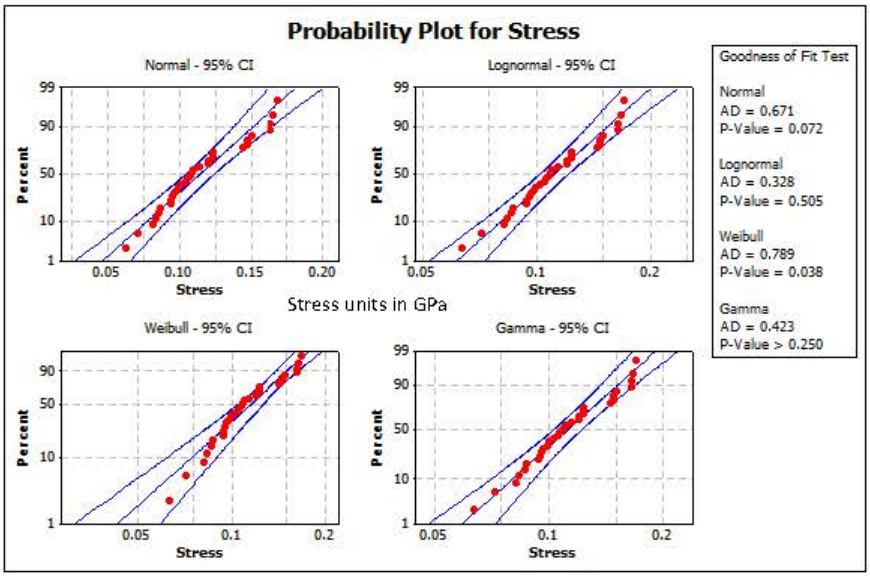

Figure 7.11. Probability graphs for stress using a normal, Weibull, lognormal and gamma distribution.

The construction of C_p and C_{pk} using a lognormal distribution has been investigated by Lovelace and Swain (2009), which will be considered here. The process spread for normally distributed data is between +3 and -3 standard deviations. This corresponds to the 0.135^{th} and the 99.865^{th} percentile of the data distribution.

With C_{pk} it takes the distance from the average of the data to the nearest specification and divides by three standard deviations. A more general calculation (Pal 2005) of C_{pk}, is derived in equation 7.3:

$$C_p = \frac{allowable\ spread}{process\ spread} = \frac{USL - LSL}{x_{0.99865} - x_{0.00135}} \qquad \textbf{7.3}$$

Where USL is the upper specification limit and LSL is the lower specification limit. The acceptable spread with respect to the upper and lower specifications is given by C_{pl} and C_{pu}.

$$C_{pl} = \frac{x_{0.5} - LSL}{x_{0.5} - x_{0.00135}} \qquad \textbf{7.4}$$

$$C_{pu} = \frac{USL - x_{0.5}}{x_{0.99865} - x_{0.5}} \qquad \textbf{7.5}$$

Where $x_{0.5}$ is the median, then:

$$C_{pk} = min\{C_{pu}, C_{pl}\} \qquad \textbf{7.6}$$

Then C_{pk} is equal to the minimum of C_{pl} and C_{pu}, equation 7.6. The percentage of parts beyond the upper or lower specification is indicated by C_{pk}, whichever percentage is lower.

For the stress in the fibre optic data, the stochastic calculation for C_{pk} is as follows and:

$$C_{pk} = min\left\{\frac{0.11604 - 0.0616}{0.11604 - 0.09041}, \frac{0.1128 - 0.11604}{0.14655 - 0.11604}\right\} \qquad 7.7$$

The results for equation 7.7 are shown in table 7.7, and are compared with the values which were deterministically obtained using Minitab.

Table 7.7. Comparison of the percentile values, C_{pl} and C_{pu} derived deterministically and stochastically.

	LSL	0.0616	
	USL	0.1128	
		Deterministic	Stochastic
Percentile	99.865%	0.2356	0.14655
	50.000%	0.1111	0.11604
	0.135%	0.0524	0.09041
	C_{pl}	0.843	2.124
	C_{pu}	0.014	-0.106

The reported values, figure 7.12, for the 0.135th, 50th and the 99.865th percentile were obtained deterministically. These values do not take into account the variation that is found in the process.

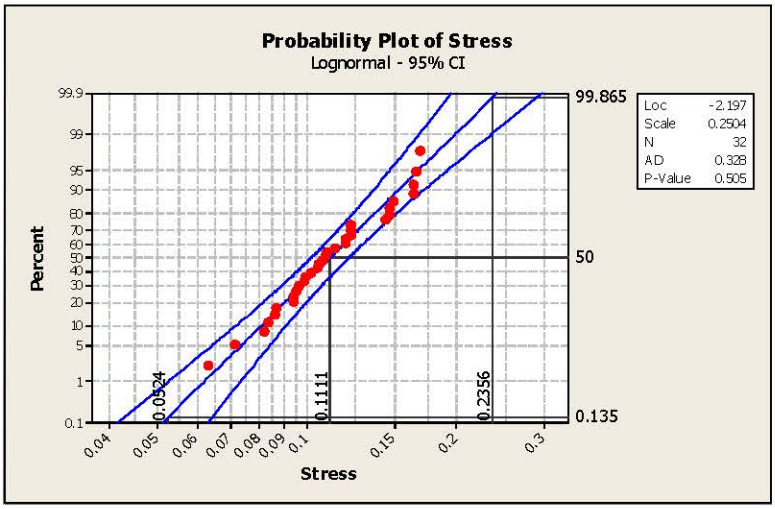

Figure 7.12. probability plot showing the percentiles. The stress units are GPa.

Deterministically, a value of 485603.51 parts per million fall outside of the specification limit, see figure 7.13. Using a Monte Carlo simulation the values for the 0.135th, 50th and the 99.865th percentile are shown in figure 7.3 (a) and (b). For comparison table 7.7, shows the values using the Monte Carlo simulation and those obtained deterministically.

The Monte Carlo simulation shows that the process is within the specification limits 36.1% of the time. Whereas deterministically over 51% of the parts are within the specification limit. This is a big disparity between these two values. Of the two values the Monte Carlo simulation will be closer to the true process estimation, as it takes into consideration the variation that is inherent in the process, that due to the five factors.

The reported values of an inadequate process have been given as $C_{pk} < 1.00$. Quite clearly the process is out of control, whichever C_{pk} is taken in to consideration.

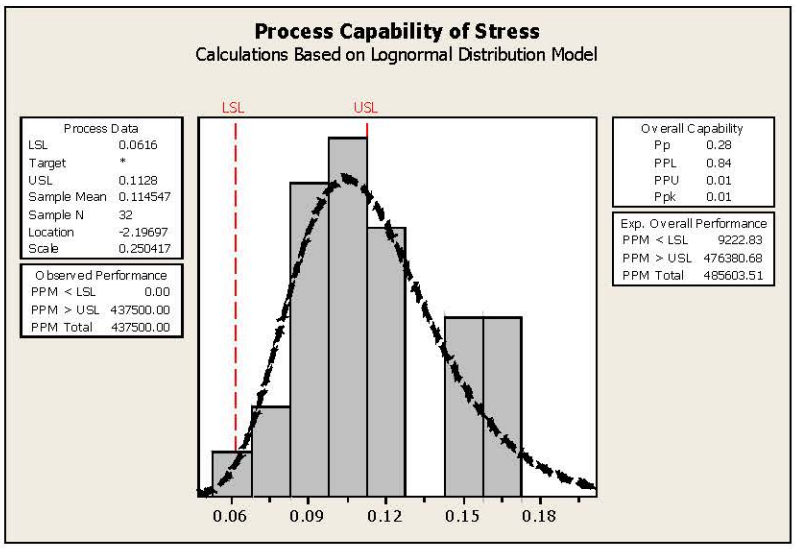

Figure 7.13. Deterministic process capability for lognormal data. The stress units are GPa.

7.5 Conclusion

This chapter has fulfilled the remaining objectives of this project to:

- Perform a risk analysis of the process.
- To improve the process so that it minimise the stress in the optical fibre.
- Discover the capability of the process.

Ordinarily the first order polynomial surrogate model, equation 7.8, can be used to approximate a true response surface that this model will plot in five dimensional space. This will be over a small region of the independent variable space in a location where there is little curvature in the function.

$$y = \beta_0 + \beta_1 x_1 + \beta_2 x_2 + \beta_3 x_3 + \beta_4 x_4 + \beta_5 x_5 \qquad \textbf{7.8}$$

The first order model was found to be poor in approximating the true response surface. Ordinarily it is assumed there will be linearity in the factor effects. Such linearity is not necessary, and the system will work well with an approximation of linearity. By the addition of the interaction terms which in this system are strong, a surrogate first order model with interactions was used to construct a response surface. With the interaction terms added to the main effects first order model, results in equation 7.9:

$$y = \beta_0 + \sum_{j=1}^{k} \beta_j x_j + \sum_{i<j=2}^{k} \sum \beta_{ij} x_i x_j + \varepsilon \qquad \textbf{7.9}$$

The model in equation 7.9, will allow the response function some capability of representing some curvature. The interaction term $\beta_{ij} x_i x_j$, which causes twisting in the plane and is responsible for the curvature.

In those situations where the response model such as equation 7.9, does not adequately represent the curvature, a second order model is needed, equation 7.10:

$$y = \beta_0 + \sum_{j=1}^{k} \beta_j x_j + \sum_{i<j=2}^{k} \sum \beta_{ij} x_i x_j + \sum_{j=1}^{k} \beta_{jj} x_j^2 + \varepsilon \qquad \textbf{7.10}$$

The addition of centre points in a 2^k factorial experiment provides protection against curvature of second order effects. It should be noted that if there are strong interaction terms even with the addition of centre points there will be some twisting of the plane (Box and Draper, 2007).

Process optimisation or improvement involves running a series of experiments starting at the centre of the current region of the process using a response surface. The experimentation follows a path perpendicular to the lines of contour. This is the steepest and quickest path to minimising the response. It locates the minima that occurs on the path. Sequences of experiments are used to follow this path. For this project this would have involved setting up a sequence FEA models, and in lieu of this the model in equation 7.1 was used. Using such a model is not a recommendation, as it would be best

to use the FEA models as the path of steepest descent is traversed. Only for the reason that this project demonstrates the OIPISA methodology was the model of equation 7.2 used.

Using the steepest descent showed a weakness if the appropriate step size is not used. The text books suggest expert opinion in selecting the step size, which is still open to error. To overcome this issue a novel application of Monte Carlo simulations was used in the steepest descent technique to estimate the step size. As a further expansion of using Monte Carlo simulations two techniques were used to implement it with the steepest descent optimisation algorithm. One technique involved estimating stochastically the step size and the location to sample on the response surface. The second technique involved stochastically sampling the response surface.

Using the Monte Carlo simulation to estimate the step size was successful in that it indicated the range of step sizes that could be suitable. From figure 7.8 the range of plus or minus 0.2 micrometre yielded potential step sizes. More specifically a step size was found that gave a minimal stress value. The simulation took 50 hours and nine minutes, which is considerably a very short period of time in comparison to having run a series of FEA simulations along the path of steepest descent. Once again using the Monte Carlo simulations to only locate the optimal region of the response surface appears to be a more resource efficient technique compared to running a series of experiments along the path of steepest descent. There are however more efficient algorithms than Monte Carlo simulations, such as the ant colony (Gupta et al., 2012) that can be used to survey the response surface.

The first order model appeared to be insufficient in locating the optimal process parameters. This indicates the process was already operating at factor settings that were near a minimum response value. A second order model was required by conducting another design of experiment using a central composite design or even a Box-Benkham design. The second order model was not developed as the purpose of this chapter was merely to show how such a methodology of well-established techniques could be used.

Using a Monte Carlo simulation technique the influence of the manufacturing tolerances of the process parameters were assessed as part of the risk analysis. The resulting distribution from the simulation was lognormal and C_p and C_{pk} were constructed using this distribution. The analysis revealed this process to be incapable at a six sigma level.

Chapter 8

Conclusions

The work that has been presented here was part of an industrial case award and has fulfilled the aim that the industrial partner of this project had commissioned. This was to develop techniques that would allow the Oclaro design and development team based in Paignton UK, to locate weld spot positions on the fibre capsule that would result in the least residual stress generated once the laser weld spot had cooled. To achieve this aim nine objectives were realised, and were fulfilled, as discussed in this work. The fulfilment of the first eight objectives collectively resulted in the development of the OPISA methodology. The ninth object was the dissemination of this work to the industrial partner. This has occurred in the form of two reports, two publications and this thesis.

8.1 Thermomechanical Investigation

The evolution of temperature, stresses and displacements caused by laser spot welding of 304L stainless steel of the fibre capsule were initially investigated at a preliminary level. The study used the design of the Oclaro butterfly package and fibre capsule, which was initially modelled as a three dimensional transient numerical model.

The heating curves showed that there is a rapid increase in temperature within the first four milliseconds of the laser hitting the work piece. The maximum temperature achieved in this work compares well to the temperatures achieved by other researches. Shanmugam et al (2013) found a maximum temperature of 4707 K, Abdulateef (2009) found a maximum temperatures of 5244 K. Whilst Desi and Bag (2014) had a maximum temperature of 3000 K.

As solidification of the weld pool progresses it sets the generation of residual stresses in the work piece. The solidification of the weld pool causes a 'pinching' effect that tends to draw the material in towards the weld. This follows the direction of the distortions and the effective stresses in the work piece.

The distribution of stresses in the work piece is influenced by the density of the different materials that comprise the fibre capsule. It has been observed that towards the fibre end, materials that are flexible such as the Hytrel tube and the UV coat tend to allow stresses to travel freely along them. Stiffer materials such as the ceramic capillary tend to build up the stress. At the interfaces between materials localised regions of high stresses were observed in the simulation. The interfaces between materials include the ceramic capillary and the optical fibre and the steel ferrule. These interface generated stresses have been observed by others (Hall 2007).

Materials of a higher density allowed greater fibre displacement, as indicated at the interface of the ceramic capillary and the fibre and the steel ferrule. This produced a peak for maximum displacement and stress.

8.2 Developing the Methodology

The aim of the OPISA project was to develop a methodology that can be used to develop a welding regime that minimises the stress development in the optical fibre. This methodology can be applied generically and has been developed as a proof of concept to demonstrate how improvement in the micro laser welding process of optoelectronic packages can be achieved.

A number of well-established engineering techniques were used to develop this methodology. The OPISA methodology involves the development of a predicative and analytical surrogate model. Such a model can be used to optimise process conditions. This methodology can be used to improve the manufacturing process and hence increase the production rate.

The industrial partner was interested in the development of a simplified two dimensional axisymmetric finite element analysis model. This was developed and used

to undertake thermomechanical analysis of the optoelectronics package to predict stress in fibre. Assumption for linear elastic behaviour of all materials is made in this study. It is found that as the solidification of the weld pools progress this leads to a generation of residual stresses in the work piece.

Initially the evolution of temperature, stresses and displacements caused by the micro welding process of the fibre capsule were studied. The objective of this part of the study was to understand heat transfer and stress evolution during the formation of the weld spot. A physics-based modelling approach using the finite element technique was used to undertake thermomechanical analysis of the optoelectronics package to predict stress in the optical fibre.

The development of peak stresses in the work piece is influenced by a number of design variables (key process parameters). Five key process parameters were identified by expert opinion from the Oclaro engineering team:

- The interweld distance between the two micro weld spots, the first weld is always one millimetre from the butterfly end.
- The air gap between the sleeve and ferrule.
- The angle of the laser.
- The diameter of the weld spot.
- Weld spot penetration.

The main part of the project's focus is on the cooling of the weld spots and how the associated thermal contraction of the weld region induces stress in the optical fibre. To study this, design of experiments (DoE) statistical technique was used to investigate the five key process parameters that influence the resultant stress in the optical fibre. The DoE specified 32 design points for five process parameters. For each set of the process points a respective physics-based finite element model was built and the thermomechanical behaviour of the package simulated. The maximum predicted von Mises stress in the fibre is the design output parameter used to judge quality and performance of the manufacturing process. With lower values for stress resulting in lower risk of failure and misalignment of the laser and the optical fibre.

A predictive surrogate model of the post welding stresses in the fibre optic for different combinations of the design variables was developed from the results of the DoE. The surrogate model is an explicit analytical model, which is a first order polynomial model that was used to make predictions for stress in the fibre, as a function of the five design variables.

Using integrated design of experiment and response surface methodology a surrogate model was developed to investigate sensitivity and risk analysis of the fibre package and associated welding process. It was found that the air gap between the sleeve and ferrule, the inter-weld distance and the weld diameter have a significant main effect, in that order, as compared to the other two variables. However, these key factors had significant interactions which need to be taken into consideration.

A risk analysis was performed using a Monte Carlo simulation to determine the fibre stress variation when uncertainty and variation of the design variables have been taken into consideration. The parameters used an estimated mean and standard deviation, assuming that the parameters all came from a normal distribution.

The optimisation study identified how improvement to package specification can be made using a novel variation on the steepest descent method and Monte Carlo simulation. This novel method conserved resources and can be used to identify the parameter settings of the Oclaro welding regime that gave the least stress. The method can be used to identify the region on the response surface where an improvement in the process can be obtained.

A capability analysis followed the risk analysis. The output from the risk analysis was a lognormal distribution, indicating the traditional method of estimating the capability could not be used as it requires a normal distribution. There are two options in estimating the capability. Either the data could be transformed, which is computer intensive. Or the capability can be estimated from the lognormal distribution. The latter method was chosen. The analysis showed that the process is an incapable process.

The design of experiment based surrogate model has been used to create an interactive web based Java applet. The applet is a welding parameter estimation tool (WPET) and shows how the five process parameters interact.
This can be accessed from–

http://staffweb.cms.gre.ac.uk/~ma60/opisa/XacS/sct/

8.3 Future Work

For future investigations, these can include a number of experiments that can be used to verify the simulation by using the parameters that were estimated by the surrogate model. This has been suggested, and may already have been done by the Oclaro engineering team in China. The other experiments that could done would help verify the simulations and include –

- Investigating laser spot weld geometry of the fusion zone, the heat affected zone, penetration depth and width of the weld spot to agree with the simulation results.
- The weight of the fibre capsule before and after welding, to estimate the degree of vaporisation during the welding process. The weighing can be done using a chemical balance.
- Effects of sequencing the formation of the weld spots.
- Enhancing the complexity of the model by utilising non-linear material models.
- Developing a second order polynomial surrogate model.
- Optimisation of the second order polynomial surrogate model.
- Comparing and contrasting the use of other optimisation algorithms such ant colony optimisation with the steepest descent/ascent and the Monte Carlo technique used in this thesis.
- Record spot temperatures of the weld area using thermocouples. The temperature is take form several areas, in order to try and estimate the temperature gradients involved in this process. Temperature values from the top and bottom of the welded metal are noted.
- With the same laser setup as used for the fibre capsule welds, welds are done on a strip of 304L stainless steel with the following measurements being recorded:-
    - The weight of the strip before and after welding.

  - The dimensions of the strip before and after welding, and noting if the strip is warped.
  - The diameters of each of the three weld spots.
  - The distance between the weld spots.
  - Longitudinal sections are taken of the weld spots and micro-photographed, and the penetration depth and width of weld are noted.
  - The volumes of the weld spots are calculated to get an estimate of the laser power input.
  - Ideally about 300 weld spots should be made over a period of about a week. This information can be used to perform a statistical analysis to see how consist the weld spot are between the locations, and where the predominant variation(s) between them occur.
  - This information can also be used to estimate the laser power, and the degree of shrinkage/distortion involved.
- The above, is repeated for different laser energies, pulse durations and laser beam diameters.
- Use of non-destructive techniques to measure the stress in situ:
  - Ultrasonic stress measurement techniques (Kudryavtev et al., 2004) are based on the acoustic-elasticity effect, according to which the velocity of elastic wave propagation in solids is dependent on the mechanical stress.
  - The magnetic Barkhausen noise (MBN) method (Altpeter et al., 2009) is of particular interest because of its potential as a non-destructive industrial tool to measure surface residual stress (SRS) and other microstructural parameters.
- Include cost and environmental constraints into the surrogate model

References

Abdulateef O F (2009). Investigation of Thermal Stress Distribution in Laser Spot Welding Process. Al-Khwarizmi Engineering Journal, Vol. 5, No. 1, PP33-41.

Akhter R, Davis M, Dowden J, Kapadia P, Ley M and Steen W M, 1989. J. Phys. D, 22, 23-28.

Altpeter I, Dobmann G, Kröning G, Rabung M, Szielasko S., 2009. Micro-magnetic evaluation of micro residual stresses of the IInd and IIIrd order. NDT &E International 42: 283-290.

Andrews JG, Atthey DR. 1976 Hydrodynamic limit to penetration of a material by a high-power beam. Journal of Physics D: Applied Physics 9:2181–2194.

ASM, 1983, Metals Handbook-Volume 6, 9th Edition.

Assembly Magazine http://www.assemblymag.com/

Bag S, and De A. 2010. Computational Modelling of Conduction Mode Laser Welding Process, Laser Welding, Xiaodong Na, Stone (Ed.), ISBN: 978-953-307-129-9.

Bailey C, Tilford T, Ridout T, Lu H, EngOpt 2008 - International Conference on Engineering Optimization. Rio de Janeiro, Brazil, 01 - 05 June 2008.

Becker A. A. 2004. An Introductory Guide to Finite Element Analysis, ASME Press, New York.

Box G.E.P. and Draper N.R. 1987. Empirical Model-Building and Response Surfaces. John Wiley & Sons, New York.

Box G.E.P. and Draper N.R. 2007.Response Surfaces, Mixtures, and Ridge Analyses. Wiley-Interscience.

Box, G. E. P.; Hunter, W. G.; and Hunter, J. S. 1978. Statistics for Experimenters. John Wiley, New York, NY.

Bramson M. A. 1968. Infrared Radiation: A Handbook for Applications, Plenum Press, New York.

Bransch H.N., Weckman D.C. and Kerr H.W. 1994, Welding Journal, 73, No. 6, 141-s - 151-s.

Brebbia C. A. and Partridge P. W. 1992. Boundary Elements in Fluid Dynamics, Elsevier Science, New York.

Bunting KA, Cornfield G. 1975. Towards a general theory of cutting: a relationship between power density and speed. Trans ASME J Heat Transf 97:116–122

Camilleri D, Mollicone P, and Gray T, 2007. Computational methods and experimental validation of welding distortion models, Proceedings of the Institution of Mechanical Engineers, Part L: Journal of Materials: Design and Applications, vol. 221, pp. 235-249

Carslaw H, C, Jaeger J, C. 1997. Conduction of heat in solids. Oxford: Oxford Science Publications.

Chande T, Mazumder J. 1981. Heat flow during CW laser materials processing. In: Mukherjee K, Mazumder J, editors. Proceedings of Lasers in Metallurgy, TMS-AIME, p. 165–77.

Chang W. S., and Na S. J., 2002."A study on the prediction of the laser weld shape with varying heat source equations and the thermal distortion of a small structure in micro-joining," Journal of Materials Processing Technology 120, pp. 208-214.

Cheng W. H., Wang S. C., Yang Y. D., Chi S., Sheen M. T., and Kuang J. H., 1997. "Effect of A thickness on laser beam penetration in semiconductor laser packages," IEEE Transactions on Components, Packaging, and Manufacturing Technology B 20(4), pp. 396-402.

Chiang S. and Albright C.E. 1993, Welding Journal, 72, No. 3, 117-s - 121-s.

Cho, W., Na, S., Thomy, C., and Vollertsen, F., 2012. Numerical Simulation of Molten Pool Dynamics in High Power Disk Laser Welding, Journal of Materials Processing Technology, 212(1), pp.262-275.

Cline HE, Anthony TR. 1977. Heat treating and melting material with a scanning laser or electron beam. Journal of Applied Physics 48:3895–3900.

Connon LP. 1991. "Welding handbook, Welding technology", Eight edition, Miami: American Welding Society, pp 67-87, 218-264, ISBN 0-87171-281-4.

Daniel, C. 1976. Applications of Statistics to Industrial Experimentation. New York: Wiley.

Davis J. R. 1998. Metals Handbook (ASM International, Materials Park, OH,).

De A, Maiti S. K., Walsh C. A. and Bhadeshia H. K. D. H. 2003. Prediction of Cooling Rate and Microstructure in Laser Spot Welds. Science & Tec. of Weld. & Join. 8:6

Deaconu, V. 2007. Finite Element Modelling of Residual Stress - A Powerful Tool in the Aid of Structural Integrity Assessment of Welded Structures. 5th Int. Conference Structural Integrity of Welded Structures (ISCS2007), Timisora, Romania, 20-21 Nov.

Desai R. S, and Bag S, 2014. Influence of displacement constraints in thermomechanical analysisof laser micro-spot welding process. Journal of Manufacturing Processes 16, 264–275

Deshayes Y., Becbou L., Deletage J. Y., Verdier F., Danto Y., Laffitte D., and Goudard J. L., 2003. "Three- dimensional FEM simulations of thermalmechanical stresses in 1.55um laser modules," Microelectronics Reliability 43, pp. 1125-1136.

Dowden J, and Kapadia P. 1995. A mathematical investigation of the penetration depth in keyhole welding with continuous CO2 lasers. Journal of Physics D: Applied Physics 28: 2252–2261.

Dowden J, Postacioglu N, Davis M, Kapadia P. 1987. A keyhole model in penetration welding with a laser. Journal of Physics D: Applied Physics 20:36–44.

Duley WW. 1999. Laser welding. Wiley, New York.

Dwivedi A, Glaesemann G.S. 2011. Optical Fiber Strength, Fatigue and Handleability After Aging in a Cable. Corning New York.

Edge, C 2006. Personal communication, Caswell.

Fadhali, M.; Zainal, J.; Munajat, Y.; Ali, J. & Rahman, R. 2007. Reliable pigtailing of photonic devices employing laser microwelding. Journal Engineering and Applied Science, Vol. 2, pp. 1724-1728.

Fassani R. N. S. and Trevisan O. V. 1999. Analytical Modeling of Multipass Welding Process with Distributed Heat Source. 15th Brazilian Congress of Mechanical Engineering. São Paulo. SP. Brazil.

Femsys http://www.femsys.co.uk/

Feng, Zihli, 2005. Processes and mechanism of welding residual stress and distortion Woodhead Publishing Ltd, 1st Ed, Cambridge, England, Chap. 1-3, 5-9.

Finetech GmbH and Co. KG. http://www.finetech.com

Fraser J. Personal communication. Bookham Technology Caswell. 2007.

Frewin, M. R. and Scott, D. A. 1999. Finite Element Model of Pulsed Laser Welding, Welding Journal, Welding Research Supplement, pp. 15s-22s.

Fuerschbach P. W. and Eisler, G. R. 2002. Effect of laser spot weld energy and duration on melting and absorption Weld. J., v7, 4

Fuerschbach P. W. and Norris J. T. 2002 , Beam Characterization for Nd:YAG Spot Welding Lasers, Scottsdale, AZ.

Fuerschbach P. W., 1996. Measurement and prediction of energy transfer efficiency in

laser beam welding, Welding Journal, Vol.75, 24s-34s.

Gatovskii K. M. and Karkhin V. A. 1980. Theory Of Welding Stresses And Deformations. Leningrad Shipbuilding Institute.

GIA. 2010. Optoelectronics – A Global Strategic Business Report. Global Industry Analysts, Inc.

Goldak J, Chakravarti A, and Bibby M, 1984, A New Finite Element Model for Welding Heat Source. Metallurgical Transactions B, 15B: p. 299-305.

Gourd, L. M., 1991, second Ed., Principles of Welding Technology, Edward Arnold.

Gunaraj V, and Murugan N, 1999. Application of response surface methodology for predicting weld bead quality in submerged arc welding of pipes, J. of Mat. Processing Tech., Vol. 88, pp. 266-275.

Gunaraj V, and Murugan N, 2000. Prediction and optimization of weld bead volume for the submerged arc process-part 2, welding journal, AWS, 331-s-338-s.

Gunaraj V, and Murugan N, 2000. Prediction and optimization of weld bead volume for the submerged arc process-part 1, Welding journal, AWS, 286-s- 294-s.

Gunaraj V, and Murugan N, 2002. Prediction of heat-affected zone characteristics in submerged arc welding of structural steel pipes, welding journal, AWS, 94-s-98-s.

Gupta, D.K.; Arora, Y.; Singh, U.K.; Gupta, J.P., 2012. Recursive Ant Colony Optimization for estimation of parameters of a function. Recent Advances in Information Technology (RAIT), 2012 1st International Conference on , vol., no., pp.448,454, 15-17

Hall J. 2006., Bookham Technology Caswell: Personal communication.

Hamoudi W, Ducharme R. 1996. Keyhole welding of C-Mn steel using a 10kW CO_2 laser. Int J Join Mater;8:30–6.

He X. DebRoy T. Fuerschbach P .W. 2003. Probing temperature during laser spot welding from vapor composition. and modeling. J Appl. Phys. 39 525

He X., Norris J .T., Fuerschbach P .W. and DebRoy T .2006. Liquid metal expulsion during laser spot welding of 304 stainless steel. J. Phys. D: Appl. Phys. 94 10

Hill WJ, Hunter WG. 1989. A Review of Response Surface Methodology: A Literature Review. Technometrics, 8, 571-590.

Hilton PA, 1995. Optical and Quantum Electronics, 27, 1127-1147.

İç Y. T, Elaldi F, Pakdil F., and Ipek N. E., 2012. Design of Experiment and Goal

Programming Application for the GMAW Process. AWS April Vol 91 106s

Incropera F. P., DeWitt D. P. 1996. Fundamentals of heat and mass transfer, Fourth edition. Fourth edition, New York: John Wiley & Sons, pp. 52-55.

Ion J. C. 2005. Laser processing of engineering materials –Principles, procedure and industrial applications, Elsevier.

Ion, J. C., 2005, Laser Processing of Engineering Materials, Elsevier Butterworth-Heinemann, Burlington, MA

Ishikawa K. et al., . 2002. An Integrated Micro-Optical System for Laser-to-Fiber Active Alignment, The 15th IEEE International Conf. on Micro-Electro-Mechanical Systems (MEMS 2002), Las Vegas, January 20-24.

Jang S. 1996 Packaging of photonic devices using Laser welding. In: Proc SPIE, p. 138–49.

Jin X., Zeng L. and Cheng Y. (2012). Direct observation of keyhole plasma characteristics in deep penetration laser welding of aluminium alloy 6016. J. Phys. D: Appl. Phys. 45.

Kanouff, M.P. and Greif, R. 1992, "The Unsteady Development of a GTA Weld Pool;' International Journal of Heat and Mass Transfer, Vol. 35, pp. 967-979

Kaplan A. 1994 A model of deep penetration laser welding based on calculation of the keyhole profile. Journal of Physics D: Applied Physics 27:1805–1814.

Kar A., and Langlais M.D. 1995, Optical and Quantum Electronics, 27, 1165-80.

Kazemi, K & Goldak, J.A. 2009. Numerical simulation of laser full penetration welding. Computer Material Science, Vol. 44, pp. 841–849.

Khuri A.I.and Cornell J. A. 1996. Response Surfaces: Designs and Analyses: Second Edition CRC Press.

Klemens PG. 1976. Heat balance and flow conditions for electron beam and laser welding. Journal of Applied Physics 47:2165–2174.

Koleva E, 2001. Statistical modelling and computer programs for optimisation of the electron beam welding of stainless steel, J. Vacuum, Vol. 62, , pp. 151- 157.

Koric, S. and Thomas, B. G. 2008. "Thermo-mechanical models of steel solidification based on two elastic visco-plastic constitutive laws ". Journal of Materials Processing Technology 197(1-3). pp. 408-418

Kotz, S. and Johnson, N. L. 2002. Process Capability Indices – A review, 1992 – 2000/ Discussion/Response. Journal of Quality Technology. 34 (1) pp. 2 – 53.

Krishnamoorthy A.V. 2003. "Optical interconnects to the board/chip," in Institute of Physics Handbook on Laser.

Kuang J H., Hung T P., Chiou S H., Hsu C M., 2012. Enhancement of coupling efficiency of butterfly package laser modules based on Post-Weld-Shift compensation. Applied Mechanics and Materials Vol. 145 pp 109-113.

Kuang J. H., Sheen M. T., Wang S. C., Chen C. H., and Cheng W. H., 1999. "Crack formation mechanism in laser welded Au-coated invar materials for semiconductor laser packaging," IEEE Transactions on Advanced Packaging 22(1), pp. 94-100.

Kuang J. H., Sheen M. T., Wang S. C., Chen C. H., and Cheng W. H., 2001. Post-weld-shift in dual-in-line laser package. IEEE Transactions on Advanced Packaging 24(1), pp. 81-85.

Kuang J. H., Sheen M. T., Wang S. C., Wang G. L., and Cheng W. H., 2001. "Post weld shift in dual in line laser package," IEEE Trans. Adv. Packag., vol. 24, pp. 81–85.

Kudryavtev Y, Kleiman J, Gushcha O, Smilenko V, Brodovy V., 2004, Ultrasonic technique and device for residual stress measurement. X Int. Congress and Exposition on Experimental and Applied Mechanics; pp. 1-7.

Labudovic M., and Burka M., 2003. "Finite Element Analysis of Post-Weld Shift During Fiber Pigtail of 980nm Pump Lasers," IEEE Transactions on Advanced Packaging 26, pp. 41-46.

Lancaster J. F. 1986. The Physics of Welding, 2nd Edition, Pergamon, Oxford.

Lankalapalliy KN, Tuy JF and Gartnerz M. 1996. A model for estimating penetration depth of laser welding processes.J. Phys. D: Appl. Phys. 29 1831–1841.

Lightfoot N. M. H. 1930. The Solidification of Molten Steel Proc. London Math. Soc. s2-31(1): 97-116.

Lin Y. and Shi F. G., 2007. "Minimization of welding-induced-alignment distortion in butterfly laser module packages: A study of laser pulse shape," Opt. Eng., vol. 46, no. 4, p. 044302-1-5.

Lin Y., Eichele C., and Shi F. G., 2005. "Effect of welding sequence on welding-induced-alignment-distortion in packaging of butterfly laser diode modules: Simulation and experiment," J. Lightw. Technol., vol. 23, no. 2, pp. 615–623.

Lin YG., Guo J., Shapiro A. A., and Shi F. G., 2007. "WIAD Minimization in Butterfly Laser Module Packages: Clip Design" IEEE Transactions On Advanced Packaging, Vol. 30, no. 3

Lindgren L E., 2001. Finite Element Modelling and Simulation of Welding. Part 1: Increased Complexity, Journal of Thermal Stresses, 24: 141-192.

Liu J.G. et al., . 2000. Epoxy adhesives for Optical Element Attachment in Planar Passive Optical Components, Proc. 50th IEEE-Electronic Components and Technology Conference.

Lovelace, C. R. and Swain, J. J. 2009. Process capability analysis methodology for zero bound, non-normal process data. Quality Engineering, 21, 190-202.

Luminomics Inc www.luminomics.com/

M. R Frewin, and D. A. Scott, 1999. Finite element method of pulsed laser welding. Welding Research Supplement, January, pp. 15-22 (1999).

Malik A, Hughes M, Bailey C. 2007. Optoelectronic Packaging Interfaces for Submicron Alignment (OPISA) and the Dynamic of laser Spot Weld Formation. 1st European Semantic Technology Conference, Germany.

Malik Asif, Hughes Michael, Bailey Chris. 2007. Optoelectronic Packaging Interfaces for Submicron Alignment (OPISA) and the Dynamic of laser Spot Weld Formation. 1st European Semantic Technology Conference, Germany, May.

Manonmani K, Murugan N, and Buvanasekaran G, 2005. Effect of process parameters on the weld bead geometry of laser beam welded stainless steel sheets, Inter. J. for the Joining of Materials, Vol. 17, n. 4, pp.103-109.

Mazumder J, Steen WM. 1980. Heat transfer model for CW laser materials processing. J Appl Phys 51:941–947

Minitab 16, http://www.minitab.com

Mobarhan S. Jang K., S., and Heyler R., 2000. "Laser diode packaging technology: 980 nm EDFA pump lasers for telecommunication applications," Tech. Rep., Newport Application Note, 6, pp. 1–7.

Montgomery D C, Peck E A, Vining G G. 2006. Introduction to Linear Regression Analysis, 4th edition John Willey and Sons, New York.

Montgomery, D. C. 2012 . Design and Analysis of Experiments, 8th Edition. John Wiley, New York, NY.

Moraitis, G. A., and Labeas, G. N., 2008, "Residual stress and distortion calculation of laser beam welding for aluminum lap joints," Journal of Material Processing Technology, 198, pp. 260-269.

Mueller P. and Valk B., 2000. "Automated fiber attachment for 980 nm pump

modules," in Proc. 50th IEEE 2000 Electron. Comp. Technol. Conf., Las Vegas, NV, pp. 5–9.

Myers RH, Montgomery DC, Vining GG, Borror CM, Kowalski SM. 2004. "Response Surface Methodology: A Retrospective and Literature Survey." Journal of Quality Technology, 36, 53-78.

Myers R.H., Montgomery D.C., and Anderson-Cook C.M. 2009. Response Surface Methodology: Process and Product Optimization Using Designed Experiments. Wiley.

Nawi I N, Ali J, Fadhali M, Yupapin P P. 2012. Nd:YAG Laser Welding for Photonics Devices Packaging. In Welding Processes Ed. R Kovacevic. ISBN 978-953-51-0854-2.

Newport http://www.newport.com

Norman AF, Ducharme R, Mackwood A, Kapadia P, Prangnel PB. 1998. Application of thermal modelling to laser beam welding of aluminium alloys. Sci Technol Weld Join 1998;3:260–6.

OITDA. 2012. Future Vision of the Optoelectronics Industry. Optoelectronic Industry and Technology Development Association Publishing.

Pang, M.; Yu.G.; Wang, H.H. & Zheng, C.Y. (2008). Microstructure study of laser welding cast nickel-based superalloy K418. Journal of Material Processing Technology, Vol. 207, pp. 271–275

Pang, M.; Yu.G.; Wang, H.H. & Zheng, C.Y. 2008. Microstructure study of laser welding cast nickel-based superalloy K418. Journal of Material Processing Technology, Vol. 207, pp. 271–275.

Park M. W., Kim J. R., Park S., Lee J. S., Kim H. I., Choo A. G., and Kim T. I., 2000. "Lens-lens Semiconductor Optical Amplifier (SOA) mod- ules using laser welding techniques," in Proc. 50th IEEE 2000 Electron. Comp. Technol. Conf., Las Vegas, NV, pp. 733–735.

Patankar S. V. 1982. Numerical Heat Transfer and Fluid Flow, Hemisphere Publishing Corp., New York,

PHYSICA, User Guide and Documentation, Multi-Physics Software (MPS) Ltd, London, UK, http://www.multiphysics.com.

Radaj D. 1992. Heat Effects of Welding. Springer-Verlag.

Raveendra J, and Parmar R. S, 1987.Mathematical models to predict weld bead geometry for flux cored arc welding, J. of Metal construction, Vol. 19, n. 2, pp. 31R-35R

Resch M and Kaplan A.F.H. 1998. Lasers in Engineering, 7, 229-240.

Russo, A. J., Akau, R.L. and Jellison, J. L. 1990. "Thermocapillary Flow in Pulsed Laser Beam Weld Pools;' Welding Research Supplement, pp. 23s-29s.

Sabbaghzadeh J, Azizi M, Torkamany MJ. 2008. Numerical and experimental investigation of seam welding with a pulsed laser. J Opt Laser Technol; 40:289–96.

Schubert E., M. Klassen, I. Zerner and G. Sepold, 1998, Laser Magazin, 4, 17-20.

Semak VV, Damkroger B, Kempka S. 1999. Temporal evolution of the temperature field in the beam interaction zone during laser material processing. J Phys D; 32:1819–25.

Semak VV, Hopkins JA, McCay MH and McCay TD.: Melt pool dynamics during laser welding. J. Phys. D: Appl. Phys. 28 (1995) 2443-2450.

Shanmugam N S, Buvanashekaran G, Sankaranarayanasamy K. (2013). Some Studies on Temperature Distribution Modeling of Laser Butt Welding of AISI 304 Stainless Steel Sheets. World Academy of Science, Engineering and Technology
Vol:7

Shaw M., Galeotti R., and Coppo G., 2001 "Method of fixing an optical fiber in a laser package," in Proc. 51st IEEE 2001 Electron. Comp. Technol. Conf., Lake Buena Vista, FL, pp. 21–26.

Shyy W., Ouyang H., Blosch E., Thakur S. S. and Liu J. 1997.Computational Techniques for Complex Transport Phenomena, Cambridge University Press,
London.

Sleeper A. 2006. Six Sigma Distribution Modeling, McGraw-Hill.

Soul F, Hamdy N. 2012. Numerical Simulation of Residual Stress and Strain Behavior After Temperature Modification. In Welding Processes Ed. R Kovacevic. ISBN 978-953-51-0854-2.

Stearns R.C. and Trask S. 2004. Packaging challenges: Case studies in packaging engineering. Photonics IEEE Photonics Society.

Steen W.M, Dowden J, M. Davis and P. Kapadia, 1988, J. Phys. D, 21, 1255-1260.

Stephens, M. A. 1974. EDF Statistics for Goodness of Fit and Some Comparisons
Journal of the American Statistical Association, 69, pp. 730-737.

Stoyanov, S., Bailey, C., Lu, H. and Cross, M. 2002. "Integrated Computational Mechanics and Optimization for Design of Electronic Components", Optimization in Industry, pp. 57-70.

Swift-Hook DT, Gick AEF. 1973. Penetration welding with lasers. Weld Res Suppl;492s–8s.

Tang Y.K., Stoyanov S., Bailey C., Chan Y.C. 2008. EngOpt - International Conference on Engineering Optimization. Rio de Janeiro, Brazil, 01 - 05 June 2008

Tang, L. C. and Than, S. E. 1999 . Computing Process Capability Indices for Non-Normal Data: A review and Comparative Study. Quality and Reliability Engineering International. 15 (5) pp. 339 – 353.

Thomas D, Wayne Luk, Philip H.W. Leong, and John D. Villasenor. 2007. Gaussian random number generators. ACM Comput. Surv. 39, 4, Article 11 (November 2007).

Tsirkas, S.A., Papanikos, P., Kermanidis, Th. 2003. Numerical simulation of the laser welding process in butt-joint specimens. Mater. Process. Technol. 134, 59–69.

Unitek Miyachi www.miyachiunitek.com/

Vernooy D.W. et al., . 2004. Alignment-Insensitive Coupling for PLC-Based Surface Mount Photonics," IEEE Photonics Technology Letters, 16(1) 269-71.

Versteeg H. K. and Malalasekera W. 1996.An Introduction to Computational Fluid Dynamics: The Finite Volume Method, Addison-Wesley, New York.

Wang, R., Lei, Y., and Shi, Y., 2011. Numerical Simulation of Transient Temperature Field during Laser Keyhole Welding of 304 Stainless Steel Sheet, Optics & Laser Technology, 43, pp.870-873.

Withers P. J. & Bhadeshia H. K. 2000. Residual Stress, Measurement Techniques, Mat. Sci. Tech.

Wu, C. W., Pearn, W. L. and Kotz, S. 2009. An Overview of Theory and Practice on Process Capability Indices for Quality Assurance. International Journal of Production Economics. 117 (2) pp. 338 – 359.

Yang L. J, Bibby M. J, and Chandel R. S, 1993. Linear regression equations for modelling the submerged-arc welding process, J. of Materials Processing Technology, Vol. 39, pp. 33-42.

Ye, X., and Chen, X., 2002, "Three-dimensional Modeling of Heat Transfer and Fluid Flow in Laser Full-penetration Welding," J. Phys. D: Appl. Phys., 35(10), pp. 1049-1056.

Yeung K. S., and Thornton P. H., 1999. "Transient thennal analysis of spot welding electrodes," Welding Research Supplement, January, pp. 1-6.

Zhang W, Roy GG, Elmer JW and DebRoy T. 2003. Modelling of heat transfer and

fluid flow during gas tungsten arc spot welding of low carbon steel. Journal of Applied Physics volume 93, number 5 1.

Zhou, J. & Tsai, H.L. (2008). Modelling transport phenomena in hybrid laser-MIG keyhole welding. International Journal of Heat and Mass Transfer, Vol. 51, pp. 4353-4366.